



## 저작자표시-비영리-변경금지 2.0 대한민국

이용자는 아래의 조건을 따르는 경우에 한하여 자유롭게

- 이 저작물을 복제, 배포, 전송, 전시, 공연 및 방송할 수 있습니다.

다음과 같은 조건을 따라야 합니다:



저작자표시. 귀하는 원저작자를 표시하여야 합니다.



비영리. 귀하는 이 저작물을 영리 목적으로 이용할 수 없습니다.



변경금지. 귀하는 이 저작물을 개작, 변형 또는 가공할 수 없습니다.

- 귀하는, 이 저작물의 재이용이나 배포의 경우, 이 저작물에 적용된 이용허락조건을 명확하게 나타내어야 합니다.
- 저작권자로부터 별도의 허가를 받으면 이러한 조건들은 적용되지 않습니다.

저작권법에 따른 이용자의 권리는 위의 내용에 의하여 영향을 받지 않습니다.

이것은 [이용허락규약\(Legal Code\)](#)을 이해하기 쉽게 요약한 것입니다.

[Disclaimer](#)

공학박사학위논문

루우버 흰을 가지는 콤팩트 열교환기에  
대한 열다공성 모델 연구

A Study on thermal porosity model for compact  
heat exchanger with louvered fin

2016년 2월

서울대학교 대학원

기계항공공학부

김 택 근

# 루우버 회를 갖는 콤팩트 열교환기의 열 다공성 모델 연구

Study on thermal porosity model for compact heat  
exchanger with louvered fin

지도교수 이 준 식

이 논문을 공학박사 학위논문으로 제출함

2015 년 10 월






서울대학교 대학원

기계항공공학부

김 태 근

김태근의 공학박사 학위논문을 인준함

2015 년 12 월

위 원 장 : 최 만 수   
부위원장 : 이 준 식   
위 원 : 김 민 수   
위 원 : 강 희 찬   
위 원 : 김 영 원 

## **Abstract**

# **A study on thermal porosity model for compact heat exchanger with louvered fin**

**Taek Keun Kim**

**School of Mechanical and Aerospace Engineering**

**Seoul National University**

Due to the peculiar geometry of louvered fin and its complicated nearby heat and flow distribution, the 3D numerical analysis of a compact heat exchanger containing a louvered fin had been a difficult analysis task. In this study, an empirical equation for friction coefficient of a louvered fin was proposed by assuming it to be a porous medium, in order to enable the 3D numerical analysis of a compact heat exchanger containing it. In the empirical equation for friction coefficient, the intrinsic permeability and Ergun constant of the louvered fin were derived as a function of parameters for the louvered fin. In order to determine the intrinsic permeability and Ergun constant of the louvered fin, a database of friction coefficient at Reynolds number from 0.001 to 30,000 was established for 14 different types of louvered fin models that are magnified by a factor of three. For Reynolds number from 100 to 1000, the friction coefficient data was obtained from previous works, and for Reynolds number less than 100 or greater than 1000, the friction coefficient data was obtained from a 3D numerical analysis of two-pitch louvered fin. The aim of obtaining the friction coefficient value for louvered fin at Reynolds number less than 100 or greater than 1000 is to determine the intrinsic permeability for the Darcy



term, which governs viscous force at very low Reynolds number, and to determine the Ergun constant for the non-Darcy term (or Forchheimer term) that governs the inertial force at high Reynolds number. To determine the intrinsic permeability and Ergun constant from the database established through experiment and numerical analyses, nonlinear and linear regression analyses were performed consecutively, and a new friction coefficient of louvered fin suitable for the properties of a porous medium was proposed. By comparing the newly proposed friction coefficient to the coefficients of the modified Darcy equation, which governs the momentum within a porous medium, the intrinsic permeability and Ergun constant of the louvered fin are obtained. For verification, the friction coefficients obtained from the database of 14 louvered fin models using the empirical equation were compared, showing the error within 10% on average. Furthermore, when the intrinsic permeability value is obtained for 14 different types of model and different Reynolds number, while the permeability of the louvered fin is constant for Reynolds number less than 1, it is not constant for Reynolds number greater than 1. This accurately corresponds to the theory of porous medium. In the theory of porous media, the pressure drop in the fluid passing the porous medium is linearly proportional to the Darcy speed when Reynolds number is less than 1, with the proportionality constant being the permeability, that is constant. However, if the Reynolds number is greater than 1, the pressure drop within the porous medium varies nonlinearly with Darcy speed, with the permeability thereof being no longer constant. Therefore, it is observed that assuming louvered fin to be a porous medium is very appropriate. For 3D performance prediction of a compact heat exchanger, the permeability and Ergun constant proposed in this study, and Colburn  $j$  factor from Kang and Jun (2011) were used. First simulation compared the 3D numerical analysis of two-pitch louvered fin and the one

where thermodynamic porous medium model was applied. The comparison showed that while the predicted outlet temperature differs by less than one Celsius, the size of the volume element of the analysis with porous medium model decreases to about 1/200 of the usual method. Second simulation performed a numerical analysis of a compact heat exchanger containing louvered fin. Compared to the experimental results, it was observed that the error in the outlet temperatures of cooled air and coolant is within 2 degrees, and that the error in the pressure drop in the cooled air is less than 10%. Interestingly, if the compact heat exchanger used for verification of this study is modeled using previous method without applying the thermodynamic porous medium model, around 24.4 billion volume elements are required for louvered fin alone, while the application of thermodynamic porous medium model requires 2 million volume elements only. Moreover, since less than 10 million volume elements are required for a 3D numerical analysis of louvered fin, the performance prediction of compact heat exchanger with louvered fin is now possible using a 3D analysis. For future research, the permeability and Ergun constant can be determined for other fins that are commonly used in compact heat exchangers, so that these can correspond to the properties of porous medium. This will allow the field engineers to easily design heat exchangers or car air-conditioning and heating units with reduced design cost and development time, through free selection of fins and easy performance prediction through simulation.

**Keywords** : Louvered fin; Porous media approach; Permeability; Ergun constant; Compact heat exchanger; 3D Simulation

**Student Number** : 2010-31313

## Contents

|  |     |
|--|-----|
| Abstract .....   | i   |
| Contents .....   | iv  |
| List of Figures .....                                    | vii |
| List of Tables .....                                     | ix  |
| 1. Introduction .....                                    | 1   |
| 1.1 Motivation .....                                     | 1   |
| 1.2 Objectives .....                                     | 3   |
| 1.3 Outline of the thesis .....                          | 4   |
| 2. Heat transfer of around louvered fin .....            | 7   |
| 2.1 Previous study for louvered fin .....                | 7   |
| 2.2 Introduction to $\varepsilon$ -NTU/LMTD Method ..... | 10  |
| 2.2.1 Log Mean Temperature Difference (LMTD) .....       | 10  |
| 2.2.2 The Effectiveness-NTU Method .....                 | 13  |
| 3. Heat transfer in porous media .....                   | 16  |
| 3.1 Terminologies .....                                  | 16  |
| 3.2 (Modified) Darcy equation .....                      | 27  |
| 3.3 Local Thermal Equilibrium Approach .....             | 32  |
| 3.4 Local Non-thermal Equilibrium Approach .....         | 36  |
| 3.4.1 The local phase volume averaging .....             | 37  |
| 3.4.2 The heuristic two-medium treatments .....          | 40  |
| 3.5 Previous Study of Fin as Porous media .....          | 43  |

|   |     |
|---|-----|
| 4. Construction of Data Base for louvered fin.....                      | 45  |
| 4.1 Design for louvered fin .....                                       | 45  |
| 4.2 CFD results validation for louvered fin .....                       | 52  |
| 4.3 Construction of Data Base for louvered fin .....                    | 60  |
| 5. Statistical Treatment.....   | 65  |
| 5.1 Non-linear regression.....  | 65  |
| 5.2 Multi-linear regression.....  | 71  |
| 5.2.1 friction factor ( $f$ ) correlation .....                         | 71  |
| 5.2.2 Heat transfer coefficient (Colburn $j$ factor).....               | 73  |
| 5.3 Verification of present correlations .....                          | 75  |
| 5.3.1 Comparison of present correlation and Data-Base.....              | 75  |
| 5.3.2 Permeability and Ergun constant of louvered fin.....              | 77  |
| 5.4 Need to new friction correlation for louvered fin .....             | 80  |
| 6. Validation .....   | 82  |
| 6.1 Validation for louvered fin .....                                   | 82  |
| 6.2 Experimental Set up.....  | 87  |
| 6.3 Uncertainty Analysis.....   | 89  |
| 6.4 Validation for Compact Heat Exchanger with louvered fin.....        | 92  |
| 6.5 Comparison of CFD and 1D simulation using new $f$ correlation ..... | 105 |
| 7. Conclusion .....   | 108 |
| 7.1 Summary .....   | 108 |
| 7.2 Future work.....  | 116 |

|                           |     |
|---------------------------|-----|
| References .....          | 117 |
| Abstract (in Korean)..... | 120 |
| 감사의 글 .....               | 123 |

## List of Figures

- Fig. 1.1 CFD analysis to path design to radiator coolant
- Fig. 1.2 Heat and flow contours for louvered fin CFD analysis
- Fig. 1.3 Comparison of model for proto and numerical assumed by porous media treatment
- Fig. 2.1 Variation of the fluid temperatures in a parallel flow double-pipe heat exchanger
- Fig. 3.1 REV (Representative Element Volume)
- Fig. 3.2 Schematic of Darcy experiment
- Fig. 3.3 Schematic of Capillary model for porous media
- Fig. 3.4 Bundle of capillary tubes
- Fig. 3.5 Various capillary models for porous media
- Fig. 3.6 Friction factor for flow in a porous media
- Fig. 3.7 Schematic of flow regime for  $Re_D < 1$
- Fig. 3.8 Flow across a Bank of Tubes in a Narrow Gap
- Fig. 4.1 Design for louvered fin
- Fig. 4.2 Schematic for louvered-, Un-louvered regions
- Fig. 4.3 Duct- and Louvered- directed flow around louvered fin
- Fig. 4.4 Real flow around louvered fin
- Fig. 4.5 Flow visualization for around louvered fin
- Fig. 4.6 Pressure visualization for around louvered fin
- Fig. 4.7 Stanton number curves demonstrating transition from duct to flat-plate flow
- Fig. 4.8 Achaichia and Cowell' experiment model
- Fig. 4.9 Louvered plate fin model using Atkinson et al. study
- Fig. 4.10 Louvered plate fin without un-louvered region, (b) Louvered plate fin with louvered region

Fig. 4.11 Boundary conditions for louvered (plate) fin

Fig. 4.12  $f$  factor according to investors

Fig. 4.13  $St$  number according to investors

Fig. 4.14 Data Base for louvered fin' friction factor combined by experiment correlation and present CFD

Fig. 5.1 Classical correlations of friction factor for spheres immersed by bathe

Fig. 5.2 Friction factor distribution followed by new correlation equation about louvered fin

Fig. 5.3 Colburn  $j$  factor distribution followed by new correlation about louvered fin

Fig. 5.4 Comparison of friction factors between previous data and novel correlation of present study of louvered fin

Fig. 5.5 Permeability as a function of the Reynolds number for various louvered fin geometries

Fig. 5.6 Comparison of louvered fin friction factor according to wide range Reynolds number

Fig. 6.1 Boundary conditions for louvered fin

Fig. 6.2 Experimental Set up for Compact Heat Exchanger

Fig. 6.3 Computational domain for compact heat exchanger

Fig. 6.4 Volume grid for compact heat exchanger with louvered fin

Fig. 6.5 Comparison of experimental and numerical data according to mass flow of coolant and air

Fig. 6.6 Prediction of pressure drop according to friction models

Fig. 6.7 Comparison of 1D and 3D Simulation

Fig. 6.8 Comparison of Darcy- and Modified Darcy equation

## List of Tables

- Table 2.1 Various friction and dimensionless heat transfer coefficients
- Table 3.1 Comparison of permeability and porosity for various material
- Table 4.1 Test samples conducted by Achaichia and Cowell
- Table 4.2 Relation pressure drop passed in louvered fin and velocity for various friction models
- Table 4.3 Detail geometries information of louvered fin for present study
- Table 5.1  $C_1$  and  $C_2$  values
- Table 6.1 Comparison of Full 3D 2-pitch louvered fin and NEHT simulation
- Table 6.2 Capacity of Experimental apparatus
- Table 6.3 Number of cells for each region consist of compact heat exchanger
- Table 6.4 Louvered fin-tube parameters
- Table 6.5 Comparison of Experimental and Numerical data for compact heat exchanger with louvered fin



# 1. Introduction

## 1.1 Motivation

In corporate research activity, there is an increasing demand for computer-based design owing to the emphasis on shorter release time and stronger cost competitiveness. Also, in practice, computer-aided engineering (CAE) is actively used. Moreover, CAE is also commonly used in engine cooling and air-condition systems design for cars. Following the advances in hardware and software, prediction based on various physical models is possible, enhancing the cost and business competitiveness of the companies. While there are various components consisting of car engine cooling and passenger space air-conditioning systems, the design and implementation of heat exchanger is of particular importance to the thermal load system, in terms of heat transfer. Therefore, it is significantly important to be able to design a heat exchanger based on its predicted performance in the car thermal load system. Figures 1.1 and 1.2 show the examples of CAE for various heat exchangers. However, in the case of louvered fin-tube compact heat exchanger, where louvered fin is equipped for improved heat exchanger performance, it is nearly impossible to consider the louvered fin and tube simultaneously for a numerical analysis, due to the complexity of the geometry of louvered fin and fluid flow structure and the absence of vast numerical resources required for simulating louvered fin. As a simple example, one can estimate the number of lattices required to simulate a car radiator using a numerical analysis. Figure 1.3 shows a traditional car radiator model. In this model, there are 60 tubes and 61 louvered fins, with each fins consisting of typically 400 pitches. Since the number of lattices required resolving one pitch of a louvered fin is at the order of one million,

if the radiator model is simulated using current analysis methods, it is seen that around 24.4 billion cells are required for a louvered fin alone. Accordingly, it is observed that the analysis of louvered fin-tube compact heat exchanger using traditional numerical analysis methods is highly difficult for practical reasons. Therefore, a usual approach to the prediction of louvered fin-tube compact heat exchanger is based on 1D relationship. One of the common 1D approaches is  $\epsilon$ -NTU method. While this is a classical method, it is still used in the industry owing to its fast prediction and low computational requirements. However, since prediction is made using 1D relationship, additional models are required for friction coefficient ( $f$ ) and heat transfer coefficient ( $j$ ), and a correction factor is required to adjust the analysis result. Moreover, due to the limitations of 1D analysis, it is highly difficult to consider the change in performance with changes in heat exchanger geometry, and to deduce the flow structure and heat transfer distribution.

## 1.2 Objectives

As aforementioned, in a 3D numerical analysis of louvered fin-tube compact heat exchanger, it was observed that the modeling of louvered fin is highly difficult using traditional methods. Therefore, to solve this problem, a louvered fin is assumed to be a porous medium. A porous medium here refers to a hypothetical continuum that connects the solid part (louvered fin) that forms the louvered fin, and fluid part (the air that passes through louvered fin). This continuum can be characterized by permeability ( $K$ ), Ergun constant ( $C_E$ ), and intrinsic heat transfer coefficient ( $h_{sf}$ ). An example of the analysis model that a louvered fin is assumed as a porous medium can be seen in Figure 1.3. It is believed that 3D numerical analysis of louvered fin-tube heat exchanger will be possible if a louvered fin is assumed to be a porous medium, and that this will be very useful for an actual louvered fin-tube compact heat exchanger design, since the flow structure and heat distribution of the cooled air and working fluid can be predicted.

### 1.3 Outline of the thesis

The contents addressed in each section of this thesis are as follow.

In Section 2, the theory of louvered fin will be addressed. Various friction coefficients and heat transfer coefficients proposed for louvered fin models will be reviewed, and two methods of predicting the performance of compact heat exchanger will be introduced, including log mean temperature difference (LMTD) method and  $\varepsilon$ -NTU method. In Section 3, the theory of porous medium will be explained. First of all, important and frequently cited terms will be introduced. Then, the momentum equation within porous media, and two approaches regarding the energy within porous media will be explained.

In Section 4, a database for a louvered fin will be established in order to determine the intrinsic permeability and Ergun constant of louvered fin. The experiment and model as in Kang and Jun [1] will be used to establish the database, and the data unavailable from the experiment of Kang and Jun [1] will be obtained through CFD, so that the database covers 14 louvered fin models at Reynolds number from 0.001 to 30,000.

In Section 5, a new form of friction coefficient is assumed, and the friction coefficient of louvered fin as a porous medium is newly proposed, through the nonlinear and multilinear regression analyses on the database obtained in the previous section. Moreover, the permeability and Ergun constant of louvered fin is given as a function of fin parameter, through coefficient comparisons with the modified Darcy equation.

In Section 6, the permeability and Ergun constant, that reflect the properties as a porous medium, and the Colburn  $j$  factor as in Kang and Jun [1] will be used to perform a 3D numerical analysis on two-pitch louvered fin and a compact heat exchanger containing a louvered fin. The result is

compared with the experimental data, and the accuracy and efficacy of the model obtained from this study will be discussed.

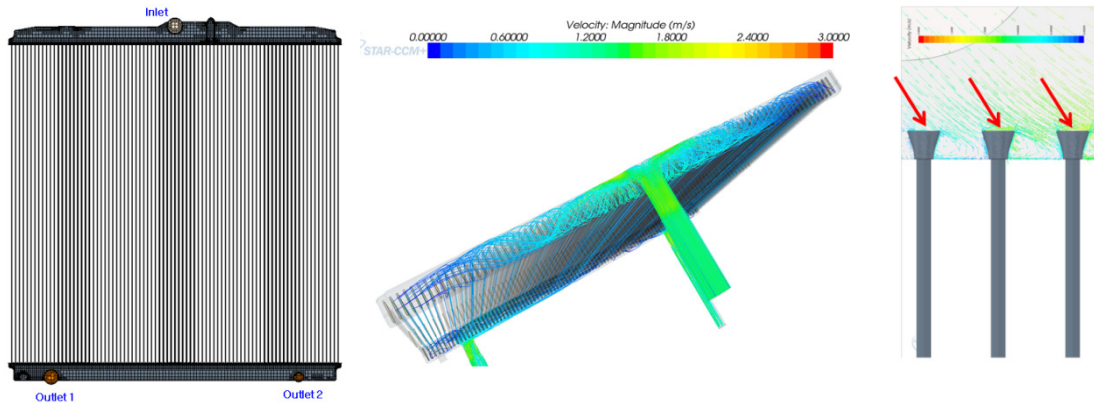


Fig. 1.1 CFD analysis to path design to radiator coolant

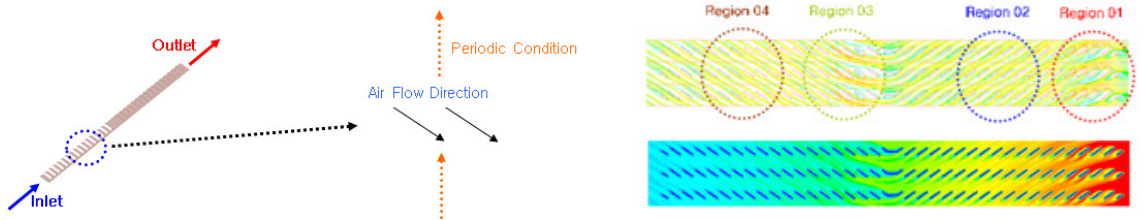


Fig. 1.2 Heat and flow contours for louvered fin CFD analysis

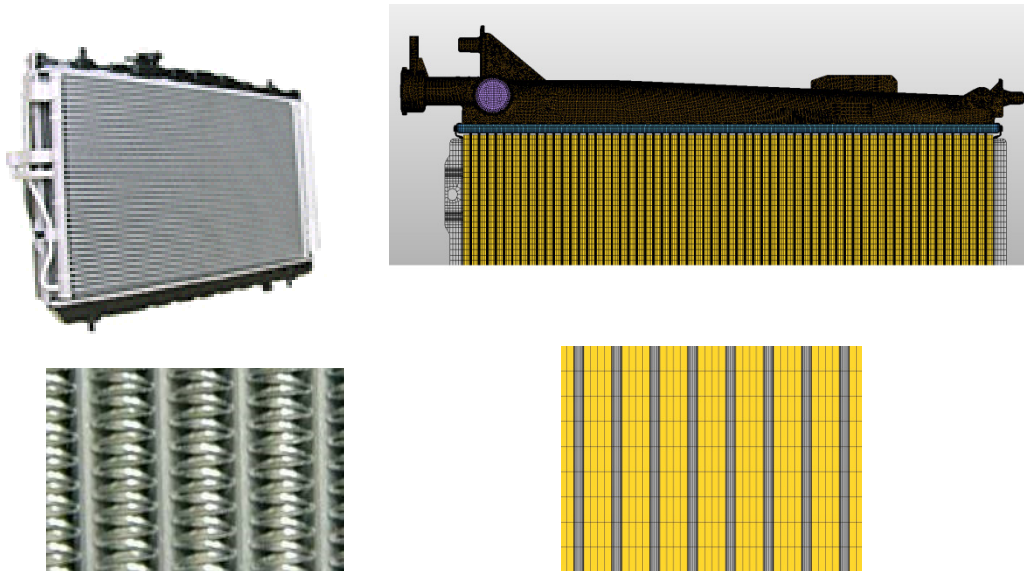


Fig. 1.3 Comparison model for proto and numerical assumed by porous zone treatment

## 2. Heat transfer of around louvered fin

### 2.1 Previous study for louvered fin

There are various applications of compact heat exchangers, ranging from micro- to macro-scale, and various fins exist for different applications. Fins commonly used in compact heat exchangers are of five main types, including offset fin, louvered fin, straight fin, pin fin, and wavy fin. However, in a compact heat exchanger for cars, a louvered fin is most commonly used. This is because a louvered fin is superior in terms of heat exchange amount and manufacturability compared to the other four types of fins. Since 1950s, research has been progressively conducted on the improvement of the performance of louvered fin by numerous researchers. Achaichia and Cowell[5] reported that the flow near the louvered fin has a transition from pipe flow to boundary flow as Reynolds number increases. Webb et al [6] showed that for offset strip fins and plain fins with equal hydraulic diameter, the heat transfer coefficient ( $j$ ) and friction coefficient ( $f$ ) of the offset fin showed a 2.5 fold and 3 fold increase compared to plain fins, respectively, at Reynolds number of 1000 with hydraulic diameter reference. Moreover, Pearson et al (1992)[7] reported that comparing plain fins and louver fins, the heat transfer coefficient ( $j$ ) and friction coefficient ( $f$ ) of louver fins increased 1.3 folds and 2.1 folds, respectively.

Davenport [8] obtained empirical equations by conducting an experiment based on 32 models comprising flat tubes and corrugated louvered fins with triangular, and this is shown in Table 2.1. Chang and Wang [2,3,4] proposed models for heat transfer coefficient ( $j$ ) and friction coefficient ( $f$ ) of louver fins, by using 91 models. In addition, Sudden and Svantesson [9] and Sahnoun and Webb et al [10] proposed models for heat transfer coefficient ( $j$ ) and friction coefficient ( $f$ ). Recently, Kang and Jun [1] proposed heat transfer coefficient ( $j$ ) and friction coefficient ( $f$ ) for 3-times magnified louvered fins, and representative models from numerous researchers are summarized in Table 2.1.

Table. 2.1 Various friction and dimensionless heat transfer coefficients

| Investor                     | Friction Model  | Heat Transfer Model  |
|------------------------------|---|--|
| Davenport (1983)             | $70 < \text{Re}_{D_h} < 900$<br>$f = 5.47 \text{Re}_{L_p}^{-0.72} \left( \frac{L_l}{H} \right)^{0.89} H^{0.23} L_p^{0.2} L_h^{0.37}$<br>$1000 < \text{Re}_{D_h} < 4000$<br>$f = 0.494 \text{Re}_{L_p}^{-0.39} \left( \frac{L_h}{H} \right)^{0.33} \left( \frac{L_l}{H} \right)^{1.1} H^{0.46}$                          | $300 < \text{Re}_{D_h} < 4000$<br>$j = 0.249 \text{Re}_{L_p}^{-0.42} (L_h)^{0.33} \left( \frac{L_l}{H} \right)^{1.1} (H)^{0.26}$   |
| Achaichia and Cowell (1988)  | $\text{Re}_{D_h} < 150$<br>$f = 10.4 \text{Re}_{L_p}^{-1.17} F_p^{0.04} L_p^{1.24} T_p^{0.83} L_h^{*0.25} L_h^* = L_p \sin \theta$<br>$150 < \text{Re}_{D_h} < 3000$<br>$f = 0.895 f_A^{1.07} F_p^{-0.22} L_p^{0.25} T_p^{0.26} L_h^{*0.33}$<br>$f_A = 596 \text{Re}_{L_p}^{(0.318 \log_{10}(\text{Re}_{L_p}) - 0.25)}$ | $150 < \text{Re}_{D_h} < 3000$<br>$St = 1.54 \text{Re}_{L_p}^{-0.57} \left( \frac{F_p}{L_p} \right)^{-0.19} \left( \frac{T_p}{L_p} \right)^{-0.11} \left( \frac{L_h^*}{L_p} \right)^{0.15}$<br>$L_h^* = L_p \sin \theta$             |
| Sunden and Svantesson (1992) | $100 < \text{Re}_{D_h} < 1000$<br>$f = 9.2 \text{Re}_{L_p}^{-0.54} \left( \frac{F_p}{L_p} \right)^{-0.022} \left( \frac{H}{L_p} \right)^{-1.085} \left( \frac{L_h}{L_p} \right)^{0.067} \left( \frac{F_d}{L_p} \right)^{0.31}$  | $100 < \text{Re}_{D_h} < 1000$<br>$St = 3.67 \text{Re}_{L_p}^{-0.591} \left( \frac{F_p}{L_p} \right)^{0.0206} \left( \frac{H}{L_p} \right)^{-0.285} \left( \frac{L_h}{L_p} \right)^{0.0671} \left( \frac{F_d}{L_p} \right)^{-0.243}$ |

| Investor              | Friction Model   | Heat Transfer Model  |
|-----------------------|--|--|
| Chang and Wang (1996) |  | $100 < \text{Re}_{L_p} < 1000$<br>$j = 0.436 \text{Re}_{L_p}^{-0.559} (\varepsilon)^{0.192} (\varepsilon_i)^{0.0956}$<br>$\varepsilon = \left( \frac{A_{tot}}{A_b} \right) \varepsilon_i = \left( \frac{A_i}{A_{tot}} \right)$   |
| Chang and Wang (1997) |  | $100 < \text{Re}_{L_p} < 3000$<br>$j = \text{Re}_{L_p}^{-0.49} \left( \frac{\theta}{90} \right)^{0.27} \left( \frac{F_p}{L_p} \right)^{-0.14} \left( \frac{H}{L_p} \right)^{-0.29} \left( \frac{T_d}{L_p} \right)^{-0.23}$<br>$\times \left( \frac{L_i}{L_p} \right)^{0.68} \left( \frac{T_p}{L_p} \right)^{-0.28} \left( \frac{t}{L_p} \right)^{-0.05}$ |
| Chang and Wang (1999) | $f = f_1 f_2 f_3$<br>$\text{Re}_{L_p} < 150$<br>$f_1 = 14.39 \text{Re}_{L_p}^{(-0.305 F_p / H)} (\ln(1.0 + (F_p / L_p)))^{3.04}$<br>$f_2 = \ln((t / F_p)^{0.48} + 0.9))^{-1.435} (D_h / L_p)^{-3.01} (\ln(0.5 \text{Re}_{L_p}))^{-3.01}$<br>$f_3 = (F_p / L_i)^{-0.308} (F_d / L_i)^{-0.308} (e^{(-0.1167 T_p / T_w)}) \theta^{0.35}$<br>$150 < \text{Re}_{L_p} < 5000$<br>$f_1 = 4.97 \text{Re}_{L_p}^{(0.5049 - 1.064 (\theta^{1.5}))} (\ln((t / F_p)^{0.5} + 0.9))^{-0.527}$<br>$f_2 = ((D_h / L_p) \ln(0.3 \text{Re}_{L_p}))^{-2.966} (F_p / L_i)^{-0.793} (T_p / (T_w - T_w))$<br>$f_3 = (T_p / T_w)^{-0.0446} \ln(1.2 + (L_p / F_p)^{1.4})^{-3.553} \theta^{-0.477}$ |  |

Table. 2.1 Various friction and dimensionless heat transfer coefficients



(Continue)

| Investor            | Friction Model  | Heat Transfer Model   |
|---------------------|---|---|
| Kang and Jun (2011) | $130 < \text{Re}_{L_z} < 800$<br>$f = 4.81 \text{Re}_{L_z}^{-0.622} (\cos \theta)^{-1.94} \left( \frac{L_p}{F_p} \right)^{0.233}$ | $130 < \text{Re}_{L_z} < 800$<br>$j = 4181 \text{Re}_{L_z}^{-0.698} \left( \frac{L_p}{F_p \cos \theta} \right)^{0.364}$ |

## 2.2 Introduction to $\epsilon$ -NTU/LMTD Method

As mentioned in Chapter 1, a 3D numerical analysis of louvered fin-tube heat exchanger is nearly impossible due to the lack of physical model and computational resources for modeling the louvered fin component. Therefore, as an alternative, the performance analysis for louvered-fin tube exchanger is possible through heat exchanger theory. Log mean temperature difference and  $\epsilon$ -NTU methods are used to predict the louvered fin-tube heat exchanger performance in heat exchanger theory, and these methods are introduced [11].

### 2.2.1 Log Mean Temperature Difference (LMTD)

There are mainly two methods of predicting the heat exchanger performance through theory. The first one is LMTD method, and the second one is  $\epsilon$ -NTU method. LMTD is a method of determining the heat exchanger when the mass flow rate and temperature differences between inlet and outlet (or heat transfer amount) are known, and  $\epsilon$ -NTU is a method of predicting the heat transfer amount and outlet temperature when the entrance temperature, mass flow rate, and heat exchanger specification are known. When the high-temperature and low-temperature parts of the heat exchanger exchanges heat as shown in Figure 2.1, LMTD is given by below.

Consider the differential area element  $dA_s$  of the low-temperature and high-temperature parts in Figure 2.1. The heat exchanger exchanges heat as much as  $\delta Q$  through area  $dA_s$ . Hence, the amount of heat exchange between low-temperature and high-temperature parts is given by Equations (2.1) and (2.2).

$$\delta Q = -\dot{m}_h C_{ph} dT_h \quad (2.1)$$

$$\delta Q = -\dot{m}_c C_{pc} dT_c \quad (2.2)$$

Where,

$$dT_h = -\frac{\delta Q}{\dot{m}_h C_{ph}} \quad dT_c = -\frac{\delta Q}{\dot{m}_c C_{pc}}$$

Meanwhile,

$$dT_h - dT_c = d(T_h - T_c) = -\frac{\delta Q}{\dot{m}_h C_{ph}} - \frac{\delta Q}{\dot{m}_c C_{pc}} = -\delta Q \left( \frac{1}{\dot{m}_h C_{ph}} + \frac{1}{\dot{m}_c C_{pc}} \right) \quad (2.3)$$

Since the heat transfer amount through differential area  $dA_s$  in heat exchanger is given by Equation (2.4):

$$\delta Q = U(T_h - T_c) dA_s$$

Therefore,

$$\begin{aligned} d(T_h - T_c) &= -\delta Q \left( \frac{1}{\dot{m}_h C_{ph}} + \frac{1}{\dot{m}_c C_{pc}} \right) \\ \frac{d(T_h - T_c)}{T_h - T_c} &= -U dA_s \left( \frac{1}{\dot{m}_h C_{ph}} + \frac{1}{\dot{m}_c C_{pc}} \right) \end{aligned}$$

Taking the integral from inlet to the outlet of the heat exchanger, Equation (2.4) is obtained.

$$\ln \frac{T_{h,out} - T_{c,out}}{T_{h,in} - T_{c,in}} = -UA_s \left( \frac{1}{\dot{m}_h C_{ph}} + \frac{1}{\dot{m}_c C_{pc}} \right) \quad (2.4)$$

Meanwhile, since

$$\begin{aligned} \dot{m}_h C_{ph} &= \frac{Q}{T_{h,in} - T_{h,out}} & \dot{m}_c C_{pc} &= \frac{Q}{T_{c,out} - T_{c,in}} \\ \ln \frac{T_{h,out} - T_{c,out}}{T_{h,in} - T_{c,in}} &= -\frac{UA_s}{Q} ((T_{h,in} - T_{h,out}) + (T_{c,out} - T_{c,in})) \\ \ln \frac{\Delta T_2}{\Delta T_1} &= -\frac{UA_s}{Q} (\Delta T_1 - \Delta T_2) \end{aligned}$$

Therefore,

$$Q = UA_s \frac{\Delta T_1 - \Delta T_2}{\ln \frac{\Delta T_1}{\Delta T_2}} = UA_s \Delta T_{lm} \quad (2.5)$$

Here, LMTD is defined as below:

$$\Delta T_{lm} = \frac{\Delta T_1 - \Delta T_2}{\ln \frac{\Delta T_1}{\Delta T_2}} \quad (2.6)$$

### 2.2.2 The Effectiveness-NTU Method

Unlike LMTD method,  $\varepsilon$ -NTU method determines the heat transfer amount and outlet temperature when the size, mass flow rate, and inlet temperature of the heat exchanger are known. To use this method, few terms and equations must be defined. First of all, heat transfer effectiveness,  $\varepsilon$ , is defined as in Equation (2.7).

$$\varepsilon = \frac{Q}{Q_{\max}} = \frac{\text{Actual heat transfer rate}}{\text{Maximum possible heat transfer rate}} \quad (2.7)$$

Moreover, the actual heat transfer amount in the heat exchanger is defined as in Equation (2.8).

$$Q = C_c (T_{c,out} - T_{c,in}) = C_h (T_{h,in} - T_{h,out}) \quad (2.8)$$

Where,

$$C_c = \dot{m}_c C_{pc}, C_h = \dot{m}_h C_{ph} : \text{Heat capacity rates}$$

The maximum heat transfer amount that can be collected in the heat exchanger is as in Equation (2.9).

$$\begin{aligned} \Delta T_{\max} &= T_{h,in} - T_{c,in} \\ Q &= C_{\min} (T_{h,in} - T_{c,in}) \end{aligned} \quad (2.9)$$

Here,

$$C_{\min} = \min[C_c, C_h]$$

Let us predict the radiated amount of heat and outlet temperature for parallel-flow heat exchanger using  $\varepsilon$ -NTU method.

By using the heat transfer effectiveness ( $\varepsilon$ ), maximum heat exchange amount (2.7), and the maximum heat transfer amount Equation (2.8), the heat transfer amount of the actual heat exchanger can be obtained by Equation (2.10).

$$Q = \varepsilon Q_{\max} = \varepsilon C_{\min} (T_{h,in} - T_{c,in}) \quad (2.10)$$

Therefore,

$$\ln \frac{T_{h,out} - T_{c,out}}{T_{h,in} - T_{c,in}} = -\frac{UA_s}{C_c} \left( 1 + \frac{C_c}{C_h} \right) \quad (2.11)$$

Meanwhile, since

$$Q = C_c (T_{c,out} - T_{c,in}) = C_h (T_{h,in} - T_{h,out})$$

Substituting this into (2.11),

$$\ln \frac{T_{h,in} - T_{c,in} + T_{c,in} - T_{c,out} - \frac{C_c}{C_h} (T_{c,out} - T_{c,in})}{T_{h,in} - T_{c,in}} = -\frac{UA_s}{C_c} \left( 1 + \frac{C_c}{C_h} \right)$$

Meanwhile, since

$$\varepsilon = \frac{Q}{Q_{\max}} = \frac{C_c (T_{c,out} - T_{c,in})}{C_{\min} (T_{h,in} - T_{c,in})} \quad \frac{T_{c,out} - T_{c,in}}{T_{h,in} - T_{c,in}} = \varepsilon \frac{C_{\min}}{C_c}$$

Therefore, from

$$\begin{aligned} \ln \left[ 1 - \left( 1 + \frac{C_c}{C_h} \right) \frac{T_{c,out} - T_{c,in}}{T_{h,in} - T_{c,in}} \right] &= -\frac{UA_s}{C_c} \left( 1 + \frac{C_c}{C_h} \right) \\ \exp \left[ -\frac{UA_s}{C_c} \left( 1 + \frac{C_c}{C_h} \right) \right] &= 1 - \left( 1 + \frac{C_c}{C_h} \right) \frac{T_{c,out} - T_{c,in}}{T_{h,in} - T_{c,in}} \\ \exp \left[ -\frac{UA_s}{C_c} \left( 1 + \frac{C_c}{C_h} \right) \right] &= 1 - \varepsilon \left( 1 + \frac{C_c}{C_h} \right) \frac{C_{\min}}{C_c} \end{aligned}$$

Hence, the heat transfer effectiveness in a parallel-flow heat exchanger is as below:

$$\varepsilon_{parallel\ flow} = \frac{1 - \exp\left[-\frac{UA_s}{C_c}\left(1 + \frac{C_c}{C_h}\right)\right]}{\left(1 + \frac{C_c}{C_h}\right)\frac{C_{\min}}{C_c}} \quad (2.12)$$

Equation (2.12) can be written in a simple form as in Equation (2.13).

$$\varepsilon_{parallel\ flow} = \frac{1 - \exp\left[-\frac{UA_s}{C_{\min}}\left(1 + \frac{C_{\min}}{C_{\max}}\right)\right]}{1 + \frac{C_{\min}}{C_{\max}}} \quad (2.13)$$

Here, number of transfer units (NTU) is defined as follows:

$$NTU = \frac{UA_s}{C_{\min}} = \frac{UA_s}{(\dot{m}C_p)_{\min}} \quad (2.14)$$

Therefore, from the definition of NTU, it is observed that the heat transfer amount increases with increasing NTU. It can also be deduced that, in general, heat transfer effectiveness is a function of NTU and heat capacity ratio ( $c$ ) as shown in Equation (2.15).

$$\varepsilon = function\left(\frac{UA_s}{C_{\min}}, \frac{C_{\min}}{C_{\max}}\right) = function(NTU, c) \quad \text{Where } c = \frac{C_{\min}}{C_{\max}}$$

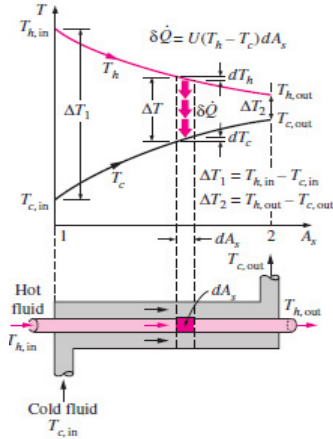
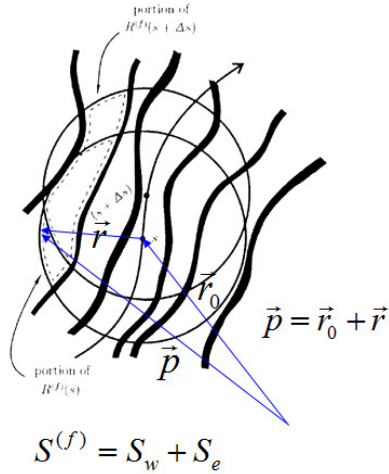


Fig. 2.1 Variation of the fluid temperatures in a parallel flow double-pipe heat exchanger

### 3. Heat transfer in porous media

It was shown in Sections 1 and 2 that it is extremely difficult to analyze the performance of a compact heat exchanger containing a louvered fin through computational fluid dynamics (CFD), due to the lack of computational resources and physical models. Therefore, in order to solve this problem, a louvered fin region is assumed to be a porous medium, and the performance of compact heat exchanger with a louvered fin is predicted through a 3D numerical analysis using appropriate friction and heat transfer models.

#### 3.1 Terminologies



In order to assume a louvered fin as a porous medium, few important concepts must be understood. A porous medium refers to a hypothetical continuum that assumes the solid and the fluid phases, such as the air passing through a louvered fin, to be one whole part. Here, similar to defining a test element volume in a fluid continuum for the

mathematical treatment of a hypothetical continuum, in a porous medium, representative element volume is defined as follows [12]:

Figure 3.1 REV (Representative Element Volume)



In order to represent the relative ratio between fluid and solid in REV, porosity can be defined as below. Here, porosity can be divided into true porosity and effective porosity.

· Porosity (true porosity or total porosity)

$$\mathcal{E}_t = \frac{V_{pores}}{V_{total}} = \frac{V_{total} - V_s}{V_{total}} = 1 - \frac{V_s}{V_{total}} = 1 - \frac{M_{total} / V_{total}}{M_{total} / V_s} \approx 1 - \frac{\rho_a}{\rho_s}$$

Here,

$V_{pores}$  : Pore volume,  $V_{total}$  : REV,  $V_s$  : Volume of solid in REV,  $M_{total}$  : Mass of REV,  $\rho_a$  : Apparent density,  $\rho_s$  : Solid density

· Effective porosity

$$\mathcal{E}_e = \frac{V_{interconnected\ pores}}{V_{total}}$$

Where,

$V_{interconnected\ pores}$  : Connected volume of non-isolated pores in REV

The study on fluid flow in a porous medium was formulated by Darcy during mid-18<sup>th</sup> century, and Figure 3.2 shows the schematic of the experimental apparatus used by Darcy.

## Generalization of Darcy's column

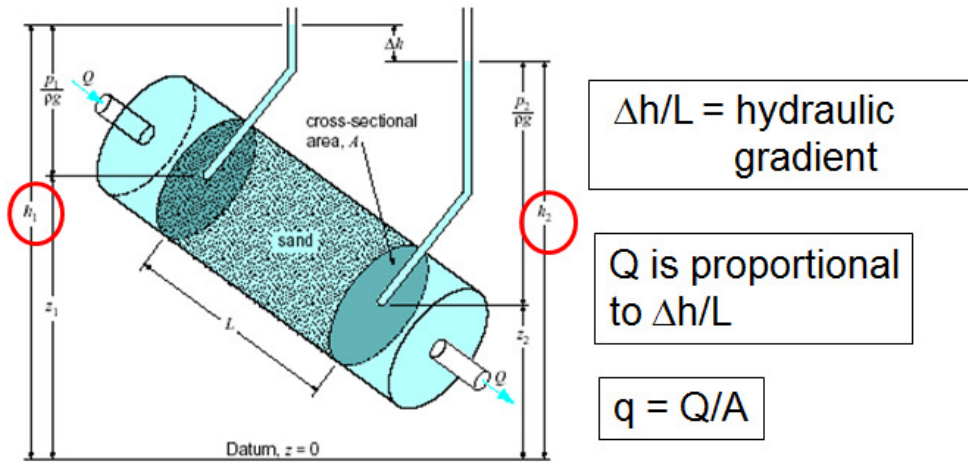


Figure from Hornberger et al. (1998)

Figure 3.2 Schematic of Darcy Experiment

Darcy obtained the below equation regarding flow rate and pressure gradient.

$$\frac{\Delta(p + \rho\phi)}{L} = \frac{\mu}{K} \frac{Q}{A} \quad (3.1)$$

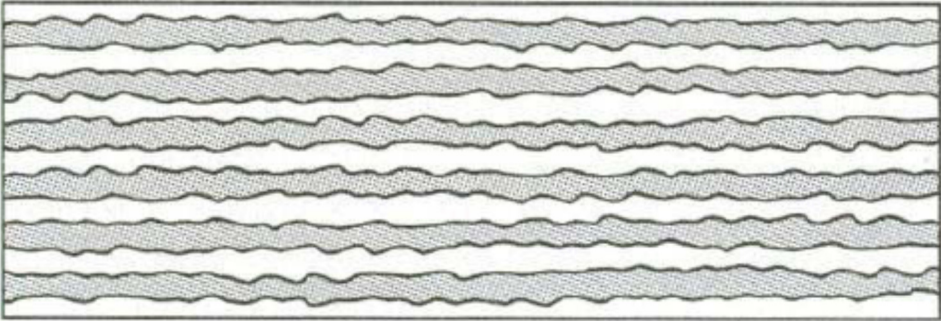
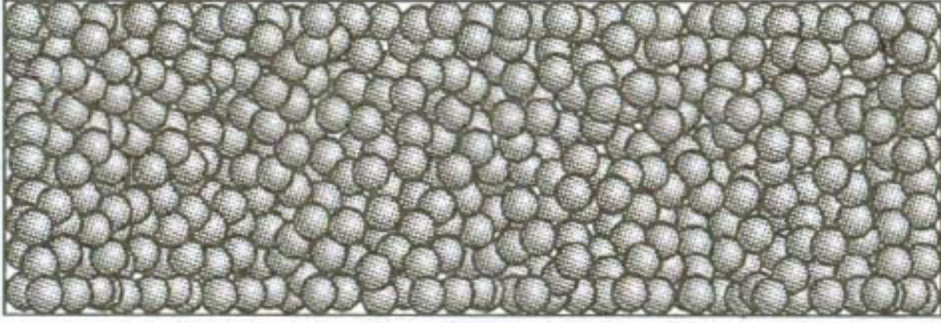
Where,  $\mu$  : viscosity,  $K$  : permeability,  $Q$  : flow rate,  $A$  : surface area

From Darcy equation, it can be seen that the Darcy velocity and pressure gradient between the two ends of the porous medium are linearly proportional to each other, and that permeability acts as conductance in Darcy equation. Namely, the pressure difference between the two ends of porous medium becomes smaller with greater permeability. Table 3.1 shows the example of porosity and permeability of various materials.

Table 3.1 Comparison of Porosity and Permeability according to various materials

| Material                                  | Porosity<br>$\phi$ | Permeability<br>$K$ [cm <sup>2</sup> ]        | Surface per unit<br>volume [cm <sup>-1</sup> ] |
|---|--------------------|---|--|
| Agar-agar                                 |                    | $2 \times 10^{-10}$ – $4.4 \times 10^{-9}$    |  |
| Black slate powder                        | 0.57–0.66          | $4.9 \times 10^{-10}$ – $1.2 \times 10^{-9}$  | $7 \times 10^3$ – $8.9 \times 10^3$            |
| Brick                                     | 0.12–0.34          | $4.8 \times 10^{-11}$ – $2.2 \times 10^{-9}$  |  |
| Catalyst (Fischer–Tropsch, granules only) | 0.45               |   | $5.6 \times 10^5$                              |
| Cigarette                                 |                    | $1.1 \times 10^{-5}$                          |  |
| Cigarette filters                         | 0.17–0.49          |   |  |
| Coal                                      | 0.02–0.12          |   |  |
| Concrete (ordinary mixes)                 | 0.02–0.07          |   |  |
| Concrete (bituminous)                     |                    | $1 \times 10^{-9}$ – $2.3 \times 10^{-7}$     |  |
| Copper powder (hot-compacted)             | 0.09–0.34          | $3.3 \times 10^{-6}$ – $1.5 \times 10^{-5}$   |  |
| Cork board                                |                    | $2.4 \times 10^{-7}$ – $5.1 \times 10^{-7}$   |  |
| Fiberglass                                | 0.88–0.93          |   | 560–770  |
| Granular crushed rock                     | 0.45               |   |  |
| Hair (on mammals)                         | 0.95–0.99          |   |  |
| Hair felt                                 |                    | $8.3 \times 10^{-6}$ – $1.2 \times 10^{-5}$   |  |
| Leather                                   | 0.56–0.59          | $9.5 \times 10^{-10}$ – $1.2 \times 10^{-9}$  | $1.2 \times 10^4$ – $1.6 \times 10^4$          |
| Limestone (dolomite)                      | 0.04–0.10          | $2 \times 10^{-11}$ – $4.5 \times 10^{-10}$   |  |
| Sand                                      | 0.37–0.50          | $2 \times 10^{-7}$ – $1.8 \times 10^{-6}$     | 150–220  |
| Sandstone ("oil sand")                    | 0.08–0.38          | $5 \times 10^{-12}$ – $3 \times 10^{-8}$      |  |
| Silica grains                             | 0.65               |   |  |
| Silica powder                             | 0.37–0.49          | $1.3 \times 10^{-10}$ – $5.1 \times 10^{-10}$ | $6.8 \times 10^3$ – $8.9 \times 10^3$          |
| Soil                                      | 0.43–0.54          | $2.9 \times 10^{-9}$ – $1.4 \times 10^{-7}$   |  |
| Spherical packings (well-shaken)          | 0.36–0.43          |   |  |
| Wire crimps                               | 0.68–0.76          | $3.8 \times 10^{-5}$ – $1 \times 10^{-4}$     | 29–40  |

In order to determine the Darcy velocity and pressure gradient in a porous medium, permeability must be obtained, which is the proportionality constant. In a classical perspective, there are three ways of obtaining permeability. First model of permeability is the capillary model. Capillary model replaces the pores with capillaries that correspond to the internal structure of the porous medium, and the model of permeability can be established relatively easily. In other words, by replacing the flow within a porous medium as pipe flow through multiple capillaries, the relationship between permeability, porosity, and Darcy velocity can be established.

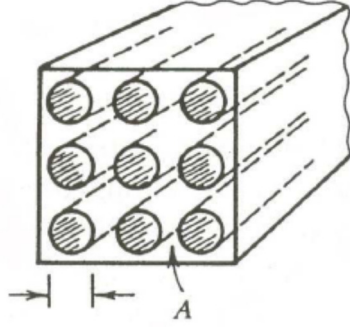


For example, approximating an arbitrary porous medium with a capillary model bundle as in Figure 3-4, and assuming each capillary to be a pipe with diameter  $d$ , the relationship between pore velocity ( $u_p$ ), diameter ( $d$ ), and pressure drop in a fully developed flow within a capillary is given by below:

$$u_p = \frac{d^2}{32\mu} \left( -\frac{dp}{dx} \right)$$

Meanwhile, by the relationship between Darcy velocity and pore velocity,

$$u_D = \varepsilon u_p = -\frac{n\pi d^4}{128\mu} \frac{dp}{dx} \quad (3.2)$$



$$n = \frac{N}{A}, \quad \varepsilon = n \cdot \frac{\pi d^2}{4}$$

Where,  $N$  is the number of capillaries and  $A$  is the surface area of the porous medium

Figure 3-4. Bundle of capillary tubes

By comparing Equation (3.2) with Darcy equation (3.1), the relationship between permeability ( $K$ ), capillarity diameter ( $d$ ), and porosity ( $\varepsilon$ ) can be obtained as below:

$$K = \frac{n\pi d^4}{128} \left( \because u_D = \frac{K}{\mu} \frac{\Delta p}{L} \right), \quad K = \frac{\varepsilon d^2}{32} \quad (3.3)$$

However, if the structure within a porous medium cannot easily be approximated with a simple capillary model, variations as shown in Figure 3-5 are used, which significantly reduces the accuracy and robustness of the capillary model.

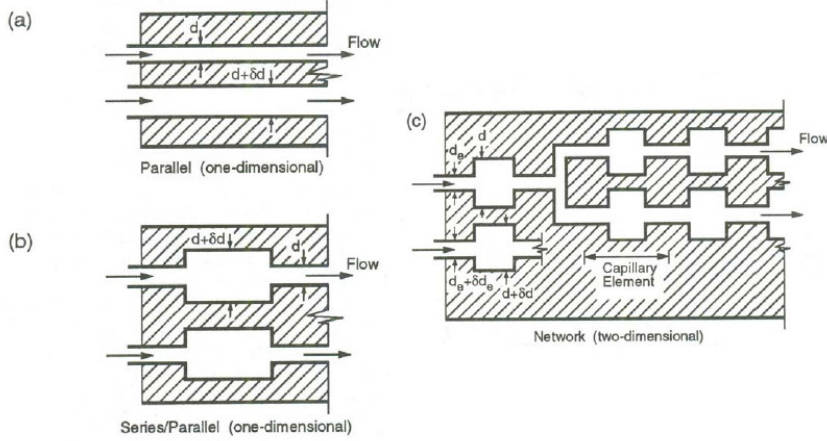


Figure 3-5. Various capillary models for porous media

The second model of permeability is the hydraulic radius model, which is a semi-heuristic approach. Here, the hydraulic radius is defined as follows:

$$r_h = \frac{A_c}{p} = \frac{\text{Cross section available for flow}}{\text{wetted perimeter}} = \frac{\text{volume available for flow} / V_{total}}{\text{total wetted surface} / V_{total}} = \frac{\varepsilon}{a_{sf}}$$

By defining the specific surface  $a_0$  as below:

$$a_0 = \frac{\text{total particle surface}}{\text{volume of particles}} = \frac{A_{sf}}{V_s} = \frac{A_{sf}}{V_{total}(1-\varepsilon)} = \frac{a_{sf}}{1-\varepsilon}$$

Hydraulic radius can be defined as follows:

$$d_h = 4r_h = \frac{4\varepsilon}{a_0(1-\varepsilon)} \quad (3.4)$$

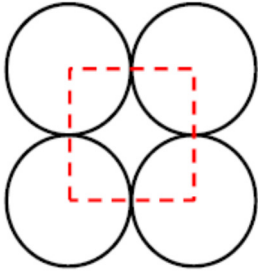
Here, using Hagen-Poiseuille equation for pipe flow through a pipe with hydraulic radius  $d_h$ , the following equation regarding pore velocity, hydraulic radius, and pressure drop is given:

$$u_p = \frac{d_h^2}{16k_k\mu} \left( -\frac{dp}{dx} \right) \quad (3.5)$$

Where,  $k_k$  is Kozeny constant, and for circular capillary  $k_k = 2$ .

Let us consider a case where a tank is filled with spherical particles with diameter  $d$ .

In this case, the specific area and hydraulic radius are given as follows:



$$a_0 = \frac{A_{sf}}{V_s} = \frac{4\pi r^2}{\frac{4}{3}\pi r^3} = \frac{6}{d}$$

$$d_h = \frac{4\varepsilon}{a_0(1-\varepsilon)} = \frac{2\varepsilon d}{3(1-\varepsilon)}$$

Here, permeability is as follows:

$$K = \frac{\varepsilon d_h^2}{16k_k} = \frac{\varepsilon^3}{36k_k(1-\varepsilon)^2} d^2$$

If Kozeny constant is 5, we obtain Carman-Kozeny equation as below:

$$K = \frac{\varepsilon^3}{180(1-\varepsilon)^2} d^2 \quad (3.6)$$

If Kozeny constant is  $25/6$ , we obtain Blake-Kozeny equation as below:

$$K = \frac{\varepsilon^3}{150(1-\varepsilon)^2} d^2 \quad (3.7)$$

Figure 3-6 describes the friction coefficient with increasing Reynolds number for the case where a tank is filled with spherical particles with diameter  $d$ . As shown in Figure 3-6, while it can be seen that for Reynolds number below 1, the friction coefficient decreases linearly with increasing Reynolds number, for Reynolds number above 1000, friction coefficient is a constant that is irrespective of Reynolds number, and for Reynolds number from 1 to 1000, friction coefficient changes nonlinearly with increasing Reynolds number. Hence, it is seen that for Reynolds number below 1, the permeability is constant, and that Darcy equation is in effect. However, if Reynolds number is greater than 1, permeability is no longer constant due to the increase in inertial force, and an additional inertial term is added to Darcy equation as it is not explained only with Darcy equation. Finally, if Reynolds number is greater than 1000, the effect of viscous force represented by Darcy equation is minimal, and friction coefficient is proportional to the square of Darcy velocity.



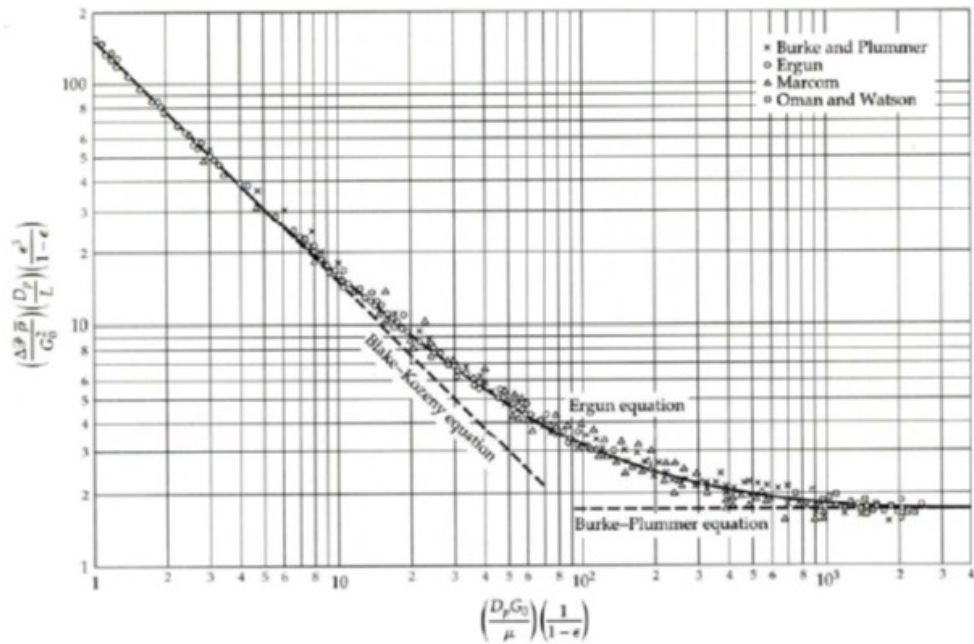
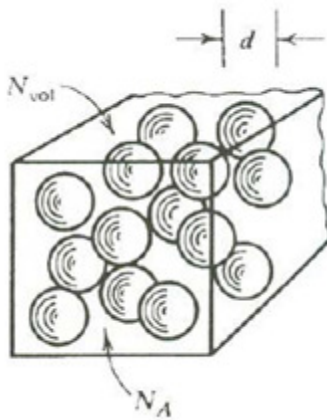


Figure 3-6. Friction factor for flow in a porous medium (Ward, 1964)

Third model of permeability is the drag model. In drag model, the porous medium is assumed to be filled with spherical particles. Here, the interaction between spherical particles is assumed to be sufficiently small. Hence, the drag coefficient for flow near spherical particles can be defined as follows. Yet, the flow is assumed to be a creeping flow, where Reynolds number is significantly small.



$$C_D = \frac{F}{\left(\frac{\pi d^2}{4}\right) \left(\frac{\rho u_p^2}{2}\right)} = \frac{24}{\text{Re}} = \frac{24\nu}{u_p d}$$

Here, since there is force equilibrium between the drag force on spherical particles and pressure drop in the fluid, below equation can be obtained:

$$\Delta p \cdot A = F (N_{vol.} \cdot AL)$$

Meanwhile, the solution to Stoke's flow is known to be as below:

$$F = 3\pi\mu du_p$$

Therefore, below equation can be obtained:

$$\frac{\Delta p}{L} = N_{vol.} \cdot 3\pi\mu du_p = \frac{\mu}{K} u_p \varepsilon \quad (3.8)$$

Where,

$$K = \frac{\varepsilon}{N_{vol.} 3\pi d} \quad (3.9)$$

However, since in a drag model, it is assumed that there is a minimal interaction between the spherical particles consisting a porous medium, it can used for a porous medium with scarce pores in its interior. In this study, a semi-heuristic approach and modified Darcy equation were used to define permeability.

### 3.2 (Modified) Darcy equation

As mentioned in Section 3.1, Darcy equation is the momentum equation for flow governed by viscous force with Reynolds number less than 1. However, if Reynolds number is greater than 1, it is seen that the effect of inertia must be considered because of the properties of porous medium. From the visualization results from Dybbs and Edwards [13] and Masuoka [14], the flow pattern within a porous medium with increasing Reynolds number can be known.

If Reynolds number is less than 1, it can be observed that the viscous force is much greater than inertial force, with inlet length about 3 times greater than the diameter of the spherical particles because of the properties of porous media. Moreover, the channeling effect near the wall is around 1-2 times greater than the diameter of the spherical particles. Figure 3-7 shows the approximate velocity distribution when Reynolds number is less than 1. Here, the average velocity does not consider no-slip condition. In other words, the velocity is not 0 at the wall. Since there is a contact with the spherical particles at the wall, the porosity at the plane where spherical particle contacts the wall is 1, but decreases closer to the center. Hence, near the wall, the flow behaves as if it passes through a channel, and this is referred to as a channeling effect.

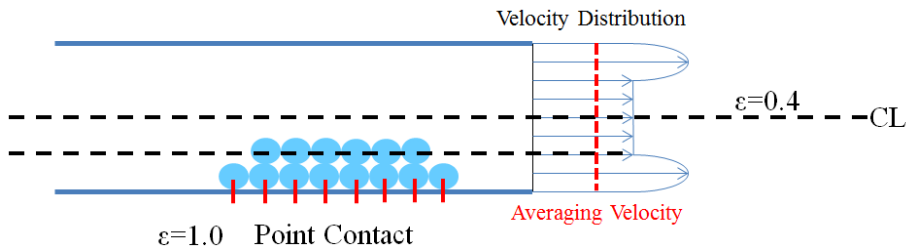
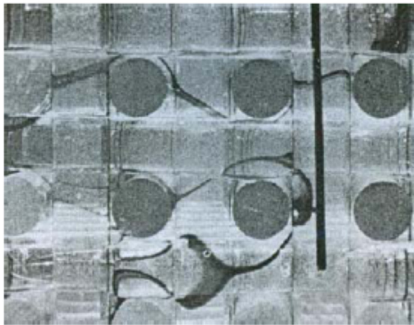


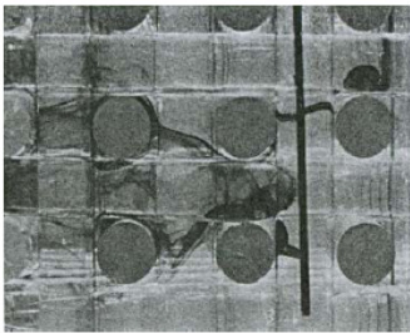
Figure 3-7. Schematic of flow regime for  $Re_D < 1$

For Reynolds number from 1 to 150, the flow characteristics inside a porous medium are as below. Inertial force is greater than viscous force as Reynolds

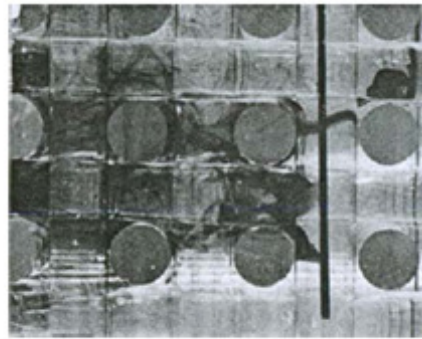
number is greater than 1, and it can be seen that boundary layer and streamline are formed along the spherical particle. Yet, flow is still laminar. However, for Reynolds number from 150 to 300, it is seen that the mixing with streamline also exists. Furthermore, for Reynolds number greater than 300, strong mixing and turbulent effects can be observed, and from here onwards can be classified as turbulent flow.



$Re = 86 \pm 16$ ,  $I = 2 \times 0.30$  cc/min



$Re = 225 \pm 15$ ,  $I = 2 \times 2.2$  cc/min



$Re = 305 \pm 13$ ,  $I = 2 \times 4.4$  cc/min

Similar research has been conducted by Masuoka [14], where flow visualization result was obtained as below.

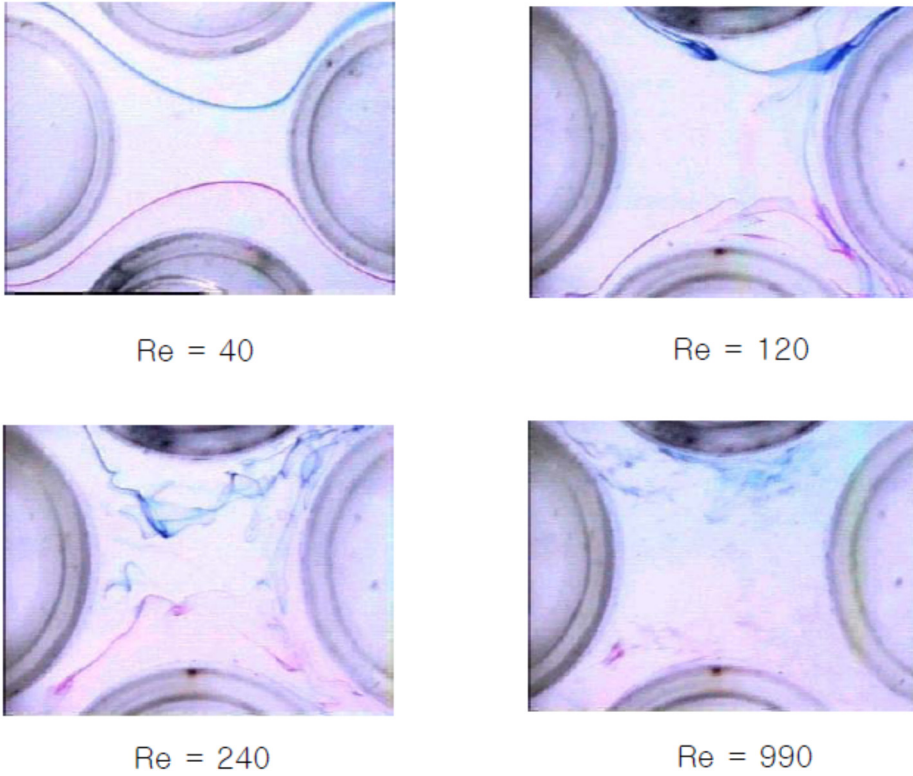


Figure 3-8. Flow across a Bank of Tubes in a Narrow Gap (Masuoka, 1996)

Therefore, the momentum equation inside a porous medium can be classified into four main models. First model is when Reynolds number is less than 1, and viscous force is dominant, of which the momentum equation is Darcy equation.

$$\nabla p = -\frac{\mu_f}{K} \vec{u}_D \quad (3.10)$$

Since Equation (3-10) is the relationship between Darcy velocity, which is the average velocity, and pressure drop, it does not satisfy the no-slip condition at the wall. Therefore, to satisfy the no slip condition at the wall, viscous term is added to Darcy equation, which is given by Brinkman equation [15,16], as below:

$$\nabla p = -\frac{\mu_f}{K} \vec{u}_D + \mu_{eff} \nabla^2 \vec{u}_D \quad (3.11)$$

Where,

$$\mu_{eff} = \mu_f \left[ 1 + 2.5(1 - \varepsilon) \right]$$

If the permeability increases significantly and porosity approaches 1, Brinkman equation becomes momentum equation for Stokes flow, and if permeability approaches zero, Brinkman equation becomes Darcy equation. The third momentum equation for a porous medium is modified Darcy equation. As aforementioned,, even if the Reynolds number is greater than 1 due to the flow characteristics within porous medium, the inertial force is appreciably greater than viscous force. Therefore, to be applied in an actual engineering situation, the effect of inertial force must be considered. Hence, the model with inertial force term added to Darcy equation is the modified Darcy equation, or the Forchheimer equation, which is as below [17,18].

$$\nabla p = -\frac{\mu_f}{K} \vec{u}_D - \frac{C_E}{\sqrt{K}} \rho \vec{u}_D^2 \quad (3.12)$$

Finally, governing equation inside porous media, which considers all of viscous force, inertial force, and no-slip condition at the wall, is the Brinkman-Forchheimer-Extended Darcy equation as below:

$$\nabla p = -\frac{\mu_f}{K} \vec{u}_D + \mu_{eff} \nabla^2 \vec{u}_D - \frac{C_E}{K^{1/2}} \rho |\vec{u}_D| \vec{u}_D \quad (3-13)$$

In this study, modified Darcy equation was used as the momentum equation for a porous medium that describes the louvered fin.

### 3.3 Local Thermal Equilibrium Approach

In order to treat the solid and fluid that form REV as a hypothetical continuum, the concept of porous medium was introduced. For heat inside such porous media can be treated with two different approaches. When the heat capacity and thermal conductivity of the solid and fluid are not significantly different, a local thermal equilibrium approach is possible. In other words, the solid and fluid inside the REV have the same representative temperature. In order to develop the local thermal equilibrium approach and local thermal non-equilibrium approach in the following discussions, we define some equations including the definition of phase average. Phase average of, which can be a scalar, a vector, or a tensor, is defined in three types:

$$\langle \psi \rangle \equiv \frac{1}{V} \int_V \psi dV \quad (3.14)$$

$$\bar{\psi}^\alpha \equiv \frac{1}{V} \int_{V_\alpha} \psi dV \quad (3.15)$$

$$\langle \psi \rangle^\alpha \equiv \frac{1}{V_\alpha} \int_{V_\alpha} \psi dV \quad (3.16)$$

Here, Equation (3-14) is the simple volume average, Equation (3-15) is the superficial volume average, and Equation (3-16) is the intrinsic volume average. Superficial and intrinsic volume averages are appropriately used for phase average within porous media. Moreover, there are two theorems regarding phase average. First is the theorem for the volume average of a gradient, and is as below:

$$\langle \nabla \psi \rangle = \nabla \langle \psi \rangle + \frac{1}{V} \int_{A_{sf}} \psi \hat{n} dA \quad (3.17)$$



Second theorem is the theorem for the volume average of a divergence. For a vector or a second order tensor, the second theorem can be described as below:

$$\langle \nabla \cdot \vec{b} \rangle = \nabla \cdot \langle \vec{b} \rangle + \frac{1}{V} \int_{A_{sf}} \vec{b} \cdot \hat{n} dA \quad (3.18)$$

Moreover, the generalized transport theorem inside porous media is as below (Slattery, 1999)[18].

$$\frac{d}{dt} \int_V \psi dV = \int_V \frac{\partial \psi}{\partial t} dV + \int_A \psi \vec{u}_A \cdot \hat{n} dA \quad (3.19)$$

Where,  $\vec{u}_A$  is the velocity at surface area  $A(t)$ , and  $\hat{n}$  is a unit vector normal to  $A(t)$ . Therefore, by using the definitions of phase average as introduced above, and the local thermal equilibrium approach, the energy equation inside REV can be derived. The heat conduction equation for solid and fluid phases inside REV is as below:

$$\begin{aligned} (\rho c_p)_f \frac{\partial T_s}{\partial t} &= \nabla \cdot k_f \nabla T_f \quad \text{in } V_f \\ (\rho c_p)_s \frac{\partial T_s}{\partial t} &= \nabla \cdot k_s \nabla T_s \quad \text{in } V_s \end{aligned}$$

Since the temperature and heat flux at the phase boundary  $A_{sf}$  must be equal:

$$\begin{aligned} T_f &= T_s \\ \hat{n}_{fs} \cdot k_f \nabla T_f &= \hat{n}_{fs} \cdot k_s \nabla T_s \end{aligned}$$

Moreover, by taking the phase average for each phase, Equations (3-17) and (3-18) can be obtained for fluid and solid phases, and (3-19) for the boundary:

$$(\rho c_p)_f \varepsilon \frac{\partial \langle T \rangle^f}{\partial t} = k_f \nabla \cdot \varepsilon \nabla \langle T \rangle^f + \nabla \cdot \frac{k_f}{V} \int_{A_{fs}} \hat{n}_{fs} T_f' dA + \frac{1}{V} \int_{A_{fs}} \hat{n}_{fs} \cdot k_f \nabla T_f dA \quad (3.17)$$

$$\begin{aligned}
(\rho c_p)_s (1-\varepsilon) \frac{\partial \langle T \rangle^s}{\partial t} &= \nabla \cdot k_s \langle T \rangle^s \nabla (1-\varepsilon) + \nabla \cdot k_s (1-\varepsilon) \nabla \langle T \rangle^s \\
&+ \nabla \cdot \frac{k_s}{V} \int_{A_{fs}} \hat{n}_{sf} T_s dA + \frac{1}{V} \int_{A_{fs}} k_s \nabla T_s \cdot \hat{n}_{fs} dA
\end{aligned} \tag{3.18}$$

And at the boundary  $A_{sf}$ :

$$\begin{aligned}
T_f' &= T_s' \\
\hat{n}_{fs} \cdot (k_f \nabla T_f - k_s \nabla T_s) &= 0
\end{aligned} \tag{3.19}$$

Summing Equations (3-17) and (3-18) and applying boundary conditions (3-19) yields:

$$\left[ (\rho c_p)_f \varepsilon + (\rho c_p)_s (1-\varepsilon) \right] \frac{\partial \langle T \rangle}{\partial t} = \nabla \cdot \left\{ \left[ \varepsilon k_f + (1-\varepsilon) k_s \right] \nabla \langle T \rangle + \frac{k_f - k_s}{V} \int_{A_{fs}} \hat{n}_{fs} T_f' dA \right\}$$

Here, constitutive equation is given as follows (Nozad et al. (1985)[19]):

$$\begin{aligned}
T_f' &= \hat{b}_f \cdot \nabla \langle T \rangle \\
T_s' &= \hat{b}_s \cdot \nabla \langle T \rangle
\end{aligned}$$

Therefore, the heat conduction equation using a local thermal equilibrium approach is as follows:

$$\left[ \varepsilon (\rho c_p)_f + (1-\varepsilon) (\rho c_p)_s \right] \frac{\partial \langle T \rangle}{\partial t} = \nabla \cdot (\bar{\bar{K}}_e \cdot \nabla \langle T \rangle) \text{ in } V \tag{3.20}$$

Here,

$$\bar{\bar{K}}_e = \left[ \varepsilon k_f + (1-\varepsilon) k_s \right] \bar{I} + \frac{k_f - k_s}{V} \int_{A_{fs}} \hat{n}_{fs} \hat{b}_f dA$$

In a similar manner, the governing equation for convection heat transfer using a local thermal equilibrium approach can be derived as follows:

$$\left[ \varepsilon (\rho c_p)_f + (1 - \varepsilon) (\rho c_p)_s \right] \frac{\partial \langle T \rangle}{\partial t} + (\rho c_p)_f \vec{u}_D \cdot \nabla \langle T \rangle = (\rho c_p)_f \nabla \cdot (\overline{\overline{D}} \cdot \nabla \langle T \rangle) \text{ in } V \quad (3.21)$$

Here,

$\overline{\overline{D}}$ : Total diffusivity tensor, defined as:

$$\overline{\overline{D}} = \frac{\overline{\overline{K_e}}}{(\rho c_p)_f} + \varepsilon \overline{\overline{D}}^d$$

.

### 3.4 Local Non-thermal Equilibrium Approach

As aforementioned, the energy equation within a porous medium allows two different approaches. There is a local thermal equilibrium approach, where average temperatures of solid and fluid inside the porous medium are assumed to be equal, as in Section 3.3. In this approach, there is only one energy equation inside porous medium, since the average temperatures of solid and fluid are assumed to be equal. Therefore, less computational resources are required for calculation. However, if the ratios of heat capacity or conductivity between solid and fluid are large, or certain phase forming a porous medium generates heat, then the thermal equilibrium approach is inappropriate. The cases where thermal equilibrium approach is appropriate are extremely limited. Typical example of the case where ratios of heat capacity and conductivity of each phase are small and there is no heat generation is insulation materials. In most applications, and in particular in louvered fin with porosity assumption, the ratios of heat capacity and conductivity between air and aluminum are significantly large, and thus the energy equation inside a porous medium must be solved through a thermal non-equilibrium approach.

There are two ways of deriving the energy equation for a porous medium using a thermal non-equilibrium approach. First way is to obtain the energy equation in a mathematical way through phase average, and the second way is to obtain the energy through a semi-heuristic approach.

### 3.4.1 The local phase volume averaging

Let us assume that the porous medium consists of aluminum, which is solid, and air, which is fluid. Then, the energy equation for each phase in a porous medium is as below:

$$(\rho c_p)_f \left( \frac{\partial T_f}{\partial t} + \vec{u}_f \cdot \nabla T_f \right) = \nabla \cdot k_f \nabla T_f \quad \text{in } V_f \quad (3.22)$$

$$(\rho c_p)_s \frac{\partial T_s}{\partial t} = \nabla \cdot k_s \nabla T_s \quad \text{in } V_s \quad (3.23)$$

At the boundary  $A_{sf}$ :

$$T_f = T_s$$

$$\hat{n}_{fs} \cdot k_f \nabla T_f = \hat{n}_{fs} \cdot k_s \nabla T_s$$

By taking the phase average for the liquid phase, below equation is obtained:

$$\begin{aligned} & (\rho c_p)_f \left( \frac{\partial \langle T \rangle^f}{\partial t} + \langle \vec{u} \rangle^f \cdot \nabla \langle T \rangle^f \right) \\ &= \nabla \cdot \left( k_f \nabla \langle T \rangle^f + \frac{k_f}{V_f} \int_{A_{fs}} \hat{n}_{fs} T'_f dA \right) - (\rho c_p)_f \nabla \cdot \langle \vec{u}' T' \rangle^f + \frac{1}{V_f} \int_{A_{fs}} \hat{n}_{fs} \cdot k_f \nabla T'_f dA \end{aligned} \quad (3.24)$$

In a similar manner, taking the phase average of the solid phase, the energy equation for solid phase is obtained as below:

$$(\rho c_p)_s \frac{\partial \langle T \rangle^s}{\partial t} = \nabla \cdot \left( k_s \nabla \langle T \rangle^s + \frac{k_s}{V_s} \int_{A_{fs}} \hat{n}_{sf} T'_s dA \right) + \frac{1}{V_s} \int_{A_{fs}} \hat{n}_{sf} \cdot k_s \nabla T'_s dA \quad (3.25)$$

At the boundary,  $A_{sf}$ :  $T'_f = T'_s + (\langle T \rangle^s - \langle T \rangle^f)$

$$\hat{n}_{fs} \cdot k_f \nabla T'_f = \hat{n}_{fs} \cdot k_s \nabla T'_s + \hat{n}_{fs} \cdot (k_s \nabla \langle T \rangle^s - k_f \nabla \langle T \rangle^f)$$

Meanwhile, from Equations (3.24) and (3.25), the constitutive equation for  $T'$  is:

$$T'_f = \vec{b}_{ff} \cdot \nabla \langle T \rangle^f + \vec{b}_{fs} \cdot \nabla \langle T \rangle^s + \psi_f \left( \langle T \rangle^s - \langle T \rangle^f \right)$$

$$T'_s = \vec{b}_{ss} \cdot \nabla \langle T \rangle^s + \vec{b}_{sf} \cdot \nabla \langle T \rangle^f + \psi_s \left( \langle T \rangle^s - \langle T \rangle^f \right)$$

Therefore, substituting and simplifying these equations, the energy equation for fluid phase is given by below:

$$\begin{aligned} & \frac{\partial \langle T \rangle^f}{\partial t} + \left[ \langle \vec{u} \rangle^f + \alpha_f \frac{A_{fs}}{V_f} \left( 2 \langle \hat{n}_{fs} \psi_f \rangle^{fs} - \langle \hat{n}_{fs} \cdot \nabla \vec{b}_{ff} \rangle^{fs} \right) - \langle \vec{u}' \psi_f \rangle^f \right] \cdot \nabla \langle T \rangle^f \\ & + \left[ \alpha_f \frac{A_{fs}}{V_f} \left( -2 \langle \hat{n}_{fs} \psi_f \rangle^{fs} - \langle \hat{n}_{fs} \cdot \nabla \vec{b}_{fs} \rangle^{fs} \right) + \langle \vec{u}' \psi_f \rangle^f \right] \cdot \nabla \langle T \rangle^s \\ & = \nabla \cdot \left[ \alpha_f \left( I + 2 \frac{A_{fs}}{V_f} \langle \hat{n}_{fs} \vec{b}_{ff} \rangle^{fs} \right) - \langle \vec{u}' \vec{b}_{ff} \rangle^f \right] \cdot \nabla \langle T \rangle^f + \nabla \cdot \left( 2 \alpha_f \frac{A_{fs}}{V_f} \langle \hat{n}_{fs} \vec{b}_{fs} \rangle^{fs} - \langle \vec{u}' \vec{b}_{fs} \rangle^{fs} \right) \cdot \nabla \langle T \rangle^s \\ & + \alpha_f \frac{A_{fs}}{V_f} \langle \hat{n}_{fs} \cdot \nabla \psi_f \rangle^{fs} \left( \langle T \rangle^s - \langle T \rangle^f \right) \end{aligned} \quad (3.26)$$

Similarly, the energy equation for solid phase is as below:

$$\begin{aligned} & \frac{\partial \langle T \rangle^s}{\partial t} + \left[ \alpha_s \frac{A_{fs}}{V_s} \left( 2 \langle \hat{n}_{sf} \psi_s \rangle^{fs} - \langle \hat{n}_{sf} \cdot \nabla \vec{b}_{sf} \rangle^{fs} \right) \right] \cdot \nabla \langle T \rangle^f + \left[ \alpha_s \frac{A_{fs}}{V_s} \left( -2 \langle \hat{n}_{sf} \psi_s \rangle^{fs} - \langle \hat{n}_{sf} \cdot \nabla \vec{b}_{ss} \rangle^{fs} \right) \right] \cdot \nabla \langle T \rangle^s \\ & = \nabla \cdot \left[ \alpha_s \left( I + 2 \frac{A_{fs}}{V_s} \langle \hat{n}_{sf} \vec{b}_{ss} \rangle^{fs} \right) \right] \cdot \nabla \langle T \rangle^s + \nabla \cdot \left( 2 \alpha_s \frac{A_{fs}}{V_s} \langle \hat{n}_{sf} \vec{b}_{sf} \rangle^{fs} \right) \cdot \nabla \langle T \rangle^f + \alpha_s \frac{A_{fs}}{V_s} \langle \hat{n}_{sf} \cdot \nabla \psi_s \rangle^{fs} \left( \langle T \rangle^s - \langle T \rangle^f \right) \end{aligned} \quad (3.27)$$

At the boundary,  $A_{sf}$ :

$$\begin{aligned} k_f \langle \hat{n}_{fs} \cdot \nabla \psi \rangle^{fs} &= -k_s \langle \hat{n}_{sf} \cdot \nabla \psi_s \rangle^{fs} \\ k_f \langle \hat{n}_{fs} \cdot \nabla \vec{b}_{fs} \rangle^{fs} &= -k_s \langle \hat{n}_{sf} \cdot \nabla \vec{b}_{ss} \rangle^{fs} \\ k_f \langle \hat{n}_{fs} \cdot \nabla \vec{b}_{ff} \rangle^{fs} &= -k_s \langle \hat{n}_{sf} \cdot \nabla \vec{b}_{sf} \rangle^{fs} \\ \langle \hat{n}_{fs} \psi_f \rangle^{fs} &= -\langle \hat{n}_{sf} \psi_s \rangle^{fs} \\ \langle \hat{n}_{fs} \vec{b}_{ff} \rangle^{fs} &= -\langle \hat{n}_{sf} \vec{b}_{sf} \rangle^{fs} \\ \langle \hat{n}_{fs} \vec{b}_{fs} \rangle^{fs} &= -\langle \hat{n}_{sf} \vec{b}_{ss} \rangle^{fs} \end{aligned}$$

Here,

$$\langle \rangle^{fs} \equiv \frac{1}{A_{fs}} \int_{A_{fs}} ( ) dA$$

By simplifying the equations into a more concise form, finally, the following equation is obtained:

$$\begin{aligned} \frac{\partial \langle T \rangle^f}{\partial t} + \bar{v}_{ff} \cdot \nabla \langle T \rangle^f + \bar{v}_{fs} \cdot \nabla \langle T \rangle^s &= \nabla \cdot \bar{\bar{D}}_{ff} \cdot \nabla \langle T \rangle^f + \nabla \cdot \bar{\bar{D}}_{fs} \cdot \nabla \langle T \rangle^s + \frac{A_{fs}}{V_{fs}(\rho c_p)_f} h_{sf} (\langle T \rangle^s - \langle T \rangle^f) \\ \frac{\partial \langle T \rangle^s}{\partial t} + \bar{v}_{sf} \cdot \nabla \langle T \rangle^f + \bar{v}_{ss} \cdot \nabla \langle T \rangle^s &= \nabla \cdot \bar{\bar{D}}_{sf} \cdot \nabla \langle T \rangle^f + \nabla \cdot \bar{\bar{D}}_{ss} \cdot \nabla \langle T \rangle^s + \frac{A_{fs}}{V_s(\rho c_p)_s} h_{sf} (\langle T \rangle^f - \langle T \rangle^s) \end{aligned} \quad (3.28)$$

$\bar{\bar{D}}_{ff}, \bar{\bar{D}}_{ss}, \bar{\bar{D}}_{fs}, \bar{\bar{D}}_{sf}$  : Total thermal diffusivity tensors

$h_{sf}$  : The interfacial convective heat transfer coefficient

$$h_{sf} = k_f \langle \hat{n}_{fs} \cdot \nabla \psi_f \rangle^{fs} = -k_s \langle \hat{n}_{sf} \cdot \nabla \psi_s \rangle^{fs}$$

Equation (3.28) is obtained by taking the phase average in energy equation in each phase of the porous medium. The energy transfer between solid and liquid phases is done through the last term of the governing equation. However, since Equation (3.28) is much more complicated compared to the original governing equations (3.22) and (3.23) and has many tensor terms that must be pre-determined, there is a significant limitation for practical applications. Therefore, in the next section, another approach is introduced, that solves these problems while conforming to a thermal non-equilibrium approach.

### 3.4.2 The heuristic two-medium treatments

The governing equation obtained by taking the phase average of governing equations for each phase under a thermal non-equilibrium approach is much more complicated than the original governing equations, and has many tensor terms that must be determined, thus having limitations for practical applications. In order to solve this problem while conforming to a thermal non-equilibrium approach, a semi-heuristic thermal non-equilibrium approach is introduced. Since this approach has a semi-heuristic property, the mathematical rigor degrades, but its simplicity and conciseness allows use in many practical applications. There are three main types of models following the semi-heuristic thermal non-equilibrium approach.

#### *Schumann model*

$$\begin{aligned}\frac{\partial \langle T \rangle^f}{\partial t} + \langle u \rangle^f \frac{\partial \langle T \rangle^f}{\partial x} &= \frac{h_{sf} A_0}{\varepsilon (\rho c_p)_f} \left( \langle T \rangle^s - \langle T \rangle^f \right) \\ \frac{\partial \langle T \rangle^s}{\partial t} &= - \frac{h_{sf} A_0}{(1 - \varepsilon) (\rho c_p)_s} \left( \langle T \rangle^s - \langle T \rangle^f \right)\end{aligned}\quad (3.29)$$

This is the most simple, but least accurate of all introduced models. In this model, while the energy transfer due to interphase convection is described, it has the limitation that energy transfer due to conduction is not described.

#### *Continuous-solid model*

$$\begin{aligned}\frac{\partial \langle T \rangle^f}{\partial t} + \langle u \rangle^f \frac{\partial \langle T \rangle^f}{\partial x} &= \frac{\langle k \rangle^f}{\varepsilon (\rho c_p)_f} \frac{\partial^2 \langle T \rangle^f}{\partial x^2} + \frac{h_{sf} A_0}{\varepsilon (\rho c_p)_f} \left( \langle T \rangle^s - \langle T \rangle^f \right) \\ \frac{\partial \langle T \rangle^s}{\partial t} &= \frac{\langle k \rangle^s}{(1 - \varepsilon) (\rho c_p)_s} \frac{\partial^2 \langle T \rangle^s}{\partial x^2} - \frac{h_{sf} A_0}{(1 - \varepsilon) (\rho c_p)_s} \left( \langle T \rangle^s - \langle T \rangle^f \right)\end{aligned}\quad (3.30)$$



Continuous-solid model is capable of considering both conduction and convection between phases, and high accuracy is guaranteed if the conduction and convection heat transfer coefficients can be determined appropriately. Therefore, in this study, this model will be used as the energy equation.

*Dispersion-Particle-Based model*

$$\begin{aligned}
\frac{\partial \langle T \rangle^f}{\partial t} + \langle u \rangle^f \frac{\partial \langle T \rangle^f}{\partial x} &= \frac{1}{\varepsilon} \left( \frac{\langle k \rangle}{(\rho c_p)_f} + D_{xx}^d \right) \frac{\partial^2 \langle T \rangle^f}{\partial x^2} + \frac{h_{sf} A_0}{\varepsilon (\rho c_p)_f} (T_{sf} - \langle T \rangle^f) \\
\frac{\partial T_s}{\partial t} &= \frac{\langle k \rangle^s}{(\rho c_p)_s} \frac{1}{r^2} \frac{\partial}{\partial r} \left( r^2 \frac{\partial T_s}{\partial r} \right) \\
-k_s \frac{\partial T_s}{\partial r} &= h_{sf} (T_{sf} - \langle T \rangle^f) \text{ on } A_{fs}
\end{aligned} \tag{3.31}$$

Here,

$$T_{sf} = T_s \text{ on } A_{fs}$$

$$D_{II}^d / \alpha_f = 0.5 Pe, \quad Pe = \varepsilon u_p d / \alpha_f$$

This model is the most accurate of all three models introduced, but is also the most fastidious of all three, as it still requires the determination of tensor value in order to solve this model.

Therefore, the governing equations for louvered fin with porosity assumption are summarized as below:

Continuity equation

$$\nabla \cdot \vec{u}_D = 0$$

Momentum equation

$$\nabla p = -\frac{\mu_f}{K} \vec{u}_D - \frac{C_E}{K^{1/2}} \rho |\vec{u}_D| \vec{u}_D$$

Energy equation

$$\frac{\partial \langle T \rangle^f}{\partial t} + \frac{\vec{u}_D}{\varepsilon} \frac{\partial \langle T \rangle^f}{\partial x} = \frac{\langle k \rangle^f}{\varepsilon(\rho c_p)_f} \frac{\partial^2 \langle T \rangle^f}{\partial x^2} + \frac{h_{sf} A_0}{\varepsilon(\rho c_p)_f} (\langle T \rangle^s - \langle T \rangle^f)$$

$$\frac{\partial \langle T \rangle^s}{\partial t} = \frac{\langle k \rangle^s}{(1-\varepsilon)(\rho c_p)_s} \frac{\partial^2 \langle T \rangle^s}{\partial x^2} - \frac{h_{sf} A_0}{(1-\varepsilon)(\rho c_p)_s} (\langle T \rangle^s - \langle T \rangle^f)$$

Hence, in later chapters, the intrinsic permeability, Ergun constant, and interfacial heat transfer coefficient ( $h_{sf}$ ) of louvered fin will be obtained, in order to solve the above governing equations.

### 3.5 Previous Study of Fin as Porous media

Following the 1960s, the research on porous media was actively conducted, and in particular, theory of porous media was applied to the area of mechanical engineering after 1980s and numerous researches are still in progress. J.C.Y. Koh and R. Colony [20] assumed micro-channels used for cooling of electronic devices as porous media in order to predict the temperature distribution inside micro-channels, and verified this through an experiment. In their research, Darcy equation was used as momentum equation, and uniform heat flux conditions were used as thermal boundary conditions. Moreover, a numerical analysis was used to obtain the solution. S.J. Kim and D.Kim [21] assumed micro-channels to be porous media, and used modified Darcy equation as momentum equation. For energy equation, two energy equations that conform to thermal non-equilibrium assumption in porous media were used. Uniform heat flux conditions were used as thermal boundary conditions, and obtained an analytical solution. H.I. You and C. H. Chang [22] determined the permeability and Ergun constant of pin fin, and H.I. You and C. H. Chang [23] assumed pin fin to be a porous medium, and used modified Darcy equation as momentum equation. Moreover, uniform temperature conditions were used as thermal boundary conditions. Also, Nusselt number of pin fin was predicted using CFD. D. Kim, S.J. Kim and A. Ortega [24] determined the intrinsic permeability and Ergun constant of pin fin in order to utilize a porous medium approach, used uniform heat flux conditions as thermal boundary conditions, and reported that performance and power consumption of pin fin can be predicted using CFD for not only laminar but turbulent flow regimes. D. K. Kim, J. H. Jung and S. J. Kim [25] found the optimal fin thickness for plate-fin heat sink using a porous medium approach. Summarizing the previous works, it is observed that relatively simple forms of heat exchanger

models have been used, and that thermal boundary conditions are uniform heat flux or uniform temperature conditions. However, this paper treats louvered fin, which has a highly complicated geometry, and the thermal boundary condition at the fin-tube boundary is neither uniform heat flux nor uniform temperature conditions. Therefore, if a thermodynamic porous model of louvered fin is successfully established for performance prediction in this thesis, a general methodology can be proposed from this study, that is irrespective of the geometry of heat exchanger or thermal boundary conditions.

## 4. Construction of Data Base for louvered fin

### 4.1 Design for louvered fin

The detailed design and terminology pertinent to louvered fin are shown in Figure 4.1.

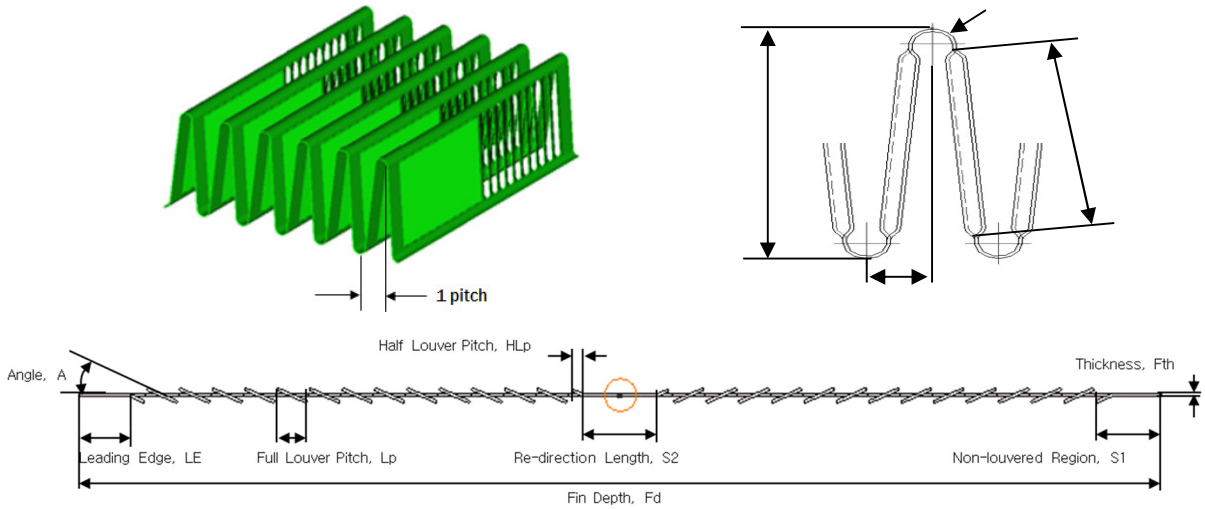


Fig. 4.1 Detail description of louvered fin parameters

While there are various parameters used in a louvered fin design as shown in Figure 4.1, louver pitch ( $L_p$ ), louver angle ( $L_a$ ), and louvered fin height ( $H$ ) are particularly important factors that have dominant effect on flow friction and heat transfer performances of louvered fin. In general, for constant effective surface area of a heat exchanger, there is an increasing trend for heat transfer performance and friction resistance as louver pitch ( $L_p$ ) and louvered fin height ( $H$ ) decrease, and louver angle ( $L_a$ ) increases. In louvered fin heat transfer, majority of heat transfer is attributed to the louver. A louvered fin enhances the heat transfer performance by suppressing the growth of thermal boundary layer through terminating the thermal boundary along the direction of flow. Moreover, louvered fins are manufactured by roll forming process, and thus

very advantageous for mass production. These are the reasons why a louvered fin was selected for compact heat exchangers for cars rather than various other heat exchanger fins. Figure 4-2 shows the louvered and un-louvered regions in a louvered fin. While un-louvered regions are unnecessary for improving the heat transfer performance and friction resistance property, un-louvered regions must be included for manufacturing processes. The loss from non-louvered regions are due to a span-wise coherent structure as in the work of Cui and Tafti [26].

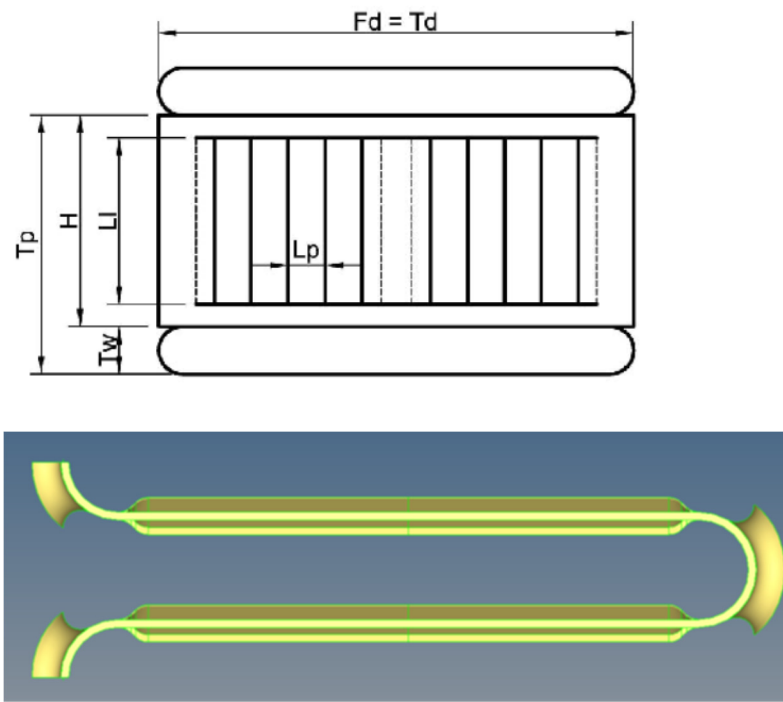


Fig. 4.2 Schematic for louvered-, Un-louvered regions

From, the numerical results of large eddy simulation (LES) by Cui & Tafti [26], it was shown that even if the Reynolds number is around 1000 with reference to louvered fin pitch ( $L_p$ ), locally, the flow is strongly turbulent, and is at unsteady state rather than steady state, due to the span-wise coherent structure generated from un-louvered region and vortex occurring at the edge of

louvered region. As such, the 3D numerical analysis of flow and heat transfer near louvered fin is a highly challenging task. However, as the louvered fin depth ( $F_d$ ) becomes relatively large (greater than 35mm), the error between numerical analysis and experimental results becomes smaller, and as the louvered fin depth becomes relatively small (less than 20mm), the error between numerical analysis and experimental results become larger. This is because if fin depth ( $F_d$ ) is larger, the momentum in stream-wise direction is much larger than the loss due to span-wise directional coherent structure generated from a un-louvered region, reducing the error between analysis and experimental results. Meanwhile, if the fin-depth ( $F_d$ ) is smaller, the loss due to a span-wise directional coherent structure generated from the un-louvered region is relatively large, causing the increase in error between analysis and experimental results. The flow around louvered fin is well depicted by the dye visualization shown in Figure 4.3. As it can be observed from Figure 4.3, there are two different types of flow near the louvered fin. Namely, these are louvered direct flow and duct direct flow. In general, duct direct flow is dominant for smaller Reynolds number, which changes to louvered direct flow as Reynolds number increases. In general, the design of louvered fin intends for louvered direct flow to be dominant. This is because the heat transfer in louvered fin occurs in louver, as aforementioned. However, as shown in Figure 4.4, in an actual louvered fin flow, louvered direct flow and duct direct flow coexist.

In the next section, in order to observe the accuracy of the numerical analysis of flow and heat transfer of louvered fin presented in this thesis, the experimental result and the numerical analysis results from previous works are compared against each other.

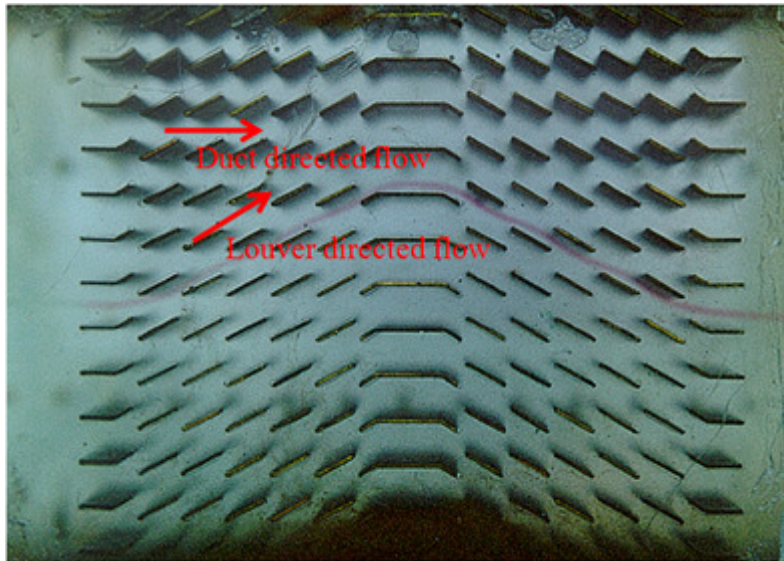


Fig. 4.3 Duct- and Louvered- directed flow around louvered fin



Fig. 4.4 Real flow around louvered fin

Above characteristics can be observed for different Reynolds numbers, through the numerical analysis of flow and heat transfer in flow near louvered fin as well. In Figure 4.5 and 4.6, the flow and temperature fields at Reynolds



number 0.1, 100, 400, and 800 are shown. As can be seen here, when Reynolds number is very low, or 0.1, duct direct flow is dominant in the flow near louvered fin, and as Reynolds number increases, the flow has a transition to louvered fin.

Figure 4.7 shows the flow and heat transfer characteristics near louvered fin for different Reynolds numbers, from the work of Archaichia & Cowell [5].

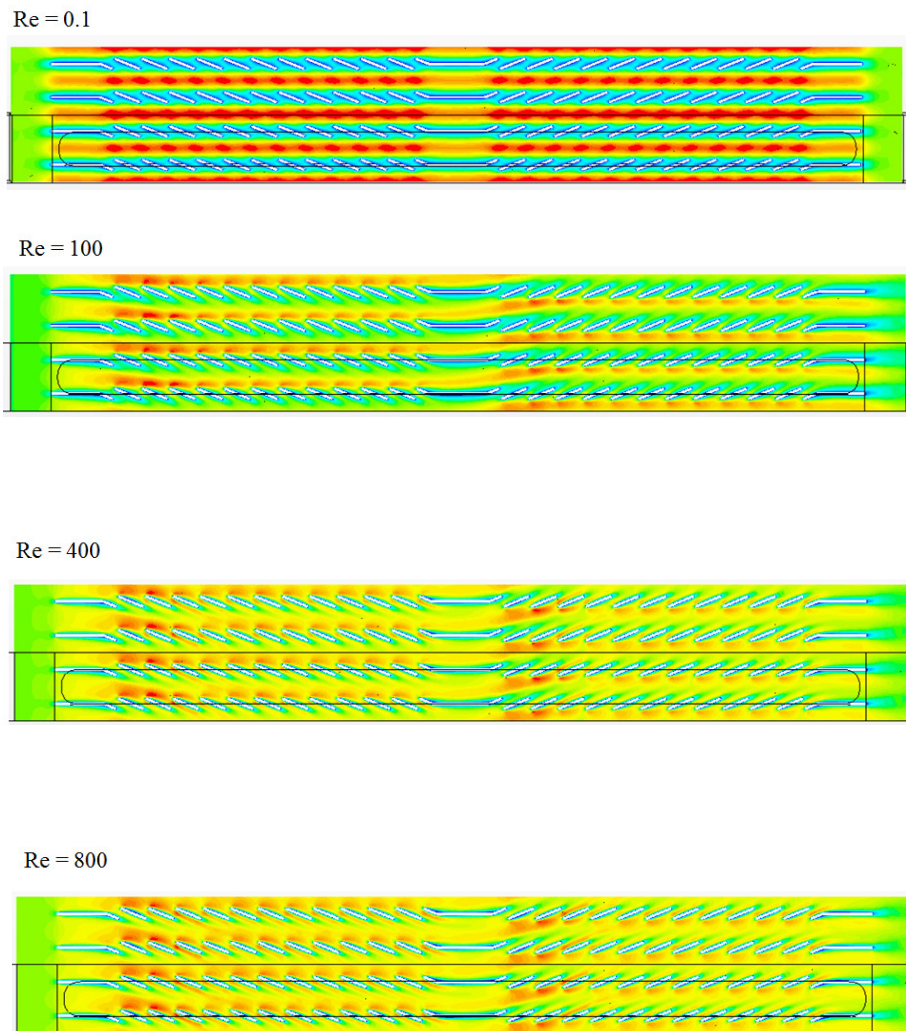
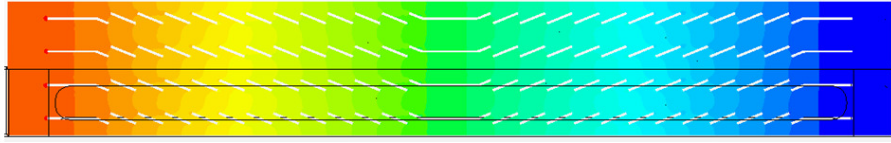
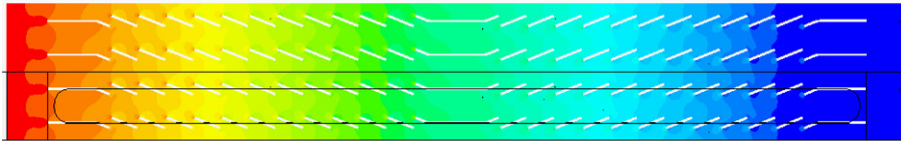


Fig. 4.5 Flow visualization for around louvered fin

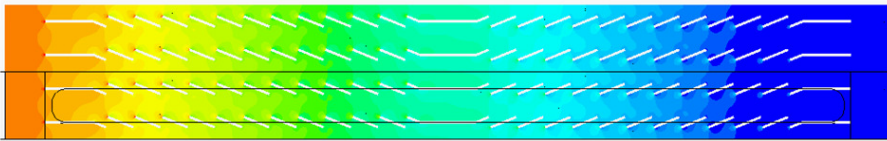
Re = 0.1



Re = 100



Re = 400



Re = 800

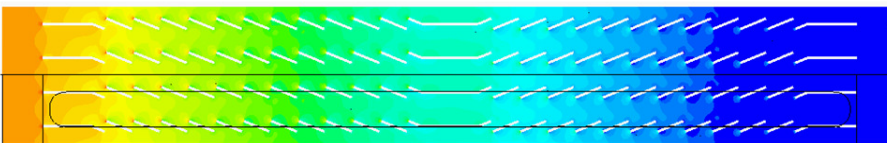


Fig. 4.6 Pressure visualization for around louvered fin

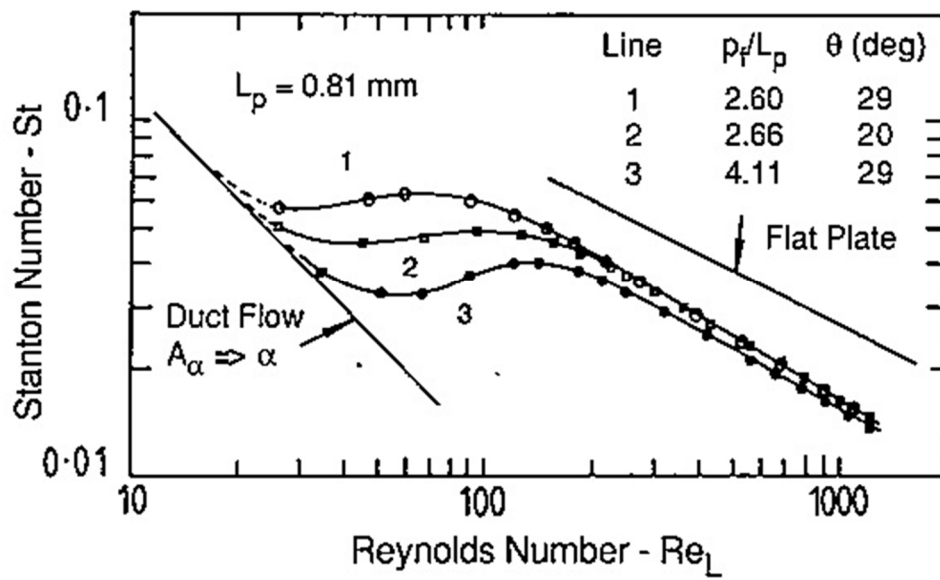


Fig. 4.7 Stanton number curves demonstrating transition from duct to flat-plate flow (Achaichia & Cowell, 1988)

## 4.2 CFD results validation for louvered fin

In order to verify the accuracy of the flow and heat transfer analysis results to be used in this study, a comparison was made to the experimental data from Achaichia and Cowell [5] and analysis results from Atkinson et al [27]. Figure 4.8 and Table 1 show the geometry of the louvered plate fin used in Achaichia and Cowell [5] and the specifications of the fin used in this study.

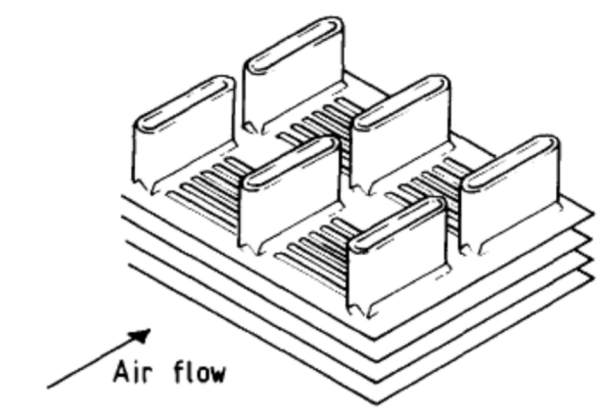


Fig. 4.8 Achaichia & Cowell's experiment model

In this study, a numerical analysis was performed for variants 1 and 3 of the test samples from Achaichia and Cowell [5]. Meanwhile, Atkinson et al [27] performed a 3D numerical analysis for flow and heat transfer based on the test data and the information on louvered fin test samples of Achaichia and Cowell [5]. The louvered plate fin in Atkinson et al [27] did not consider the un-louvered region unlike Achaichia and Cowell [5]. The model of the louvered plate fin used in the work of Atkinson et al [27] is shown in Figure 4.9.

Table 4.1 Test samples conducted by Achaichia & Cowell

| <i>Variant</i> | <i>Fin<br/>Pitch<br/>F (mm)</i> | <i>Louver<br/>Pitch<br/>L (mm)</i> | <i>Louver<br/>Angle<br/><math>\alpha</math> (deg)</i> | <i>Tube<br/>Transverse<br/>Pitch<br/>T (mm)</i> | <i>Rows of<br/>Tubes</i> | <i>Hydraulic<br/>Diameter<br/><math>d_h</math> (mm)</i> | <i>Min. free<br/>flow area<br/>frontal area<br/><math>\sigma</math></i> |
|----------------|---------------------------------|------------------------------------|---|---|--------------------------|---|---|
| 1              | 2.02                            | 1.4                                | 25.5  | 11  | 2                        | 3.33  | 0.813   |
| 2              | 3.25                            | 1.4                                | 25.5  | 11  | 2                        | 4.94  | 0.822   |
| 3              | 1.65                            | 1.4                                | 25.5  | 11  | 2                        | 2.69  | 0.808   |
| 4              | 2.09                            | 1.4                                | 21.5  | 11  | 2                        | 3.37  | 0.814   |
| 5              | 2.03                            | 1.4                                | 28.5  | 11  | 2                        | 3.30  | 0.813   |
| 6              | 2.15                            | 1.4                                | 25.5  | 11  | 1                        | 3.47  | 0.813   |
| 7              | 1.70                            | 1.4                                | 25.5  | 11  | 1                        | 2.76  | 0.807   |
| 8              | 2.11                            | 0.81                               | 29  | 11  | 2                        | 3.38  | 0.812   |
| 9              | 1.72                            | 0.81                               | 29  | 11  | 2                        | 2.81  | 0.807   |
| 10             | 3.33                            | 0.81                               | 29  | 11  | 2                        | 5.02  | 0.820   |
| 11             | 2.18                            | 1.1                                | 30  | 11  | 2                        | 3.49  | 0.813   |
| 12             | 2.16                            | 0.81                               | 20  | 11  | 2                        | 3.45  | 0.812   |
| 13             | 2.16                            | 1.1                                | 28  | 8   | 2                        | 3.14  | 0.746   |
| 14             | 2.17                            | 1.1                                | 22  | 14  | 2                        | 3.66  | 0.850   |
| 15             | 2.17                            | 1.1                                | 22  | 8   | 2                        | 3.16  | 0.747   |

$\sigma$  = ratio of minimum free-flow area to frontal area.

In this study, a numerical analysis was performed for variants 1 and 3 of the test samples from Achaichia and Cowell [5]. Meanwhile, Atkinson et al [27] performed a 3D numerical analysis for flow and heat transfer based on the test data and the information on louvered fin test samples of Achaichia and Cowell [5]. The louvered plate fin in Atkison et al [27] did not consider the unlouvered region unlike Achaichia and Cowell [5]. The model of the louvered plate fin used in the work of Atkison et al [27] is shown in Figure 4.9.

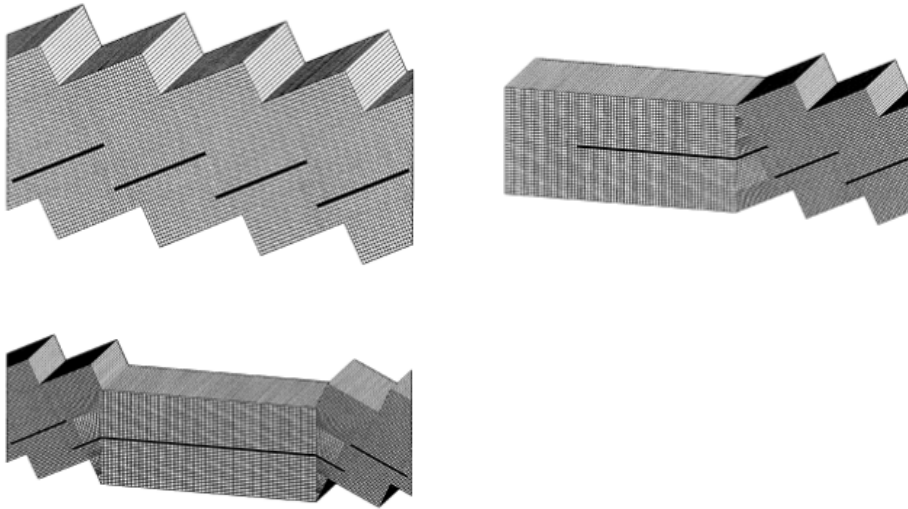
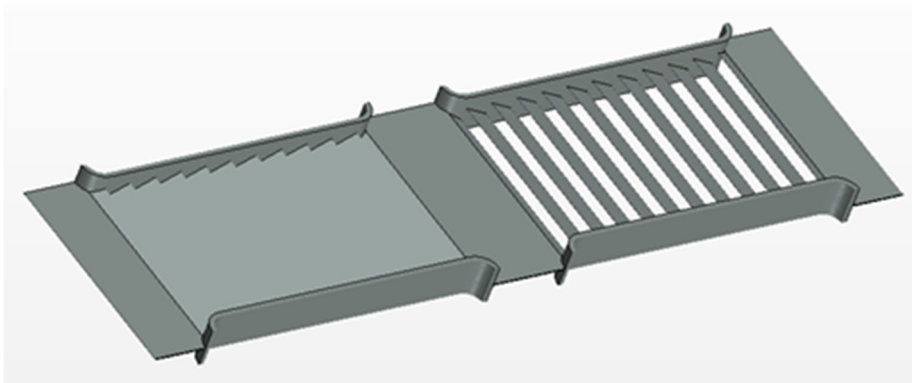
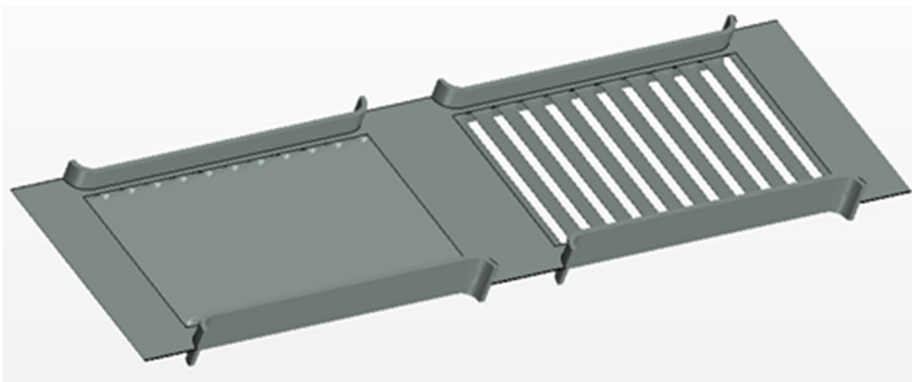


Fig. 4.9 Louvered plate fin model using Atkinson et al. study

Since Atkinson et al [27] did not consider the un-louvered region, there is no change in the geometry of louvered fin in span-wise direction, and thus this model can be considered as 2D. However, in this study, two types of models are considered for a numerical analysis of flow and heat transfer, including the one without un-louvered region similar to Atkinson et al [27], and the one that considers the louvered region similar to Achaichia and Cowell [5], in order to consider the un-louvered region as well. Figure 4.10 shows the models of louvered plat fin used in this study. Moreover, in Figure 4.11, the boundary conditions used in the numerical analysis of louvered plate fin in this thesis are specified.



(a)



(b)

Fig. 4.10 (a) Louvered plate fin without un-louvered region, (b) Louvered plate fin with louvered region

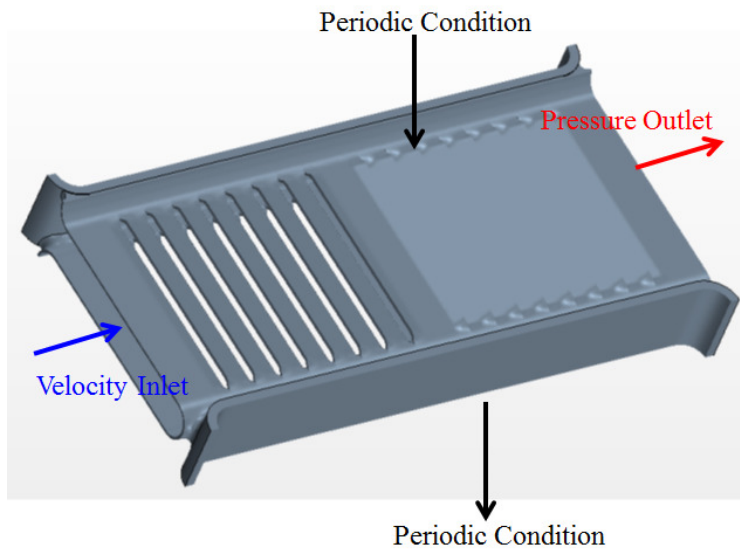


Fig. 4.11 Boundary conditions for louvered (plate) fin

In this study, a numerical analysis of flow and heat transfer was performed using the boundary conditions specified in the work of Achaichia and Cowell [5], and the result was compared to the results from Achaichia and Cowell [5] and Atkinson et al [27]. Figure 4.12 shows the comparison of friction coefficient, and Figure 4.13 shows the comparison of Stanton number. As shown in Figure 4.12, there is a good agreement between the test data from Achaichia and Cowell [5], CFD data from Atkinson et al [27], and the CFD data from this thesis. However, in terms of Stanton number in Figure 4.13, which represents the heat transfer performance, the simulation model for Achaichia and Cowell [5] is closer to the test data of Achaichia and Cowell [5] than the numerical results from Atkinson et al [27]. As such, it is seen that there is no shortcoming in using a numerical analysis in this study as a tool for obtaining the flow and heat transfer characteristics of louvered fin. Therefore, in the next section, we obtain through a numerical analysis the data for Reynolds number less than 100 or greater than 1000, for which the empirical equation for a louvered fin from Kang and Jun [1] is not guaranteed to hold.



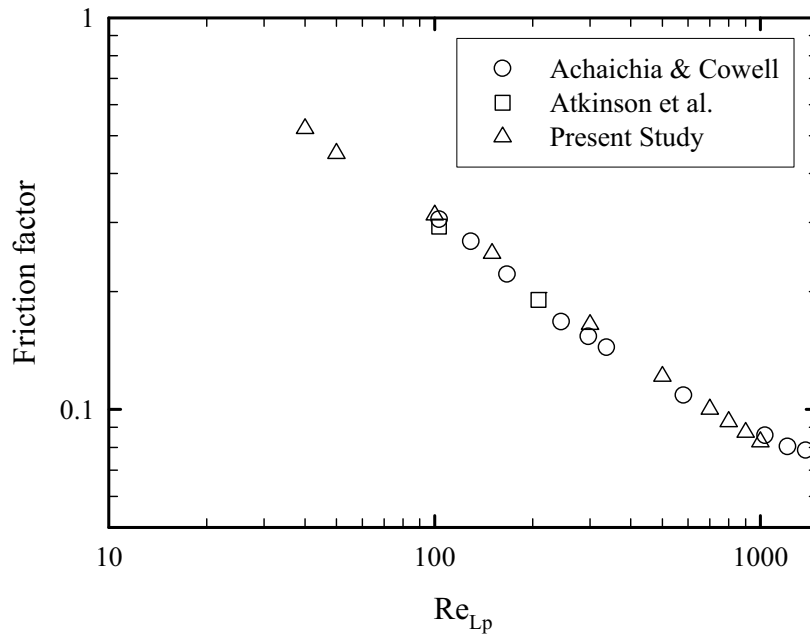


Fig. 4.12  $f$  factor according to Investors

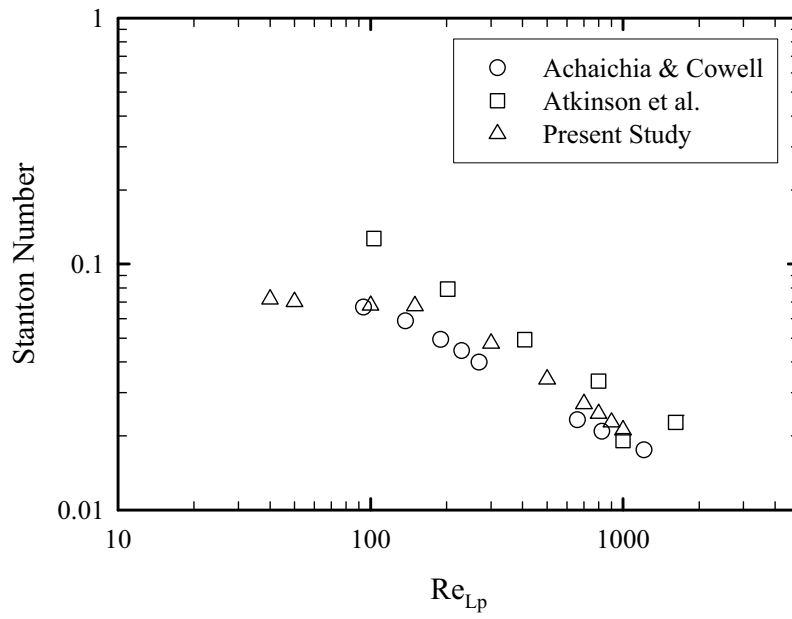


Fig. 4.13  $St$  number according to Investors

In order to use the CFD data for  $Re_{Lp} > 1,000$  in the database, the actual CFD results were compared to the following correlation proposed by Achiachia and Cowell [5]. Below is the correlation proposed by Achaichia and Cowell [5].

Achaichia and Cowell's correlation ( $150 < Re_{Lp} < 3,000$ )

$$f_A = 596 Re_{Lp}^{(0.318 \log Re_{Lp} - 2.25)}$$

$$f = 0.895 f_A^{1.07} F^{-0.22} L^{0.25} T^{0.26} H^{0.33}$$

$$H = L \sin \alpha$$

where  $F$  : fin pitch,  $L$  : louver pitch,  $T$  : tube transverse pitch,  $\alpha$  : louver angle

As a result, the graph as in Figure 4.14 was obtained for  $Re_{Lp} > 1,000$  with increasing Reynolds number.

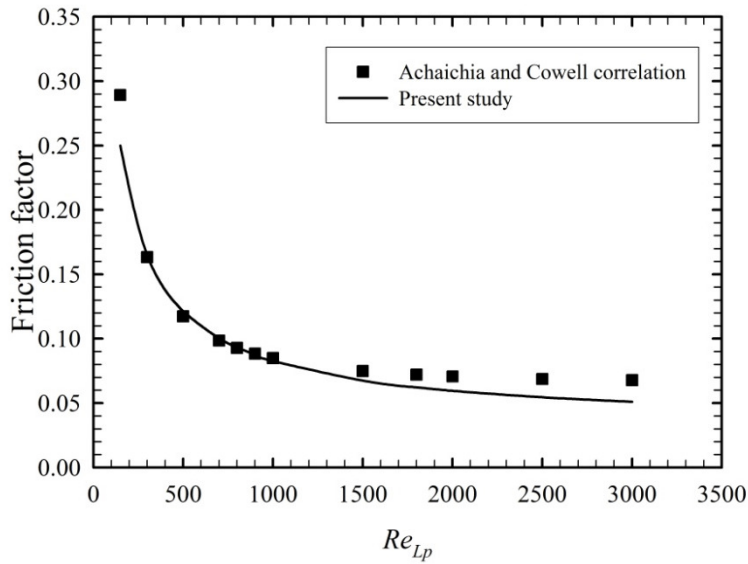


Fig. 4.14 Comparison of Experimental and CFD results for louvered plate fin  
Therefore, it is seen that the following analysis error is included, for different Reynolds number.

- $Re_{Lp} < 1,000$ : within 2% error
- $1,000 < Re_{Lp} < 2,500$ : within 10% error
- $Re_{Lp} > 3,000$ : within 20% error

Therefore, the CFD results for  $Re_{Lp} > 1,000$  can be taken as the values for the database.

### 4.3 Construction of Data Base for louvered fin

In order to perform the flow and heat transfer analysis for heat exchanger assembly with a louvered fin, porous media approach for a louvered fin is used in this paper. In order to apply the porous media approach, the momentum equation for the louvered fin region, assumed to be a porous medium, will be chosen to be modified Darcy equation, and for energy equation, a local thermal non-equilibrium approach is taken, in order to solve the equation for the louvered fin and the air passing through a louvered fin. The governing equation in a porous medium used in this thesis is as below:

$$\nabla \cdot \vec{u}_D = 0 \quad (4.1)$$

$$\nabla p = -\frac{\mu_f}{K} \vec{u}_D - \frac{C_E}{\sqrt{K}} \rho \vec{u}_D^2 \quad (4.2)$$

$$(1 - \varepsilon) \rho_s C_s \frac{\partial T_s}{\partial t} = k_{se} \frac{\partial^2 T_s}{\partial x^2} + h_{sf} a_{sf} (T_f - T_s) \quad (4.3)$$

$$\varepsilon \rho_f C_f \left[ \frac{\partial T_f}{\partial t} + \langle u \rangle^f \frac{\partial T_f}{\partial x} \right] = k_{fe} \frac{\partial^2 T_f}{\partial x^2} + h_{sf} a_{sf} (T_s - T_f) \quad (4.4)$$

Where,

$k_{fe} = \varepsilon k_f$ : Effective thermal conductivity of the fluid

$k_{se} = (1 - \varepsilon) k_s$ : Effective thermal conductivity of the solid

$a_{sf}$ : Wetted area per volume

$h_{sf}$ : Interstitial heat transfer coefficient

$u_p = \langle u \rangle^f$ : Average pore velocity

$\varepsilon$ : Porosity

$K$ : Permeability

$C_E$ : Ergun constant

Hence, in order to solve the governing equation in a porous medium, the permeability ( $K$ ), Ergun constant ( $C_E$ ), and interstitial heat transfer coefficient ( $h_{sf}$ ) must be determined first.

In order to determine the momentum equation inside porous media, the permeability ( $K$ ) and Ergun constant ( $C_E$ ) must be predetermined. Modified Darcy equation consists of viscous term and inertial term inside a porous medium, and considers the characteristics of a porous medium. If the Reynolds number inside porous medium is greater than 1, the effect of inertial force must be considered. Therefore, in many applications, Reynolds number is generally greater than 1. In particular, for car heat exchangers, the Reynolds number is between 100 and 1000, and thus the viscous force is insignificant compared to inertial force. Hence, the pressure difference from fluid passing through louvered fin has the exponent from 1 to 2 in previous works on a louvered fin (Table 2).

Table 4.2 Relation pressure drop passed in louvered fin and velocity for various friction models

|  |                              |
|--|------------------------------|
| $70 < \text{Re}_{D_h} < 900$<br>$\Delta p \sim u^{1.389}$    | Davenport (1983)             |
| $1000 < \text{Re}_{D_h} < 4000$<br>$\Delta p \sim u^{2.564}$ |                              |
| $\text{Re}_{D_h} < 150$<br>$\Delta p \sim u^{0.855}$         | Achaichia and Cowell (1988)  |
| $150 < \text{Re}_{D_h} < 3000$<br>$\Delta p \sim u^{0.935}$  |                              |
| $100 < \text{Re}_{D_h} < 1000$<br>$\Delta p \sim u^{1.852}$  | Sunden and Svantesson (1992) |
| $130 < \text{Re}_{D_h} < 800$<br>$\Delta p \sim u^{1.608}$   | Kang and Jun (2011)          |

While this can be the best regression curve for Reynolds number between 100 and 1000, when Reynolds number is less than 100 or greater than 1000, the error between tests with previous models increases. Therefore, in order to determine the permeability ( $K$ ) and Ergun constant in modified Darcy equation, the pressure drop and heat transfer amount must be obtained for Reynolds number from less than 1 to greater than 1000. Meanwhile, Kang and Jun [1] proposed the friction and heat transfer models as in Equations (4.5) and (4.6) through an experiment for Reynolds number from 200 to 800, using the same model as that used in this study.

$$130 < \text{Re}_{L_p} < 800$$

$$f = 4.81 \text{Re}_{L_p}^{-0.622} (\cos \theta)^{-1.94} \left( \frac{L_p}{F_p} \right)^{0.233} \quad (4.5)$$

$$j = 4181 \text{Re}_{L_p}^{-0.698} \left( \frac{L_p}{F_p \cos \theta} \right)^{0.364} \quad (4.6)$$

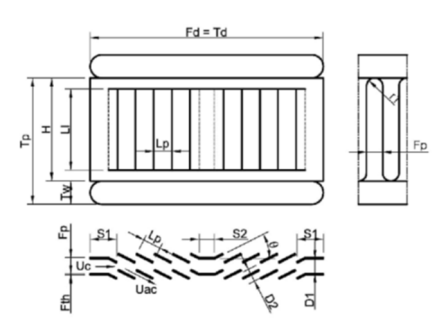
Therefore, when a louvered fin is assumed to be a porous medium and modified Darcy equation is selected as the momentum equation, the permeability ( $K$ ) and Ergun constant ( $C_E$ ) of the louvered fin must be determined. Since the effects of viscous force from pressure gradient and inertial force must be considered separately, the friction coefficient must be obtained from very low Reynolds number ( $\sim 1$ ) to very large Reynolds number ( $\sim 30,000$ ).

In this study, the friction coefficient is obtained from the empirical equation of Kang and Jun [1] for Reynolds number from 100 to 1000, and for Reynolds number less than 100 or greater than 1000, the friction coefficient data is obtained using CFD. The test model used in the work of Kang and Jun [1] is a 3-times magnified model of louvered fin, and detailed verification is referred

to references [28, 29]. Table 4.3 summarizes the geometrical characteristics of the model used in Kang and Jun [1] and in this study.

Table 4.3 Detail geometries information of louvered fin for present study

| Name                          | Symbol      | Lp9<br>A22 | Lp9<br>A27 | Lp9<br>A32 | Lp9<br>A37 | Lp11<br>A22 | Lp11<br>A27 | Lp11<br>A32 | Lp11<br>A37 | Lp13<br>A22 | Lp13<br>A27 | Lp13<br>A32 | Lp13<br>A37 | Lp14<br>A27 | Lp10<br>A22 |
|-------------------------------|-------------|------------|------------|------------|------------|-------------|-------------|-------------|-------------|-------------|-------------|-------------|-------------|-------------|-------------|
| Louver pitch                  | $L_p$       | 2.7        | 2.7        | 2.7        | 2.7        | 3.3         | 3.3         | 3.3         | 3.3         | 3.9         | 3.9         | 3.9         | 3.9         | 4.2         | 3.0         |
| Louver angle                  | $\theta$    | 22         | 27         | 32         | 37         | 22          | 27          | 32          | 37          | 22          | 27          | 32          | 37          | 27          | 22          |
| Non-louvered region           | $S_1$       | 5.25       | 5.25       | 5.25       | 5.25       | 4.05        | 4.05        | 4.05        | 4.05        | 4.05        | 4.05        | 4.05        | 4.05        | 6.30        | 5.39        |
| Re-direction length           | $S_2$       | 2.33       | 2.33       | 2.33       | 2.33       | 3.00        | 3.00        | 3.00        | 3.00        | 3.00        | 3.00        | 3.00        | 3.00        | 3.60        | 6.15        |
| Depth of fin                  | $F_d$       | 54.0       | 54.0       | 54.0       | 54.0       | 54.0        | 54.0        | 54.0        | 54.0        | 54.0        | 54.0        | 54.0        | 54.0        | 54.0        | 55.5        |
| Fin pitch                     | $F_p$       | 3.64       | 3.64       | 3.64       | 3.64       | 3.64        | 3.64        | 3.64        | 3.64        | 3.64        | 3.64        | 3.64        | 3.64        | 3.64        | 3.64        |
| Fin thickness                 | $F_{th}$    | 0.27       | 0.27       | 0.27       | 0.27       | 0.27        | 0.27        | 0.27        | 0.27        | 0.27        | 0.27        | 0.27        | 0.27        | 0.27        | 0.27        |
| Fin height                    | $H$         | 23.6       | 23.6       | 23.6       | 23.6       | 23.6        | 23.6        | 23.6        | 23.6        | 23.6        | 23.6        | 23.6        | 23.6        | 23.6        | 27.2        |
| Louver length                 | $L_l$       | 18.6       | 18.6       | 18.6       | 18.6       | 18.6        | 18.6        | 18.6        | 18.6        | 18.6        | 18.6        | 18.6        | 18.6        | 18.6        | 22.2        |
| Tube depth                    | $T_d$       | 54.0       | 54.0       | 54.0       | 54.0       | 54.0        | 54.0        | 54.0        | 54.0        | 54.0        | 54.0        | 54.0        | 54.0        | 54.0        | 55.5        |
| Tube pitch                    | $T_p$       | 29.2       | 29.2       | 29.2       | 29.2       | 29.2        | 29.2        | 29.2        | 29.2        | 29.2        | 29.2        | 29.2        | 29.2        | 29.2        | 32.8        |
| Tube width                    | $T_w$       | 5.6        | 5.6        | 5.6        | 5.6        | 5.6         | 5.6         | 5.6         | 5.6         | 5.6         | 5.6         | 5.6         | 5.6         | 5.6         | 5.6         |
| Average $L_p^2$               | $\bar{L}_p$ | 3.00       | 3.00       | 3.00       | 3.00       | 3.52        | 3.52        | 3.52        | 3.52        | 4.08        | 4.08        | 4.08        | 4.08        | 4.73        | 3.38        |
| Number of louver <sup>3</sup> | -           | 17         | 17         | 17         | 17         | 15          | 15          | 15          | 15          | 13          | 13          | 13          | 13          | 11          | 15          |
| Number of fin <sup>4</sup>    | -           | 35         | 35         | 35         | 35         | 35          | 35          | 35          | 35          | 35          | 35          | 35          | 35          | 35          | 35          |
| HEX width <sup>5</sup>        | -           | 118.8      | 118.8      | 118.8      | 118.8      | 118.8       | 118.8       | 118.8       | 118.8       | 118.8       | 118.8       | 118.8       | 118.8       | 118.8       | 132.8       |
| Fin material                  | -           | Al         | Al         | Al         | Al         | Al          | Al          | Al          | Al          | Al          | Al          | Al          | Al          | Al          | Al          |



By organizing the data from the empirical equation of Kang and Jun [1] and CFD for Reynolds number less than 100 or greater than 1000, a database is established for friction coefficients of 14 different types of louvered fin for different Reynolds number as shown in Figure 4.13.

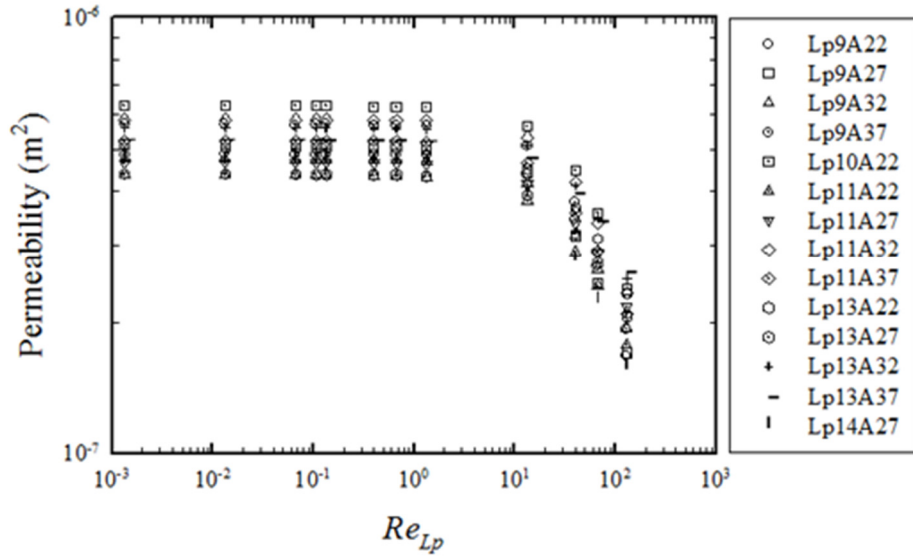


Fig. 4.13 Data-Base for louvered fin's friction factor combined by Experiment correlation and present CFD



## 5. Statistical Treatment

### 5.1 Non-linear regression

The aim of this study is to propose empirical equations for intrinsic permeability ( $K$ ) and Ergun constant ( $C_E$ ) in the momentum equation for a porous medium in terms of parameters for a louvered fin by assuming a louvered fin as a porous medium. In order to establish empirical equations for permeability ( $K$ ) and Ergun constant ( $C_E$ ), not only the empirical equation of Kang and Jun [1] was considered, but also viscous and inertial forces, for which a database was established in Chapter 3 for Reynolds number less than 100 and greater than 1000 that was not considered in Kang and Jun [1]. In this chapter, a new empirical equation that can consider both viscous and inertial forces is proposed, through a regression analysis on the established database. Figure 4.13 shows the distribution of friction coefficient for 14 louvered fin models, which was obtained by combining an empirical equation and the CFD results from this study. A peculiar aspect of this graph is that friction coefficient decreases linearly until Reynolds number of 1000, but has a constant value irrespective of Reynolds number after the Reynolds number of 1000.

Such pattern in friction coefficient distribution is very similar to the distribution of the friction coefficient obtained from a sphere with same diameter. Examining Figure 5.1, it is seen that the friction coefficient is divided into three main regions depending on the Reynolds number. When Reynolds number is less than 1, the friction coefficient is completely linear. When Reynolds number is greater than 1000, the friction coefficient is constant irrespective of Reynolds number. Moreover, when Reynolds number is between 1 and 1000, the friction coefficient decreases nonlinearly because

of the inertial force effect. Here, the friction coefficient models for each region can be proposed in three different types as below:

$$\frac{\Delta p}{L} = \mu \frac{150(1-\varepsilon)^2}{\varepsilon^2 d^2} u_D \quad \text{Blake-Kozeny Equation} \quad (5.1)$$

$$\frac{\Delta p}{L} = \mu \frac{150(1-\varepsilon)^2}{\varepsilon^2 d^2} u_D + \rho \frac{1.75}{d} \frac{1-\varepsilon}{\varepsilon^3} u_D^2 \quad \text{Ergun Equation} \quad (5.2)$$

$$\frac{\Delta p}{L} = \rho \frac{1.75}{d} \frac{1-\varepsilon}{\varepsilon^3} u_D^2 \quad \text{Burke-Plummer Equation} \quad (5.3)$$

Blake-Kozeny equation holds for Reynolds number less than 1, and has the property that pressure gradient is proportional to the Darcy velocity ( $u_D$ ). Blake-Plummer equation shows that pressure gradient is proportional to the square of the Darcy velocity ( $u_D^2$ ). Moreover, in Ergun equation, it is seen that the viscous and inertial forces must be considered together, when Reynolds number is between 1 and 1000. Since it is seen that the friction coefficient distribution for louvered fin also consists of three regions, it can be deduced that the porosity assumption for louvered fin is appropriate.

Friction coefficient can be assumed as Equation (5.4), in order to propose a new empirical equation for friction coefficient of louvered fin from Figure 4.13, and in order to separate the proposed empirical equation into viscous and inertial forces.

$$f = \frac{C_1}{\text{Re}_{L_p}} + C_2 \quad (5.4)$$

Where,  $C_1$  and  $C_2$  are functions of louvered fin parameters.

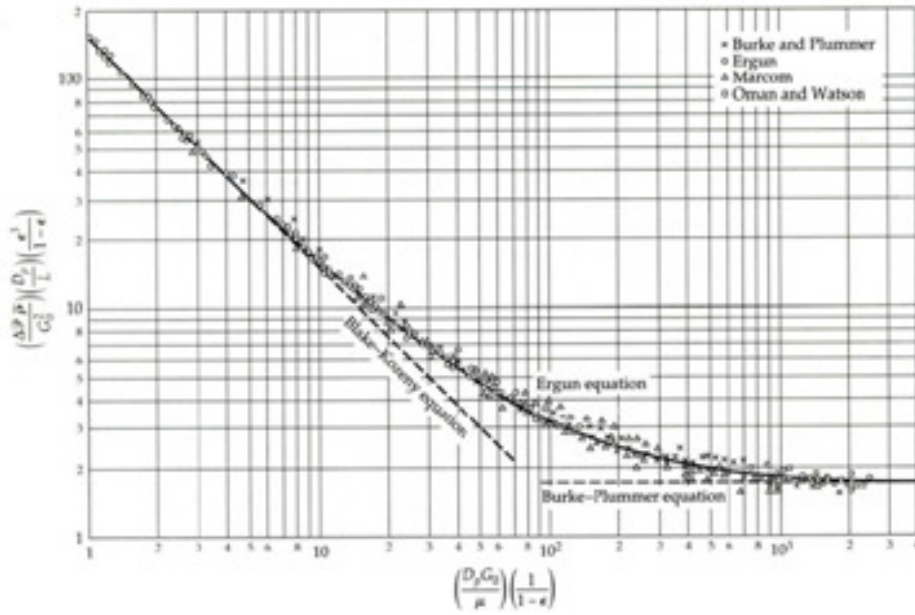


Fig. 5.1 Classical correlations of friction factor for spheres immersed by bathe

In obtaining the empirical equation through a regression analysis based on Equation (5.4), the empirical equation cannot be obtained through multi-linear regression since the equation is nonlinear. Hence,  $C_1$  and  $C_2$  are obtained from a nonlinear regression analysis from each of the 14 models of louvered fin, and the empirical equation (5.4) is obtained by performing a multi-linear regression analysis on  $C_1$  and  $C_2$ .

In order to obtain  $C_1$  and  $C_2$  for the louvered fin model using a nonlinear regression analysis, the friction coefficient is assumed as a function with variables as shown in the following [30]:

$$f_i = g(u_{p_i}; L_p, F_p, \theta) + e_i \quad (5.5)$$

Where,  $i$  corresponds to a single arbitrary Reynolds number for each louvered fin model. Moreover, for each louvered fin model, Reynolds number values

from 29 points were chosen.  $u_{pi}$  is the pore velocity, and has the following relationship with Darcy velocity ( $u_D$ ):

$$u_p = \varepsilon u_D \quad (5.6)$$

Moreover,  $L_p$ ,  $F_p$ ,  $\theta$  and  $\varepsilon$  are louver pitch, fin pitch, louver angle, and porosity respectively, and  $e_i$  is the random error. Expanding the Taylor series of Equation (5.5) to the first order for  $L_p$ ,  $F_p$ ,  $\theta$ , Equation (5.7) is obtained:

$$y_i - f_i(u_{p_i}) = \frac{\partial f_i(u_{p_i})}{\partial L_p} \Delta L_p + \frac{\partial f_i(u_{p_i})}{\partial F_p} \Delta F_p + \frac{\partial f_i(u_{p_i})}{\partial \theta} \Delta \theta + e_i \quad (5.7)$$

Where  $y_i$  is the true value obtained from the database.

By applying Equation (5.7) to  $n$  data points, the matrix form in Equation (5.8) is obtained.

$$[D] = [Z][\Delta A] + [E] \quad (5.8)$$

Here, matrices  $[D]$ ,  $[Z]$ ,  $[\Delta A]$ ,  $[E]$  are as follows:

$$[D] = \begin{bmatrix} y_1 - f_1(u_{p_1}) \\ y_2 - f_2(u_{p_2}) \\ \vdots \\ y_n - f_n(u_{p_n}) \end{bmatrix} \quad [Z] = \begin{bmatrix} \frac{\partial f_1(u_{p_1})}{\partial L_p} & \frac{\partial f_1(u_{p_1})}{\partial F_p} & \frac{\partial f_1(u_{p_1})}{\partial \theta} \\ \frac{\partial f_2(u_{p_1})}{\partial L_p} & \frac{\partial f_2(u_{p_1})}{\partial F_p} & \frac{\partial f_2(u_{p_1})}{\partial \theta} \\ \vdots & \vdots & \vdots \\ \frac{\partial f_n(u_{p_1})}{\partial L_p} & \frac{\partial f_n(u_{p_1})}{\partial F_p} & \frac{\partial f_n(u_{p_1})}{\partial \theta} \end{bmatrix}$$

$$[\Delta A] = \begin{bmatrix} \Delta L_p \\ \Delta F_p \\ \Delta \theta \end{bmatrix} \quad [E] = \begin{bmatrix} e_1 \\ e_2 \\ \cdot \\ \cdot \\ e_n \end{bmatrix}$$

Moreover, let us define the residual function  $Sr$  as follows:

$$Sr = \sum_{i=1}^n \left( D_i - \sum_{j=0}^m \Delta A_j Z_{ji} \right)^2$$

Using least squares method, partial derivatives with respect to each louver fin parameter is taken.

$$\frac{\partial Sr}{\partial L_p} = 0, \quad \frac{\partial Sr}{\partial F_p} = 0, \quad \frac{\partial Sr}{\partial \theta} = 0$$

Using a recursive algorithm, the optimal  $C_1$  and  $C_2$  for each of the 14 louvered fin models can be obtained as  $\Delta A$  approaches 0. Table 5.1 shows the values of  $C_1$  and  $C_2$  for 14 louvered fin models obtained from a nonlinear regression analysis.

Table 5.1  $C_1$  and  $C_2$  values

| Model   | $C_1$    | $C_2$   |
|---------|----------|---------|
| Lp9A22  | 17.87247 | 0.05430 |
| Lp9A27  | 22.58648 | 0.06200 |
| Lp9A32  | 29.88127 | 0.07140 |
| Lp9A37  | 34.30446 | 0.08270 |
| Lp11A22 | 20.51004 | 0.06040 |
| Lp11A27 | 24.70168 | 0.06650 |
| Lp11A32 | 32.48772 | 0.08200 |
| Lp11A37 | 36.02504 | 0.09240 |
| Lp13A22 | 24.26002 | 0.06340 |
| Lp13A27 | 27.11923 | 0.06830 |
| Lp13A32 | 33.23943 | 0.08170 |
| Lp13A37 | 38.23295 | 0.10430 |
| Lp14A27 | 29.95682 | 0.07750 |
| Lp10A22 | 20.39249 | 0.05930 |

## 5.2 Multi-linear regression

### 5.2.1 friction factor ( $f$ ) correlation

Through a nonlinear regression analysis, optimal  $C1$  and  $C2$  were obtained from each of the 14 louvered fin models, and from now on  $C1$  and  $C2$  will be turned into functions of louvered fin parameters using a multi-linear regression analysis. In order to perform a multi-linear regression analysis,  $C1$  and  $C2$  are assumed to be in the form of Equations (5.9) or (5.10).

$$C_j = \ln \left[ e^{b_{0j}} (\cos \theta)^{b_{1j}} \left( \frac{L_p}{F_p} \right)^{b_{2j}} \right] \quad (j=1,2) \quad (5.9)$$

Or

$$\begin{aligned} C_1 &= b_{01} + b_{11} \ln(\cos \theta) + b_{21} \ln \left( \frac{L_p}{F_p} \right) \\ C_2 &= b_{02} + b_{12} \ln(\cos \theta) + b_{22} \ln \left( \frac{L_p}{F_p} \right) \end{aligned} \quad (5.10)$$

Where,

Assuming that  $x_{1i} \equiv \ln(\cos \theta_i)$ ,  $x_{2i} \equiv \ln \left( \frac{L_{p,i}}{F_{p,i}} \right)$  and using least squares method, below matrix is obtained:

$$\begin{bmatrix} n & \sum x_{1i} & \sum x_{2i} \\ \sum x_{1i} & \sum x_{1i}^2 & \sum x_{1i} x_{2i} \\ \sum x_{2i} & \sum x_{1i} x_{2i} & \sum x_{2i}^2 \end{bmatrix} \begin{Bmatrix} b_0 \\ b_1 \\ b_2 \end{Bmatrix} = \begin{Bmatrix} \sum y_i \\ \sum x_{1i} y_i \\ \sum x_{2i} y_i \end{Bmatrix} \quad (5.11)$$

Solving the above matrix, below empirical equations are obtained for  $C_1$  and  $C_2$ :

$$\begin{aligned} C_1 &= 14.8 + 13.3 \ln(L_p / F_p) - 104 \ln(\cos \theta) \\ C_2 &= 0.0455 + 0.0327 \ln(L_p / F_p) - 0.224 \ln(\cos \theta) \end{aligned} \quad (5.12)$$

Therefore, new empirical equation of friction coefficient for a louvered fin obtained by assuming a louvered fin as a porous medium is as below:

$$f = \frac{14.8 + 13.3 \ln(L_p / F_p) - 104 \ln(\cos \theta)}{Re_{L_p}} + 0.0455 + 0.0327 \ln(L_p / F_p) - 0.224 \ln(\cos \theta) \quad (5.13)$$

Figure 5.2 shows the newly proposed empirical equation for a louvered fin with respect to Reynolds number and louvered fin models.

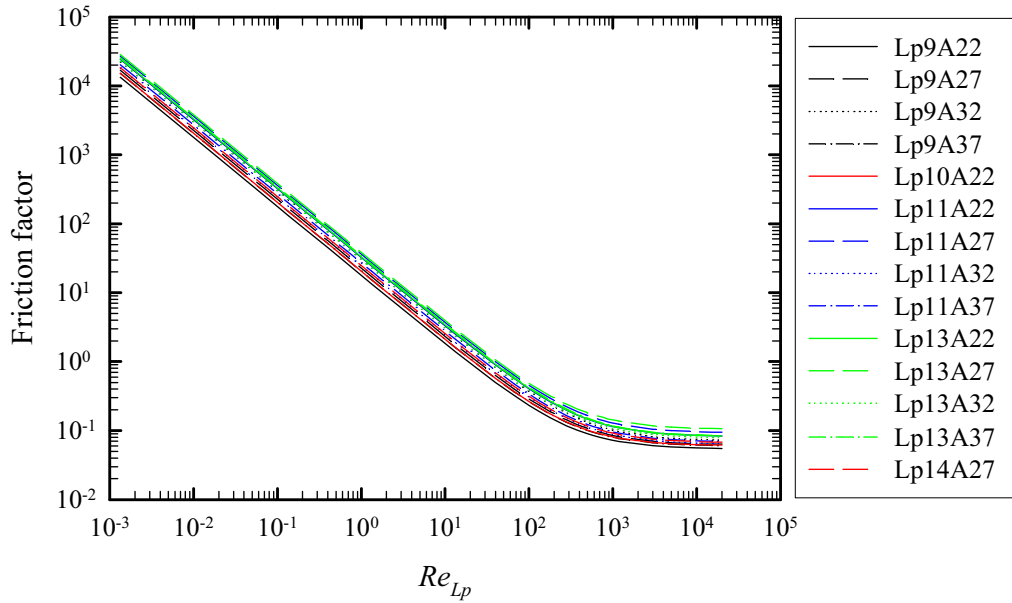


Figure 5.2 Friction factor distribution followed by new correlation equation about louvered fin



### 5.2.2 Heat transfer coefficient (Colburn $j$ factor)

This study took a thermal non-equilibrium approach for energy equation in porous media, and hence has separate energy equations for fluid and solid regarding energy inside porous medium. In a porous medium, the governing equations for each phase are as follow:

Energy equation for fluid phase

$$\frac{\partial \langle T \rangle^f}{\partial t} + \frac{\bar{u}_D}{\varepsilon} \frac{\partial \langle T \rangle^f}{\partial x} = \frac{\langle k \rangle^f}{\varepsilon(\rho c_p)_f} \frac{\partial^2 \langle T \rangle^f}{\partial x^2} + \frac{h_{sf} A_0}{\varepsilon(\rho c_p)_f} (\langle T \rangle^s - \langle T \rangle^f) \quad (5.14a)$$

Energy equation for solid phase

$$\frac{\partial \langle T \rangle^s}{\partial t} = \frac{\langle k \rangle^s}{(1-\varepsilon)(\rho c_p)_s} \frac{\partial^2 \langle T \rangle^s}{\partial x^2} - \frac{h_{sf} A_0}{(1-\varepsilon)(\rho c_p)_s} (\langle T \rangle^s - \langle T \rangle^f) \quad (5.14b)$$

Therefore, in order to solve the energy equation for louvered fin with porosity assumption, the interfacial heat transfer coefficient ( $h_{sf}$ ) must be determined. Hence, in this study, the heat transfer model of Kang and Jun [1] was used to determine the interfacial heat transfer coefficient.

The heat transfer model of Kang and Jun[1] is as follows:

$$j = 1.81 \text{Re}_{Lpa}^{-0.698} \left( \frac{L_p}{F_p \cos \theta} \right)^{0.364} \quad (5.15)$$

Moreover, the distribution of heat transfer coefficient with different Reynolds number and louvered fin model obtained from the 3D numerical analysis in this study is as follows. In Figure 5.3, it is seen that the data is in good agreement with the empirical equation of Kang and Jun [1] for Reynolds

number between 100 and 1000.

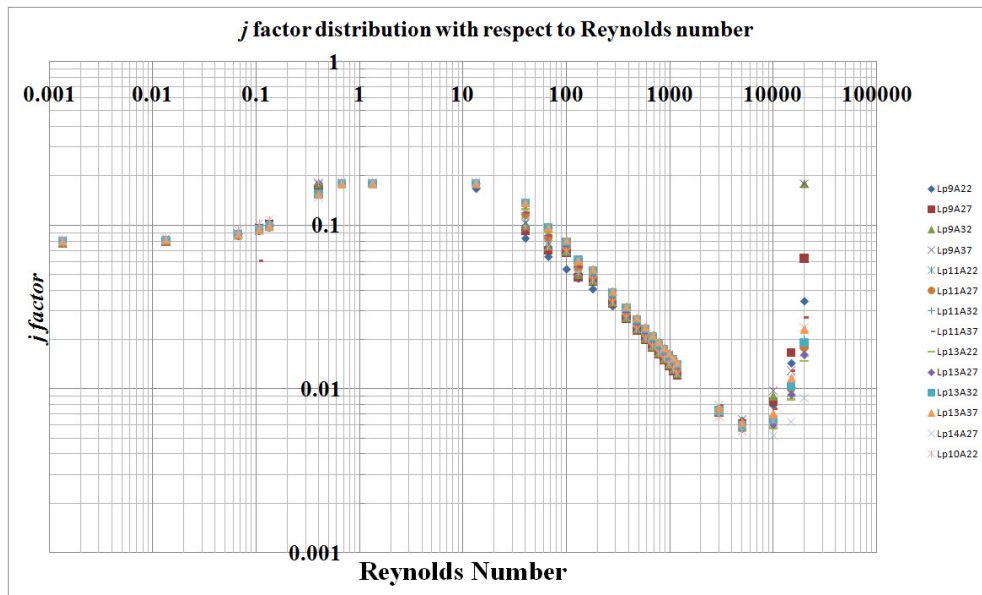
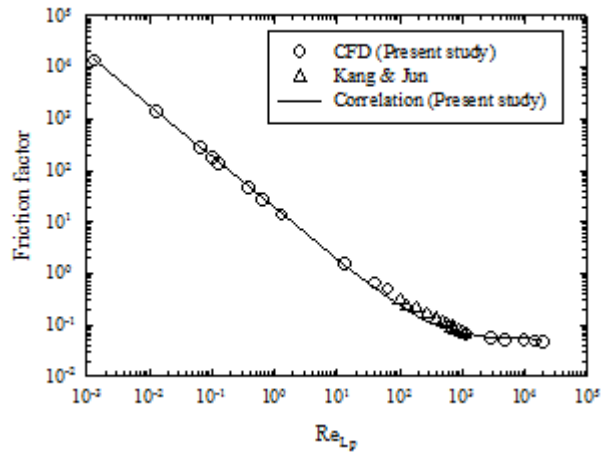


Figure 5.3 Colburn  $j$  factor distribution followed by new correlation equation about louvered fin

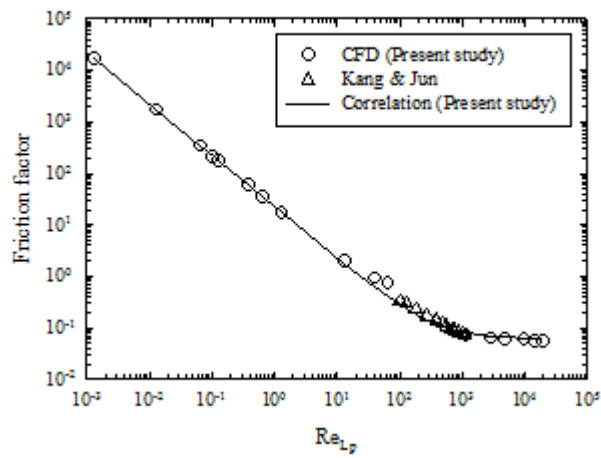
### 5.3 Verification of present correlations

#### 5.3.1 Comparison of present correlation and Data-Base

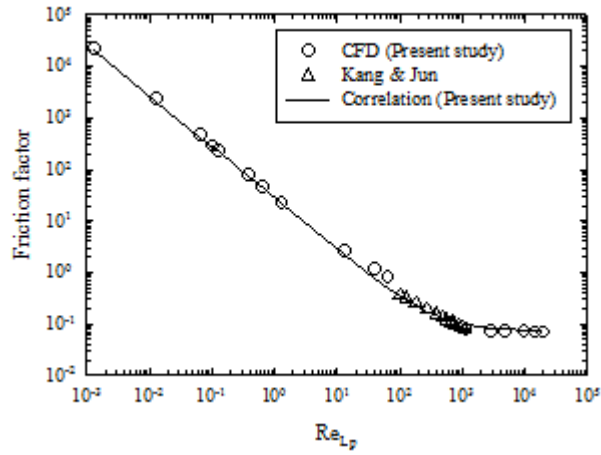
In order to verify the empirical equation for friction coefficient of louvered fin newly proposed in this study, the empirical equation was firstly compared to the database regarding louvered fin. The data used for comparison pertains to 4 types of louvered fin models (Lp9A22, Lp9A27, Lp9A32, Lp9A37).



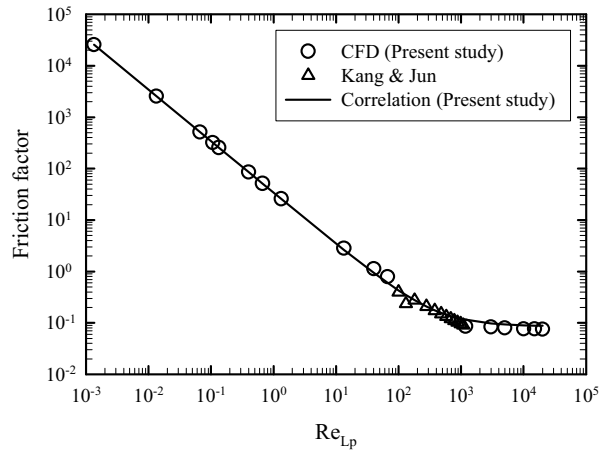
(a) Lp9A22



(b) Lp9A27



(a) Lp9A32



(a) Lp9A37

Fig. 5.4 Comparison of friction factors between previous data and novel correlation of present study of louvered fin

It is observed that the error between new empirical equation for friction coefficient of louvered fin and database is within 10% on average.

### 5.3.2 Permeability and Ergun constant of louvered fin

Momentum equation for louvered fin assumed as a porous medium is as in Equation (5.16).

$$\nabla p = -\frac{\mu_f}{K} \vec{u}_D - \frac{C_E}{K^{1/2}} \rho |\vec{u}_D| \vec{u}_D \quad (5.16)$$

Here,  $K$  is the permeability ( $\text{m}^2$ ) and  $C_E$  is Ergun constant.

Equation (5.16) is the modified Darcy equation, where its first term of the right-hand side is referred to as the Darcy term, and the second term is referred to as non-Darcy or Forchheimer term. In the theory of porous media, when Reynolds number is less than 1, the pressure drop in the flow through porous medium is linearly proportional to Darcy velocity. Here, the permeability is constant, and the momentum equation is Darcy equation. However, if Reynolds number is greater than 1, the pressure drop in the flow through porous medium is no longer linearly proportional to Darcy velocity, and the permeability is not constant either. Therefore, non-Darcy effect, or namely, inertial force appears. Hence, if a louvered fin is assumed to be a porous medium, and modified Darcy equation is used as momentum equation, the intrinsic permeability and Ergun constant of louvered fin must be determined. In previous chapters, this study obtained an empirical equation for the friction coefficient of the louvered fin with porosity assumption, and in general, the relationship between pressure drop and friction coefficient is described by Equation (5.17).

$$\frac{\Delta p}{L} = f \frac{\rho}{2} \frac{1}{L_p} \left( \frac{u_D}{\varepsilon} \right)^2 \quad (5.17)$$

By substituting Equation (5.13) into Equation (5.17), and comparing the

coefficients with the modified Darcy equation, the intrinsic permeability and Ergun constant of the louvered fin with porosity assumption can be obtained as below:

Permeability of louvered fin

$$K = \frac{2\varepsilon L_p^2}{C_1} \quad (5.18)$$

Ergun constant of louvered fin

$$C_E = \frac{C_2}{2\varepsilon^2 L_p} \sqrt{K} \quad (5.19)$$

Therefore, the intrinsic permeability and Ergun constant of louvered fin was turned into a function louvered fin parameters (louver pitch, louver angle, and fin pitch) and the porosity of louvered fin. Figure 5.5 shows the permeability of louvered fin with different Reynolds number and louver model.

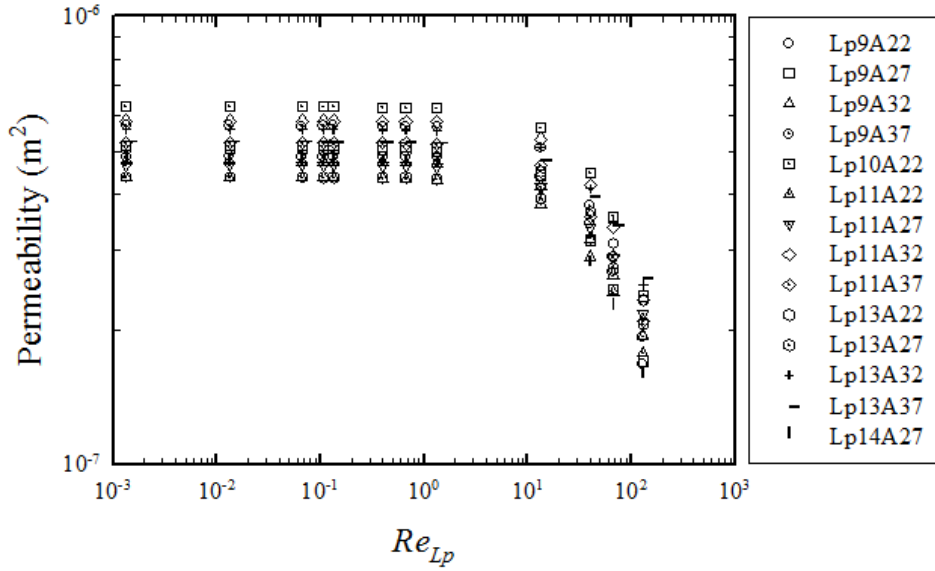


Fig. 5.5 Permeability as a function of the Reynolds number for various louvered fin geometries

In this figure, it is seen that when Reynolds number is than 1, the permeability is constant irrespective of louver fin model, and that when Reynolds number is greater than 1, the permeability is no longer constant. This is accurately in line with the theory of porous media. According to the theory of porous media, when Reynolds number is less than 1, viscous force is dominant, and pressure gradient is linearly proportional to Darcy velocity. Hence, permeability is constant. However, if Reynolds number is greater than 1, inertial force comes into effect, the pressure gradient is no longer linearly proportional to Darcy velocity, and thus permeability is no longer constant. Therefore, it is appropriate that louvered fin was assumed to be a porous medium in this study.

#### 5.4 Need to new friction correlation for louvered fin

Numerous researchers previously developed friction coefficient models for a louvered fin for its performance enhancement. These models have high accuracy for the operating range of a car. However, these models are not appropriate for friction coefficient equations assuming louvered fin to be a porous medium. It can be seen that in previous friction coefficient models, pressure gradient of louvered fin is proportional to an exponent between 1 and 2 with respect to velocity. This cannot represent any of viscous or inertial forces. It is, however, designed for the best agreement with test results in the operating range of a car. Therefore, the prediction accuracy degrades significantly outside of the operating range of a car (in terms of Reynolds number, between 100 and 1000).

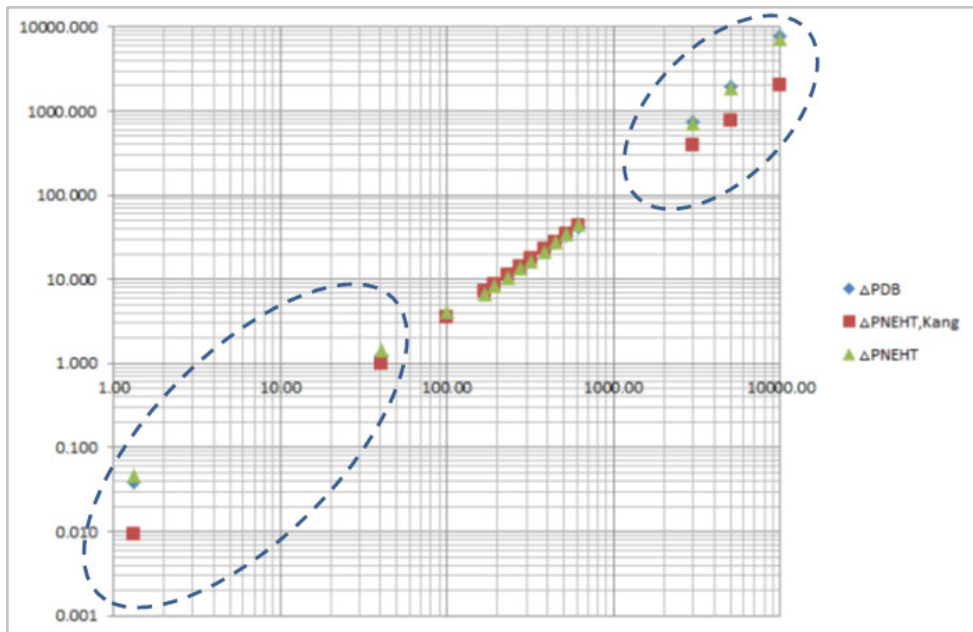


Fig 5.6 Comparison of louvered fin friction factor according to wide range Reynolds number



Figure 5.6 shows the comparison between the database of louvered fin, friction model of Kang and Jun [1], and the CFD analysis result with porosity assumption using Equation (5.13). For Reynolds number between 100 and 1000, the three data sets are in good agreement, but when Reynolds number is less than 100 or greater than 1000, the friction coefficient from Kang and Jun [1] has a significant difference to the value from the database. However, the CFD results computed using the friction coefficient obtained from this study are in good agreement with the database. Therefore, it is seen that the friction coefficient equation for a louvered fin with porosity assumption is with good agreement to the properties of porous media compared to previous numerous previous friction coefficient equations.

## 6. Validation

### 6.1 Validation for louvered fin

In the previous chapter, the intrinsic permeability, Ergun constant, and interfacial heat transfer coefficient were determined for a louvered fin with porosity assumption. Using these determined values, the following governing equations of porous medium can be solved.

Continuity equation

$$\nabla \cdot \vec{u}_D = 0 \quad (6.1)$$

Momentum equation

$$\nabla p = -\frac{\mu_f}{K} \vec{u}_D - \frac{C_E}{K^{1/2}} \rho |\vec{u}_D| \vec{u}_D \quad (6.2)$$

Energy equation

Fluid side

$$\frac{\partial \langle T \rangle^f}{\partial t} + \frac{\vec{u}_D}{\varepsilon} \frac{\partial \langle T \rangle^f}{\partial x} = \frac{\langle k \rangle^f}{\varepsilon(\rho c_p)_f} \frac{\partial^2 \langle T \rangle^f}{\partial x^2} + \frac{h_{sf} A_0}{\varepsilon(\rho c_p)_f} (\langle T \rangle^s - \langle T \rangle^f) \quad (6-3a)$$

Solid side

$$\frac{\partial \langle T \rangle^s}{\partial t} = \frac{\langle k \rangle^s}{(1-\varepsilon)(\rho c_p)_s} \frac{\partial^2 \langle T \rangle^s}{\partial x^2} - \frac{h_{sf} A_0}{(1-\varepsilon)(\rho c_p)_s} (\langle T \rangle^s - \langle T \rangle^f) \quad (6-3b)$$

Moreover, the intrinsic permeability, Ergun constant, and interfacial heat transfer coefficient are as follows:

$$K = \frac{2\varepsilon L_p^2}{C_1} \quad (6-4)$$

$$C_E = \frac{C_2}{2\varepsilon^2 L_p} \sqrt{K} \quad (6-5)$$

$$h = 1.81 \frac{\rho u_D C_p}{\varepsilon \text{Pr}^{2/3}} \text{Re}_{L_p}^{-0.698} \left( \frac{L_p}{F_p \cos \theta} \right)^{0.364} \quad (6-6)$$

First verification test is the comparison between CFD results for two-pitch louvered fin and the one with porosity assumption. The analysis model and the conditions used for the two-pitch louvered fin in this study are as follow:

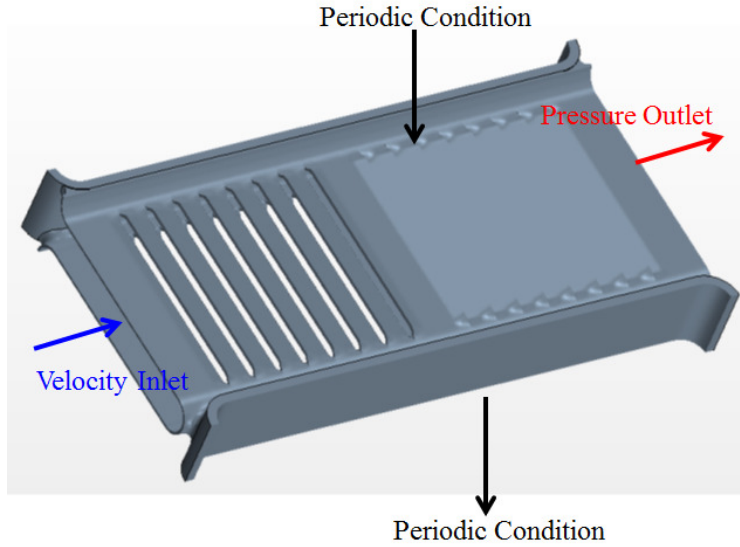
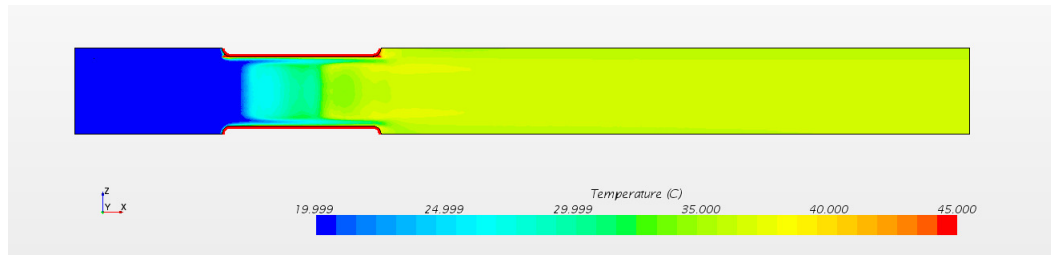


Fig. 6.1 Boundary conditions for louvered fin

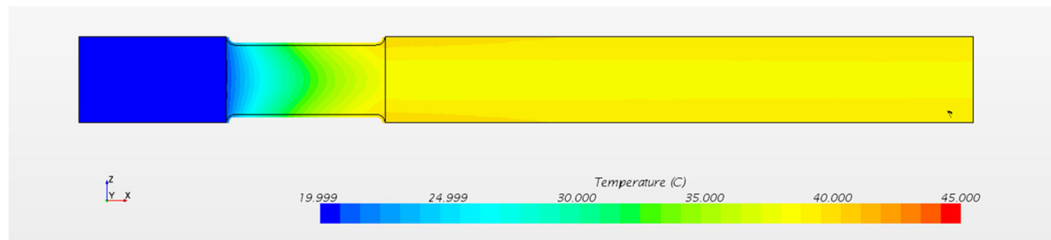
The temperature distributions in fluid and solid sides obtained from the CFDs of two-pitch louvered fin and the one with porosity model are as follow:

Fluid Region

With fin geometry

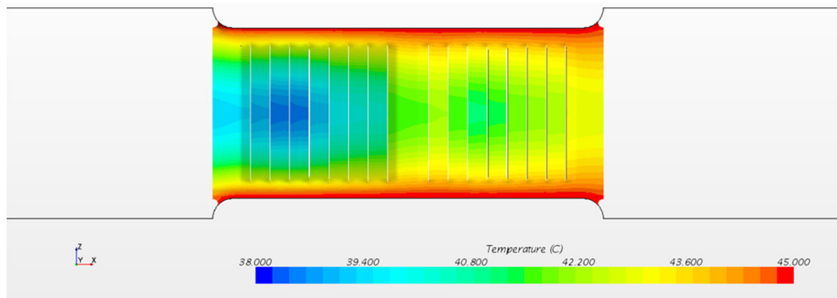


Without fin geometry



Solid Region

With fin geometry



Without fin geometry

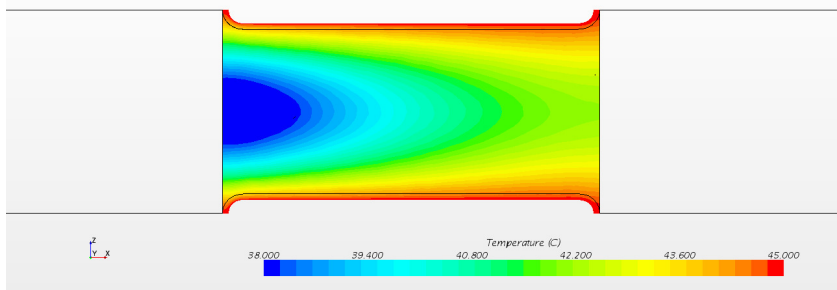


Table 6.1 Comparison of Full 3D 2-pitch louvered fin and NEHT simulation

| Lp9A22   | Outlet temperature of fluid [ $^{\circ}\text{C}$ ] |                 |
|----------|--|-----------------|
| Reynolds | CFD  | NEHT Simulation |
| 580      | 37.2   | 38.8            |
| 680      | 36.3   | 37.8            |
| 780      | 35.4   | 36.9            |

Table 6.1 shows the predicted outlet temperatures with increasing Reynolds number obtained from the CFD of two-pitch louvered fin and NEHT CFD. It is

seen that the difference between the predicted temperatures from these two simulations is within one degree. However, while the number of volume elements required for CFD of two-pitch louvered fin CFD was 2 million, the number of volume elements required for NEHT simulation was only 10,000. Therefore, using the porosity model developed in this study, while there is 1 degree error in the outlet temperature, the required number of volume elements decreases by a factor of 200. Thus, except for special situations, engineers do not have to use 200 times larger computational resources for improvement of 1 degree in accuracy. However, comparing the surface temperature predicted from two-pitch louvered fin CFD and NEHT simulation, the surface temperature predicted by NEHT simulation has no significant meaning locally.

## 6.2 Experimental Set up

In order to experimentally validate the CFD results from this study, test was conducted by using the below experimental set-up.

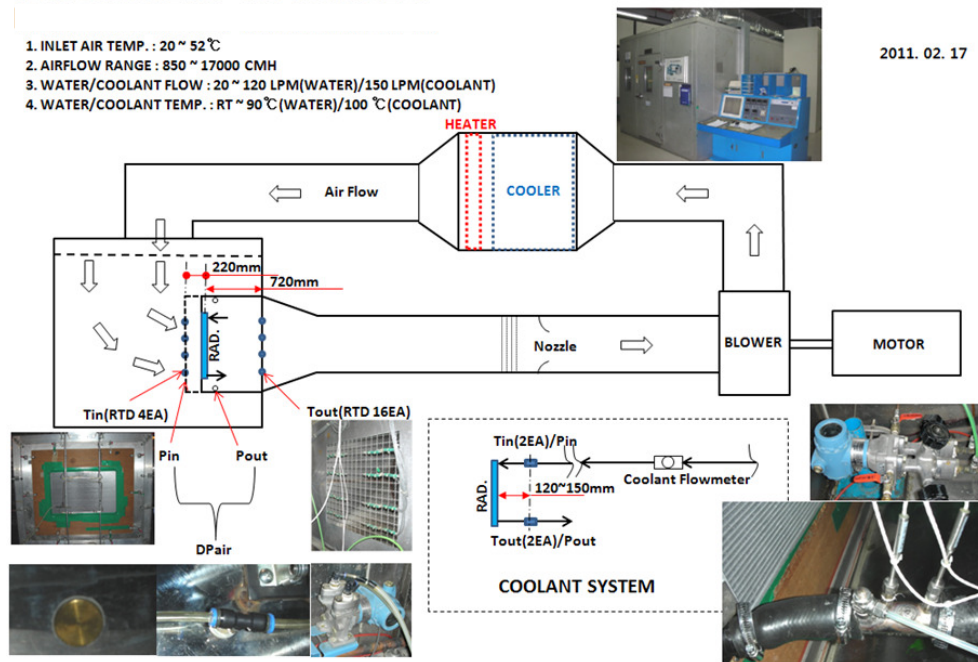


Fig. 6.2 Experimental Set up for Compact Heat Exchanger

Above experimental apparatus consists of working fluid part and cooled air part. The cooled air part controls the amount of air through the suction in the blower, and the temperature of the air from 20 to 52 degrees by using the heater in the front of the cooler. Moreover, four temperature sensors were equipped in series along the core, 220mm in front of the compact heat exchanger, and a total of 16 sensors were equipped 720mm behind the core of heat exchanger. Similarly, pressure sensors were equipped at the front and back of the core, in order to measure the pressure loss in the cooled air. The working fluid part can control the amount of flow using coolant flowmeter, and pressure and temperature sensors were equipped 120-150mm behind the

heat exchanger. Moreover, this device can control the flow rate from 20 to 150 lpm depending on the working fluid, and inlet temperature of the coolant can also be controlled from 90 to 100 degrees. Table 6.2 summarizes the specifications of this experimental apparatus.

Table 6.2 Capacity of Experimental apparatus

| Item                             | Unit  | Range      |
|----------------------------------|-------|------------|
| Dry Bulb Temp.                   | °C    | 20.0~50.0  |
| Air Flow Range                   | CMH   | 850~17,000 |
| Water Temp.                      | °C    | 25~90      |
| Water Flow Range                 | l/min | 20~180     |
| Coolant Temp.                    | °C    | 25~110     |
| Coolant Flow Range               | l/min | 20~180     |
| Water/Coolant Side Pressure Drop | mmHg  | 0~1,000    |
| Air Pressure Drop                | mmAq  | 0~150      |



### 6.3 Uncertainty Analysis

Uncertainty can be defined as the possible value of error. If the accuracy of the measurement device is known, the uncertainty of the experimental apparatus used in this study can be evaluated using the methods proposed by Kline and McClintock [31]. Uncertainty model proposed by Kline and McClintock[31] is as below.

If the test result  $R$  is a function of  $n$  independent variables ( $x_1, x_2, \dots, x_n$ ) and denoting the uncertainty of these independent variables by  $w_1, w_2, \dots, w_n$ , and the overall uncertainty by  $w_R$ ,

$$R = R(x_1, x_2, x_3, \dots, x_n)$$

$$w_R = \left[ \left( \frac{\partial R}{\partial x_1} w_1 \right)^2 + \left( \frac{\partial R}{\partial x_2} w_2 \right)^2 + \dots + \left( \frac{\partial R}{\partial x_n} w_n \right)^2 \right]^{1/2}$$

Or,

$$\left( \frac{w_R}{R} \right)^2 = \left( \frac{x_1}{R} \frac{\partial R}{\partial x_1} \right)^2 \left( \frac{w_{x_1}}{x_1} \right)^2 + \left( \frac{x_2}{R} \frac{\partial R}{\partial x_2} \right)^2 \left( \frac{w_{x_2}}{x_2} \right)^2 + \dots + \left( \frac{x_n}{R} \frac{\partial R}{\partial x_n} \right)^2 \left( \frac{w_{x_n}}{x_n} \right)^2$$

First of all, let us calculate the uncertainty in the heat quantity of air.

The equation for heat quantity of air is as below:

$$Q_{air} = \dot{m}_{air} c_{p,air} \Delta T$$

Taking the partial derivative with respect to each independent variable,

$$\left(\frac{w_{Q_{air}}}{Q_{air}}\right)^2 = \left(\frac{w_{\dot{m}_{air}}}{\dot{m}_{air}}\right)^2 + \left(\frac{w_{c_{p,air}}}{c_{p,air}}\right)^2 + \left(\frac{w_{\Delta T}}{\Delta T}\right)^2$$

Therefore, considering the accuracy of the measurement device used in this study, the uncertainty of the heat quantity of air is seen to be 2.97%.

Secondly, let us calculate the uncertainty of  $f$  factor (Fanning friction factor), which is a dimensionless variable describing pressure drop in the air.

$f$  factor is defined by the below equation.

$$f = \frac{2\Delta p}{\rho_{air} u_c^2} \frac{A_c}{A_{tot}}$$

Similarly, taking the partial derivative of the above equation with respect to independent variables,

$$\left(\frac{w_f}{f}\right)^2 = \left(\frac{w_{\Delta p}}{\Delta p}\right)^2 + \left(\frac{w_{\rho_{air}}}{\rho_{air}}\right)^2 + 4\left(\frac{w_{u_c}}{u_c}\right)^2 + \left(\frac{w_{A_c}}{A_c}\right)^2 + \left(\frac{w_{A_{tot}}}{A_{tot}}\right)^2$$

Therefore, uncertainty of  $f$  factor is 5.09%.

Thirdly, let us calculate the uncertainty of dimensionless heat transfer coefficient  $j$  factor (Colburn  $j$  factor).  $j$  factor is defined by the below equation.

$$j = St Pr^{2/3} = \frac{h Pr^{2/3}}{\rho_{air} c_{p,air} u_c}$$

Taking the partial derivative with respect to each independent variables,

$$\left(\frac{w_j}{j}\right)^2 = \left(\frac{w_h}{h}\right)^2 + \left(\frac{2}{3}\right)^2 \left(\frac{w_{\text{Pr}}}{\text{Pr}}\right)^2 + \left(\frac{w_{\rho_{\text{air}}}}{\rho_{\text{air}}}\right)^2 + \left(\frac{w_{c_{p,\text{air}}}}{c_{p,\text{air}}}\right)^2 + \left(\frac{w_{u_c}}{u_c}\right)^2$$

Therefore, the uncertainty of  $j$  factor is seen to be 3.29%.

#### 6.4 Validation for Compact Heat Exchanger with louvered fin

The second verification test for a louvered fin model with porosity assumption is the evaluation of analysis for a 3D model of compact heat exchanger containing a louvered fin. For this verification, a small radiator model (with 60 tubes and 61 louvered fins) was used. The analysis model is shown in Figure 6.2.

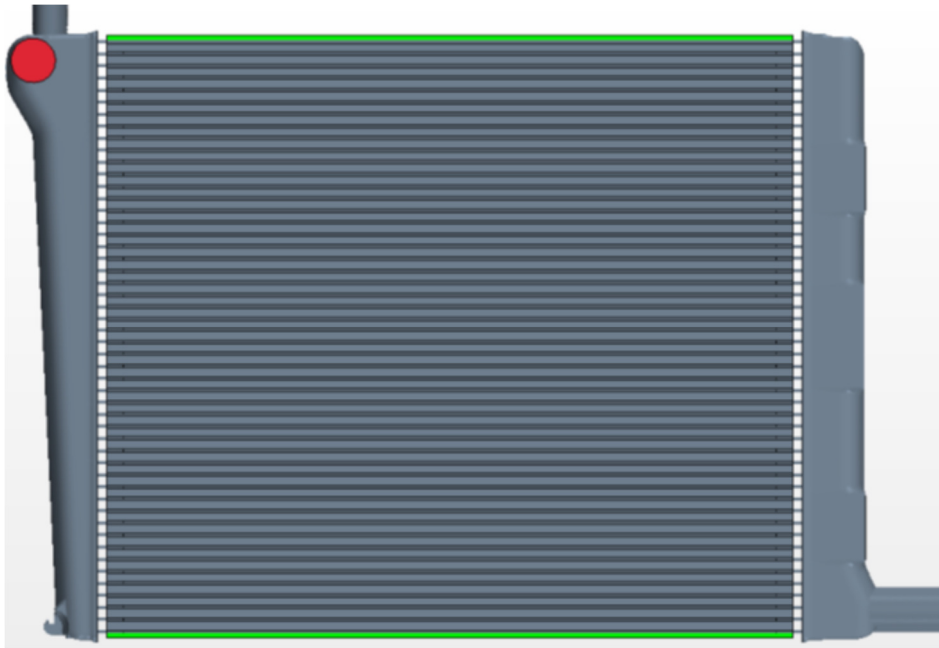


Fig. 6.3 Computational domain for compact heat exchanger

The governing equations for louvered fin with porosity assumption are Equations (6.1) - (6.3), and the required constants are described by Equations (6.4) - (6.6). However, the regions except the louvered fin region have the following governing equations.

Continuity equation

$$\nabla \cdot \vec{u} = 0 \quad (6-7)$$

Momentum equation

$$\rho \frac{\partial \vec{u}}{\partial t} + \rho (\vec{u} \cdot \nabla) \vec{u} = -\nabla p + \mu \nabla^2 \vec{u} + \rho \vec{f} \quad (6-8)$$

Energy equation

$$\rho C_p \frac{DT}{Dt} = \nabla \cdot \kappa \nabla T \quad (6-9)$$

Turbulence model

$$\mu_t = \rho C_\mu \frac{k^2}{\varepsilon}, \quad \mu = \mu_t + \mu_l \quad (6-10)$$

$$\frac{\partial}{\partial t}(\rho k) + \frac{\partial}{\partial x_k}(\rho u_k k) = \frac{\partial}{\partial x_j} \left( \frac{\mu}{\sigma_k} \frac{\partial k}{\partial x_j} \right) + G - \rho \varepsilon \quad (6-11)$$

$$\frac{\partial}{\partial t}(\rho \varepsilon) + \frac{\partial}{\partial x_k}(\rho u_k \varepsilon) = \frac{\partial}{\partial x_j} \left( \frac{\mu}{\sigma_\varepsilon} \frac{\partial \varepsilon}{\partial x_j} \right) + (C_{1\varepsilon} G - C_{2\varepsilon} \rho \varepsilon) \left( \frac{\varepsilon}{k} \right) \quad (6-12)$$

$$C_\mu = 0.09, \quad \sigma_k = 1.00, \quad \sigma_\varepsilon = 1.30, \quad C_{1\varepsilon} = 1.44, \quad C_{2\varepsilon} = 1.92$$

$$G = \mu_t \frac{\partial u_i}{\partial x_j} \left[ \frac{\partial u_i}{\partial x_j} + \frac{\partial u_j}{\partial x_i} \right] \quad (6-13)$$

Where,

$k$  : Turbulent kinetic energy

$\varepsilon$  : Rate of dissipation of turbulent kinetic energy

$\mu_t$  : Turbulent viscosity

$\mu_l$  : Laminar viscosity

$G$  : Rate of generation of turbulence energy

The volume grid of the compact heat exchanger containing a louvered fin used in this study is shown in Figure 6.3.

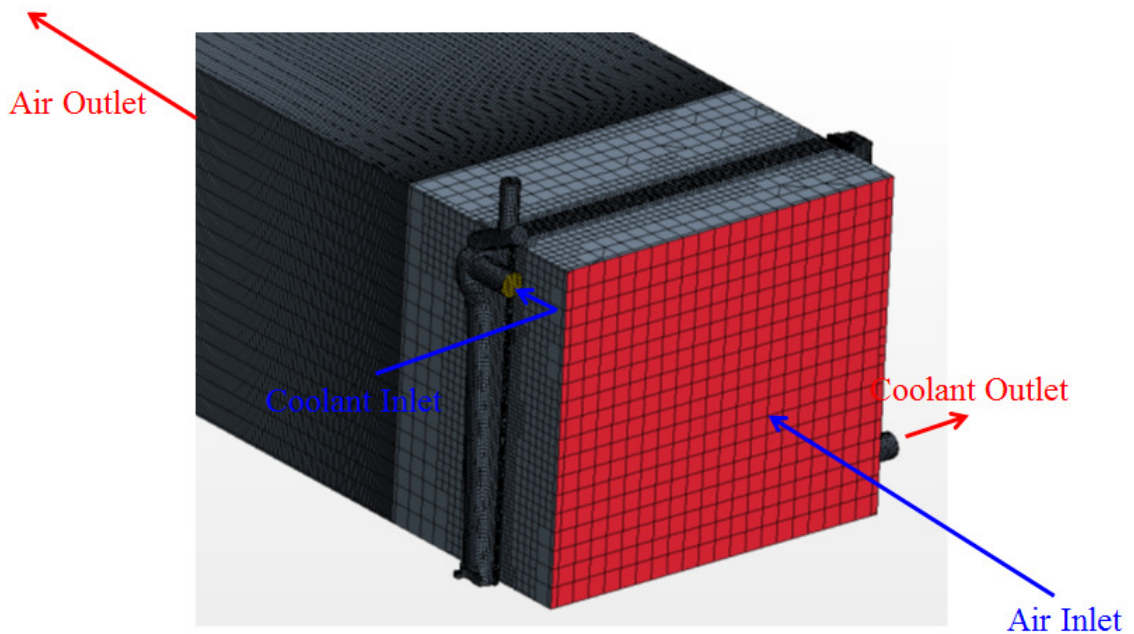


Fig. 6.4 Volume grid for compact heat exchanger with louvered fin

Moreover, the number of volume elements used in this grid model was divided into each region, and this is shown in Table 6.3

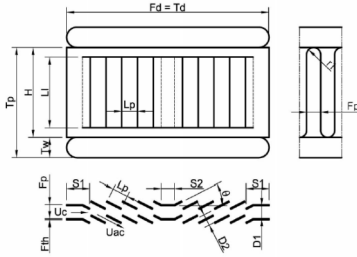
Table 6.3 Number of cells for each region consist of compact heat exchanger

| Air       | Coolant   | Fin              | Solid   |
|-----------|-----------|------------------|---------|
| 1,178,120 | 4,096,350 | <b>2,146,226</b> | 616,832 |

The number of volume elements required for this analysis model is around 8 million. In particular, 2 million cells are required for the louvered fin with porosity assumption, which is 1200 times less than 24.4 billion cells for the louvered fin without porosity assumption. Specifications of louver fin and tube are shown in Table 6.4

Table 6.4 Louvered fin-tube parameters

| Louvered Fin                  |                        |                               |                            | Tube                        |                             |                             |
|-------------------------------|------------------------|-------------------------------|----------------------------|-----------------------------|-----------------------------|-----------------------------|
| Louver Pitch<br>( $L_p$ , mm) | Louver Angle<br>(deg.) | Depth of Fin<br>( $F_d$ , mm) | Fin Pitch<br>( $F_p$ , mm) | Tube Depth<br>( $T_d$ , mm) | Tube Pitch<br>( $T_p$ , mm) | Tube Width<br>( $T_w$ , mm) |
| 0.8                           | 23                     | 14                            | 1.1                        | 14                          | 7.3                         | 1.8                         |



Boundary conditions are given by inlet temperature of 20°C and frontal velocity of 2,4,6,8, and 10 m/s for air, and for coolant, inlet temperature of 80°C and volumetric flow rate of 20,40,60,80, and 100 liter/min.

Performing a numerical analysis using above boundary condition, the results were obtained as shown in Table 6.4.

Table 6.5 Comparison of Experimental and Numerical data for compact heat exchanger containing louvered fin

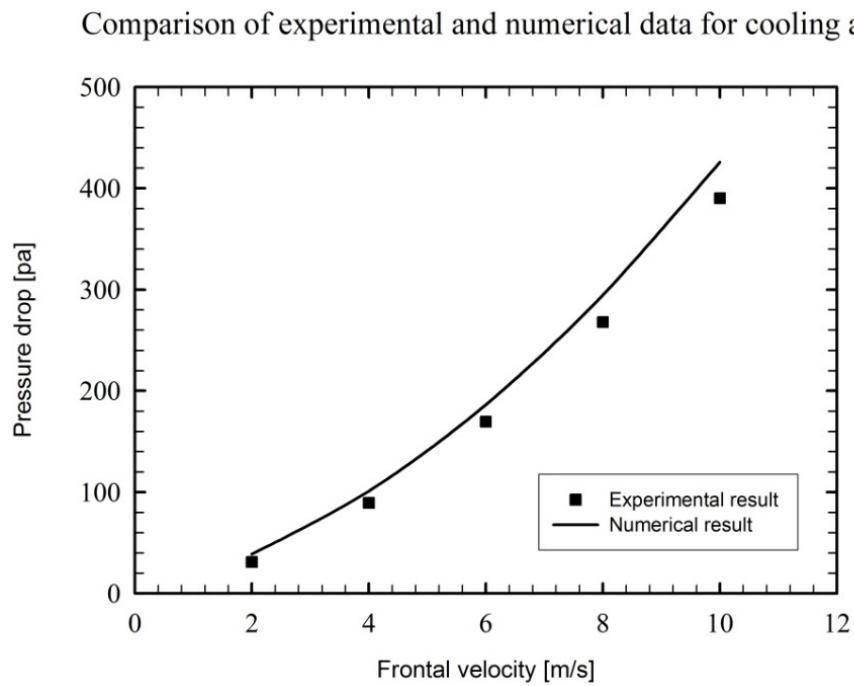
| Coolant           | 20 lpm |       | 20 lpm |        | 20 lpm |        | 20 lpm |       | 20 lpm |        |
|-------------------|--------|-------|--------|--------|--------|--------|--------|-------|--------|--------|
| Air               | 2 m/s  |       | 4 m/s  |        | 6 m/s  |        | 8 m/s  |       | 10 m/s |        |
|                   | Exp.   | Num.  | Exp.   | Num.   | Exp.   | Num.   | Exp.   | Num.  | Exp.   | Num.   |
| dp [Pa]           | 30.99  | 38.8  | 89.44  | 101.04 | 169.56 | 186.35 | 267.92 | 294.6 | 390.11 | 425.9  |
| Tout,cool [°C]    | 69.18  | 69.51 | 63.85  | 64.55  | 61.34  | 61.93  | 59.28  | 60.38 | 58.13  | 59.35  |
| Tout,air [°C]     | 58.97  | 59.37 | 49.79  | 48.94  | 43.77  | 42.61  | 39.71  | 38.54 | 36.72  | 35.75  |
| Heat Capacity [W] |        |       |        |        |        |        |        |       |        |        |
| Coolant           | 40 lpm |       | 40 lpm |        | 40 lpm |        | 40 lpm |       | 40 lpm |        |
| Air               | 2 m/s  |       | 4 m/s  |        | 6 m/s  |        | 8 m/s  |       | 10 m/s |        |
|                   | Exp.   | Num.  | Exp.   | Num.   | Exp.   | Num.   | Exp.   | Num.  | Exp.   | Num.   |
| dp [Pa]           | 31.09  | 38.8  | 89.83  | 101.03 | 170.14 | 186.35 | 266.45 | 294.6 | 386.09 | 425.89 |
| Tout,cool [°C]    | 74.18  | 74.18 | 70.23  | 70.92  | 67.91  | 69.03  | 66.43  | 67.84 | 65.25  | 67.01  |
| Tout,air [°C]     | 62.96  | 63.65 | 55.56  | 53.98  | 49.7   | 47.42  | 45.4   | 42.92 | 42.34  | 39.71  |
| Heat Capacity [W] |        |       |        |        |        |        |        |       |        |        |

| Coolant           | 60 lpm  |       | 60 lpm  |        | 60 lpm  |        | 60 lpm  |       | 60 lpm  |       |
|-------------------|---------|-------|---------|--------|---------|--------|---------|-------|---------|-------|
| Air               | 2 m/s   |       | 4 m/s   |        | 6 m/s   |        | 8 m/s   |       | 10 m/s  |       |
|                   | Exp.    | Num.  | Exp.    | Num.   | Exp.    | Num.   | Exp.    | Num.  | Exp.    | Num.  |
| dp [Pa]           | 30.89   | 38.8  | 88.55   | 101.03 | 167.3   | 186.35 | 265.47  | 294.6 | 386.48  | 425.9 |
| Tout,cool [°C]    | 75.98   | 75.97 | 73.09   | 73.57  | 71.25   | 72.13  | 69.9    | 71.19 | 69.02   | 70.53 |
| Tout,air [°C]     | 64.14   | 65.31 | 57.33   | 56.08  | 51.72   | 49.52  | 47.6    | 44.89 | 44.45   | 41.53 |
| Heat Capacity [W] |         |       |         |        |         |        |         |       |         |       |
| Coolant           | 80 lpm  |       | 80 lpm  |        | 80 lpm  |        | 80 lpm  |       | 80 lpm  |       |
| Air               | 2 m/s   |       | 4 m/s   |        | 6 m/s   |        | 8 m/s   |       | 10 m/s  |       |
|                   | Exp.    | Num.  | Exp.    | Num.   | Exp.    | Num.   | Exp.    | Num.  | Exp.    | Num.  |
| dp [Pa]           | 30.99   | 38.79 | 89.04   | 101.04 | 168.58  | 186.34 | 265.37  | 294.6 | 383.24  | 425.9 |
| Tout,cool [°C]    | 76.91   | 76.92 | 74.74   | 75.02  | 73.24   | 73.86  | 72.06   | 73.08 | 71.27   | 72.54 |
| Tout,air [°C]     | 64.98   | 66.21 | 58.36   | 57.28  | 52.81   | 50.76  | 48.72   | 46.1  | 45.69   | 42.63 |
| Heat Capacity [W] |         |       |         |        |         |        |         |       |         |       |
| Coolant           | 100 lpm |       | 100 lpm |        | 100 lpm |        | 100 lpm |       | 100 lpm |       |
| Air               | 2 m/s   |       | 4 m/s   |        | 6 m/s   |        | 8 m/s   |       | 10 m/s  |       |
|                   | Exp.    | Num.  | Exp.    | Num.   | Exp.    | Num.   | Exp.    | Num.  | Exp.    | Num.  |
| dp [Pa]           | 30.89   | 38.8  | 88.75   | 101.04 | 168.38  | 186.35 | 264.78  | 294.6 | 386.38  | 425.9 |
| Tout,cool [°C]    | 77.71   | 77.51 | 75.73   | 75.94  | 74.5    | 74.95  | 73.53   | 74.3  | 72.79   | 73.84 |
| Tout,air [°C]     | 65.28   | 66.76 | 59      | 58.04  | 53.6    | 51.54  | 49.54   | 46.83 | 46.28   | 43.35 |
| Heat Capacity [W] |         |       |         |        |         |        |         |       |         |       |

Moreover, Figure 6.4 shows the pressure drop in the air, outlet temperature of the air, and outlet temperature of coolant with respect to inlet temperature. Comparing the analysis results with experimental data, it is seen that the air pressure drop is accurate within 10%, and that the predicted outlet temperature is accurate within 2° C. Figure 6.5 shows the surface temperature of the compact heat exchanger for each coolant inlet flow rate and for each air frontal velocity. For constant coolant outlet temperature, as the frontal velocity of air increases, the temperature of louvered fin-tube surface decreases owing to an

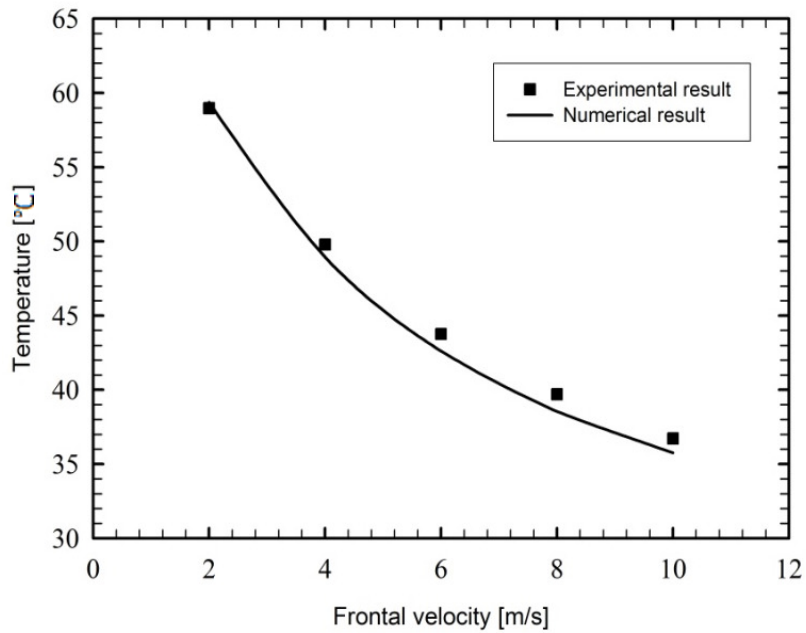


increase in heat transfer. Therefore, it is observed from the verification regarding louvered fin and a 3D performance analysis of compact heat exchanger containing a louvered fin that the friction coefficient equation for louvered fin with a porosity equation obtained in this paper is highly effective. Therefore, since the engineers can predict the performance through an analysis without the need for actual test, a fast and accurate analysis is possible with low cost, enhancing the design and manufacturing cost competitiveness.



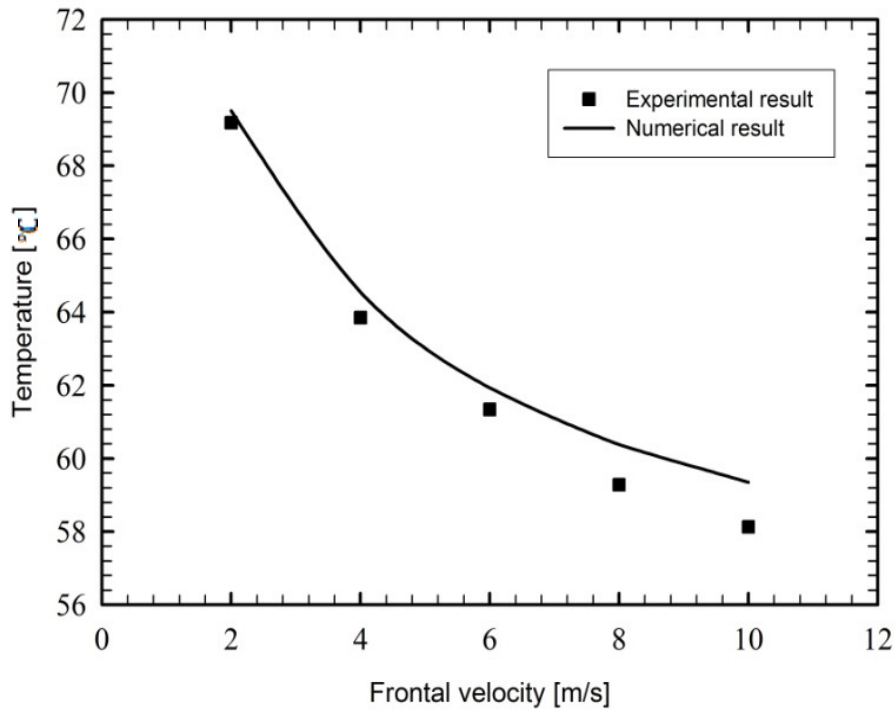
(a) Comparison of Experimental and numerical data for pressure drop

Comparison of experimental and numerical data for cooling air



(b) Comparison of Experimental and numerical data for cooling air outlet temperature

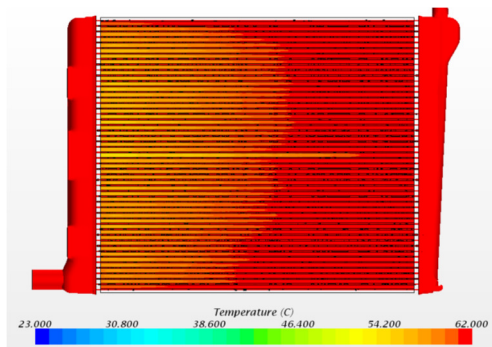
Comparison of experimental and numerical data for coolant



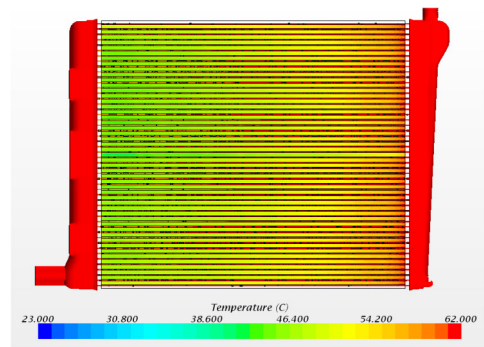
(c) Comparison of Experimental and numerical data for coolant outlet temperature

Fig. 6.5 Comparison of experimental and numerical data according to mass flow of coolant and air

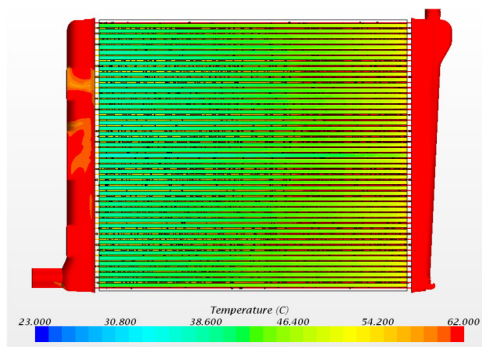
Distribution of surface temperature according to mass flow of coolant and air (Coolant = 20lpm)



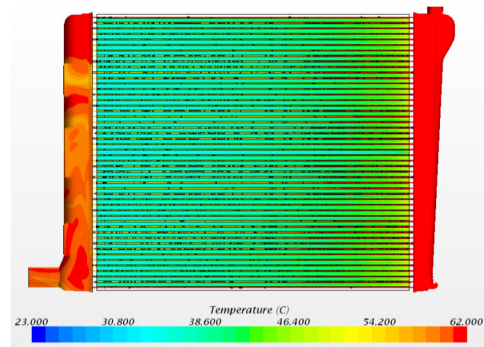
$V_{\text{air}} = 2\text{m/s}$



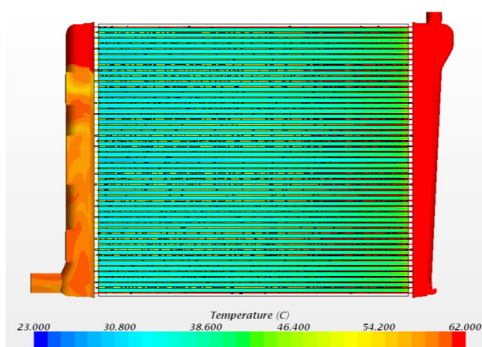
$V_{\text{air}} = 4 \text{ m/s}$



$V_{\text{air}} = 6\text{m/s}$

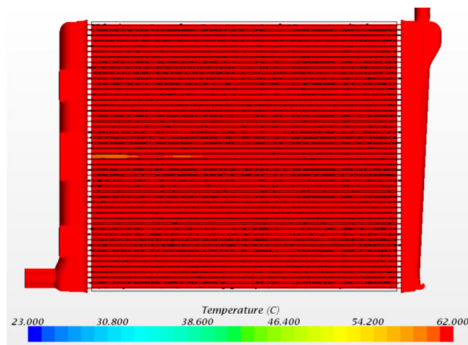


$V_{\text{air}} = 8\text{m/s}$

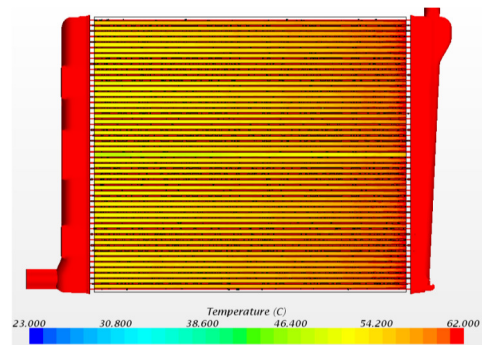


$V_{\text{air}} = 10\text{m/s}$

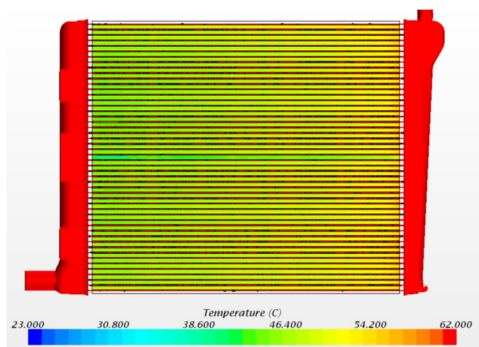
Distribution of surface temperature according to mass flow of coolant and air (Coolant = 40lpm)



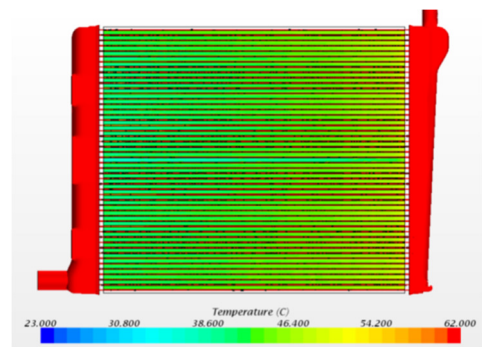
$$V_{\text{air}} = 2\text{m/s}$$



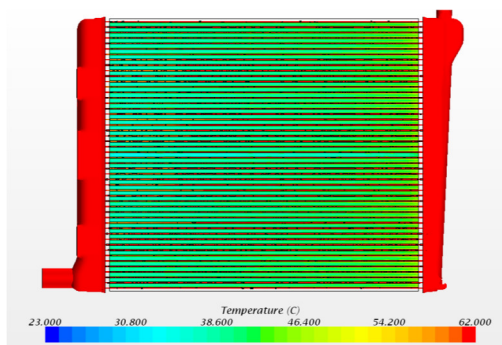
$$V_{\text{air}} = 4\text{m/s}$$



$$V_{\text{air}} = 6\text{m/s}$$

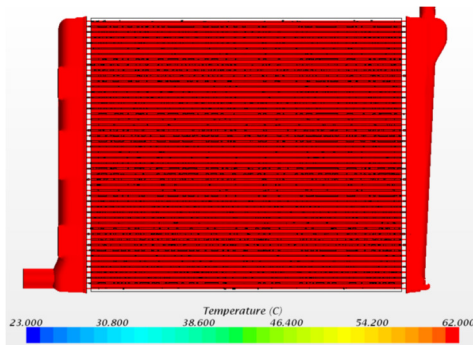


$$V_{\text{air}} = 8\text{m/s}$$

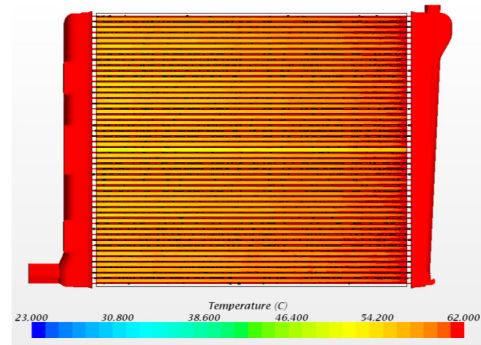


$$V_{\text{air}} = 10\text{m/s}$$

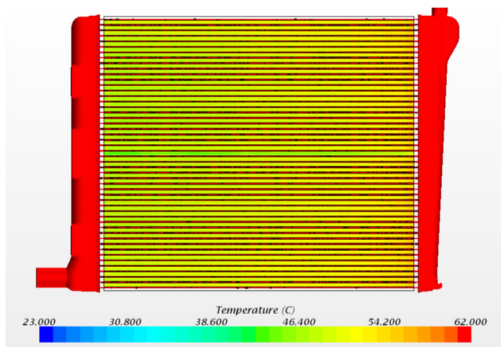
Distribution of surface temperature according to mass flow of coolant and air (Coolant = 60lpm)



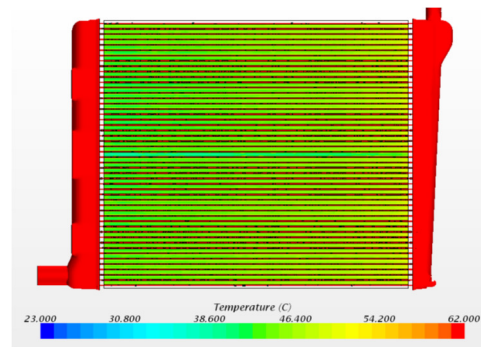
$$V_{\text{air}} = 2\text{m/s}$$



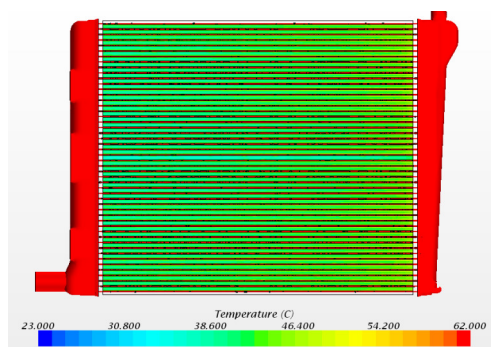
$$V_{\text{air}} = 4\text{m/s}$$



$$V_{\text{air}} = 6\text{m/s}$$

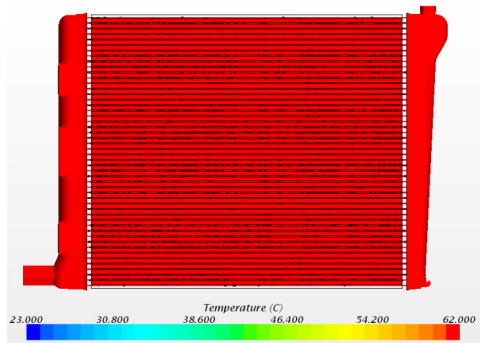


$$V_{\text{air}} = 8\text{m/s}$$

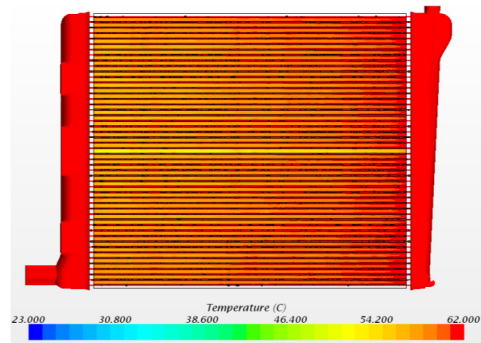


$$V_{\text{air}} = 10\text{m/s}$$

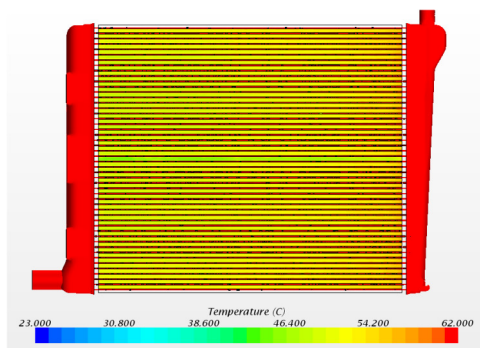
Distribution of surface temperature according to mass flow of coolant and air (Coolant = 80lpm)



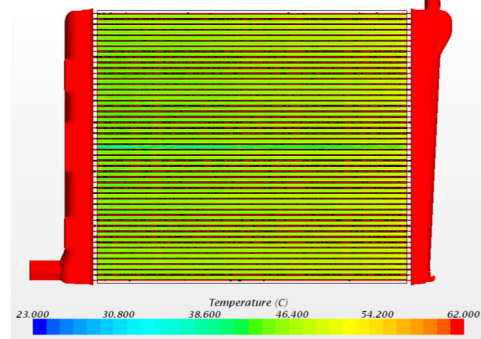
$$V_{\text{air}} = 2\text{m/s}$$



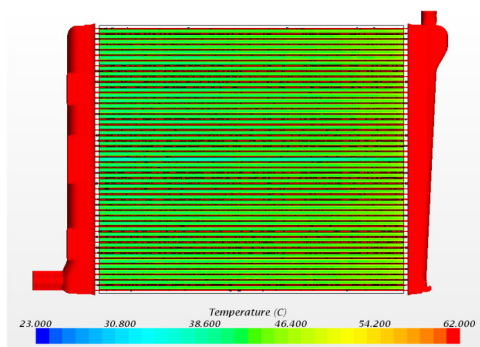
$$V_{\text{air}} = 4\text{m/s}$$



$$V_{\text{air}} = 6\text{m/s}$$



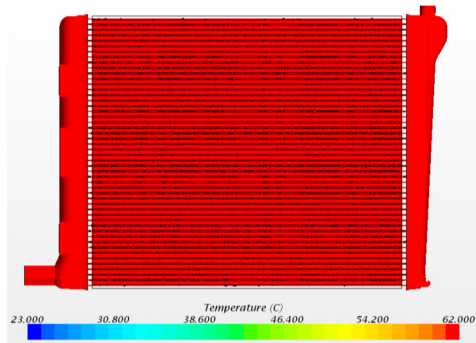
$$V_{\text{air}} = 8\text{m/s}$$



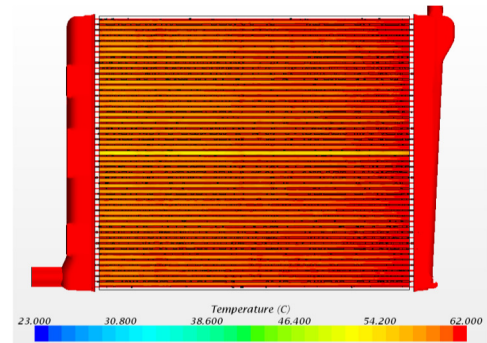
$$V_{\text{air}} = 10\text{m/s}$$



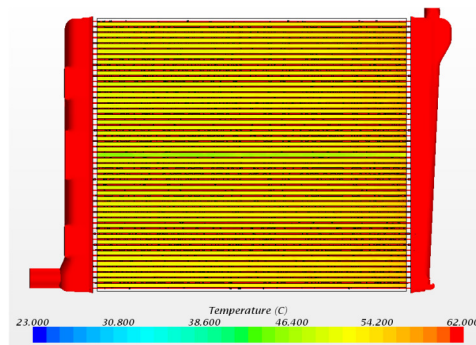
Distribution of surface temperature according to mass flow of coolant and air (Coolant = 100lpm)



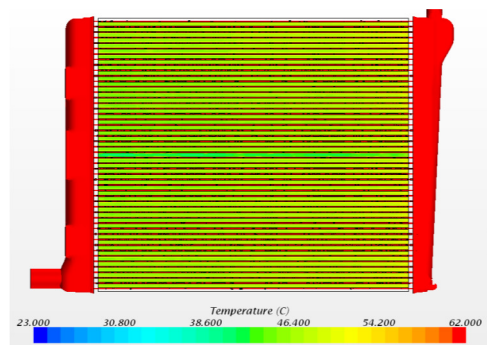
$$V_{\text{air}} = 2\text{m/s}$$



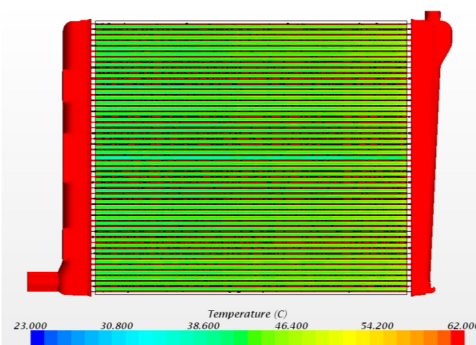
$$V_{\text{air}} = 4\text{m/s}$$



$$V_{\text{air}} = 6\text{m/s}$$



$$V_{\text{air}} = 8\text{m/s}$$



$$V_{\text{air}} = 10\text{m/s}$$



## 6.5 Comparison of CFD and 1D simulation using new $f$ correlation

Figure 6.6 compares the new friction model proposed in this paper and the previous friction model from Kang and Jun [1].

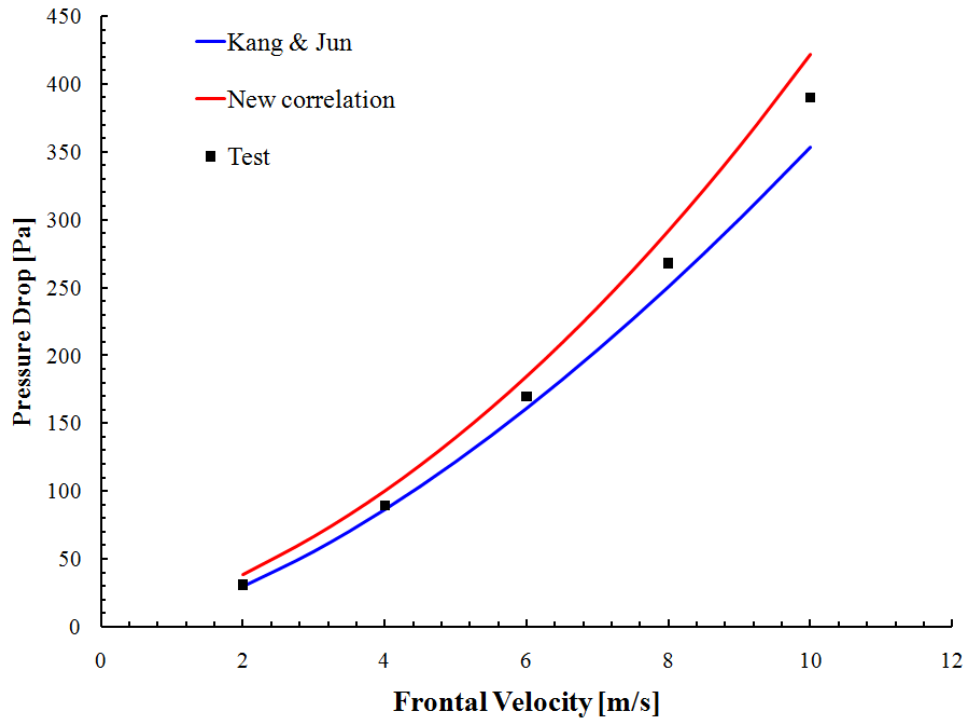


Fig. 6.6 Prediction of pressure drop according to friction models

In Figure 6.6, Kang and Jun model [1] has the tendency to underestimate the test data, and the new correlation model has the tendency to overestimate the data. Thus, thereby showing both models have a similar degree of error. However, since the experimental data from Kang and Jun [1] considers the pressure drop in the core only, the results can be closer to the experimental data if the losses at inlet and outlet are taken into account. Figure 6.7 shows the performance comparison between the 3D simulation results obtained using a new correlation model, and the 1D simulation results obtained using the

model from Kang and Jun [1]. As can be seen in this Figure, the 3D simulation results are closer to the experimental results, and this is because the CFD analysis can consider the stream-wise change in the temperature of the tube.

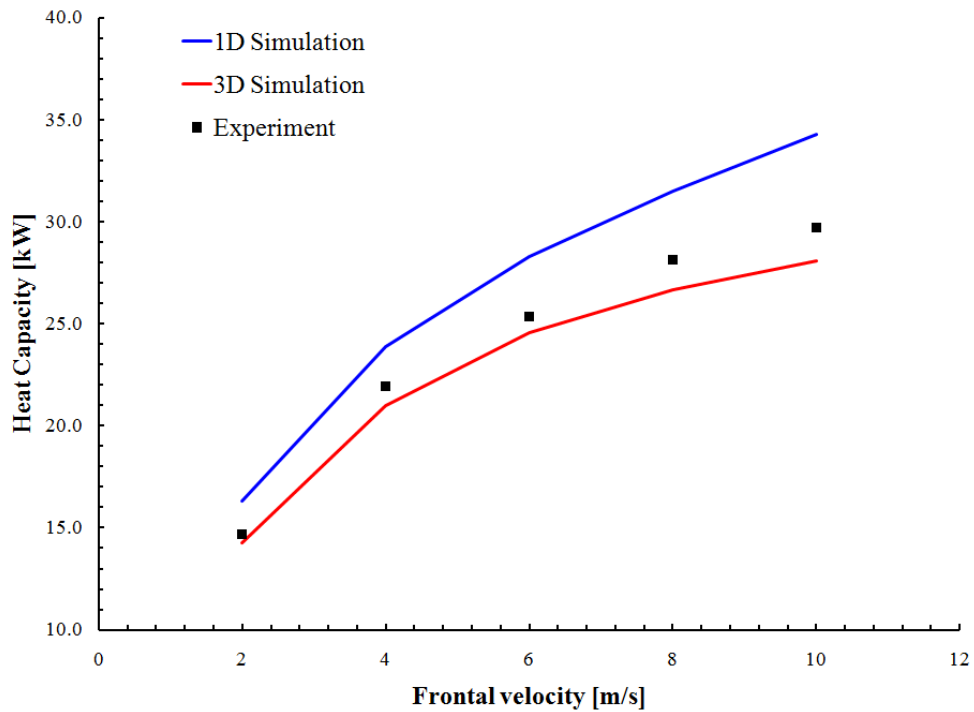


Fig. 6.7 Comparison of 1D and 3D Simulation

Figure 6.8 shows the comparison between the pressure drops predicted from Darcy equation and modified Darcy equation according to frontal velocity. In this figure, since Darcy equation describes the pressure drop from viscous force without considering inertial force, the pressure drop curve appears as a linear equation of frontal velocity. In contrast, modified Darcy equation considers viscous and inertial forces simultaneously, and pressure drop increases nonlinearly with frontal velocity. Meanwhile, as frontal velocity becomes smaller, the contribution of viscous force to pressure drop becomes

larger, owing to the increase in viscous force.

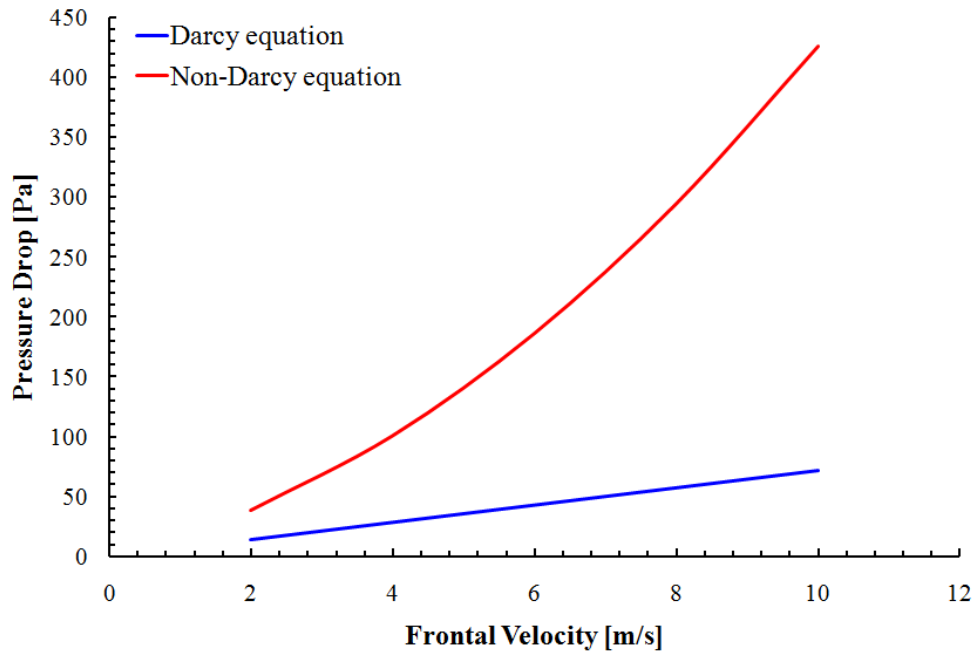


Fig. 6.8 Comparison of Darcy- and Modified Darcy equation

## 7. Conclusion

### 7.1 Summary

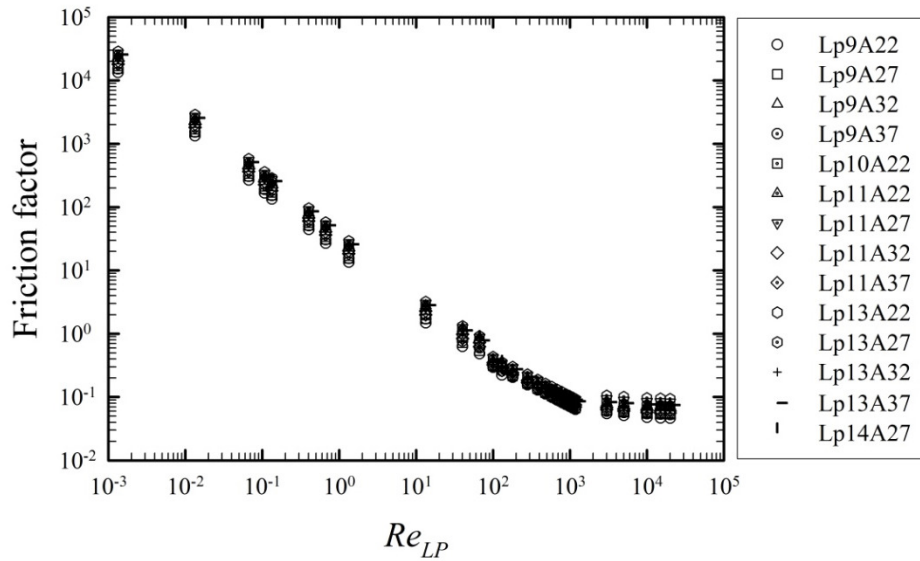
This thesis assumed a louvered fin to be a porous medium in order to enable 3D performance evaluation of compact heat exchangers containing a louvered fin, and obtained the intrinsic permeability and Ergun constant of louvered fin under porosity assumption. 3D performance evaluation of compact heat exchanger containing a louvered fin was performed using the obtained permeability and Ergun constant, and Colburn  $j$  factor from Kang and Jun [1] as interfacial heat transfer coefficient. Comparing with the experimental results, the accuracy of the predicted pressure drop in cooled air was observed to be within 10%, and the accuracy of predicted outlet temperatures of cooled air and coolant was seen to be within 2°C. Hence, the results from this thesis can be summarized into four main categories.

#### *Establishment of database to obtain a new friction coefficient of louvered fin*

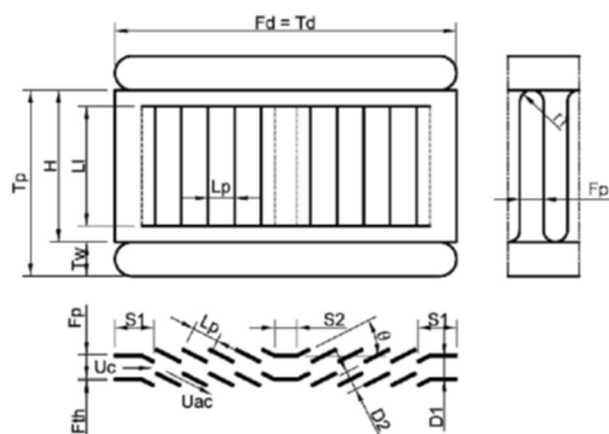
If a louvered fin is assumed to be a porous medium, a new friction coefficient equation for a louvered fin must be developed. This is because viscous force is dominant for Reynolds number less than 1, and for Reynolds number greater than 1, both viscous and inertial forces affect the pressure drop in fluid passing through a porous medium. Moreover, for Reynolds number greater than 1000, the value is constant irrespective of Reynolds number. Therefore, in order to obtain the friction coefficient of louvered fin that reflects the properties of a porous medium, the ranges of Reynolds number less than 1 and Reynolds number greater than 1000 are required. Permeability can be determined when Reynolds number is less than 1, and Ergun constant can be determined when Reynolds number is greater than 1000. Previous friction coefficient equations for a louvered fin are typically for the range of Reynolds number between 1

and 1000, which corresponds to the operating range of a car. Hence, this thesis obtained the friction coefficient of louvered fin for Reynolds number from 0.001 to 30,000.

In order to develop and verify the new friction coefficient equation, the test results and model information from Kang and Jun [1] were used in this thesis. The friction coefficients for Reynolds number from 100 to 1000 were obtained from the data of Kang and Jun [1], and for Reynolds number less than 100 or greater than 1000, database was established using CFD. Below table shows the fin-tube parameters for 14 different types of louvered fin model used in this study and the work of Kang and Jun [1].



| Name                          | Symbol      | Lp9<br>A22 | Lp9<br>A27 | Lp9<br>A32 | Lp9<br>A37 | Lp11<br>A22 | Lp11<br>A27 | Lp11<br>A32 | Lp11<br>A37 | Lp13<br>A22 | Lp13<br>A27 | Lp13<br>A32 | Lp13<br>A37 | Lp14<br>A27 | Lp10<br>A22 |
|-------------------------------|-------------|------------|------------|------------|------------|-------------|-------------|-------------|-------------|-------------|-------------|-------------|-------------|-------------|-------------|
| Louver pitch                  | $L_p$       | 2.7        | 2.7        | 2.7        | 2.7        | 3.3         | 3.3         | 3.3         | 3.3         | 3.9         | 3.9         | 3.9         | 3.9         | 4.2         | 3.0         |
| Louver angle                  | $\theta$    | 22         | 27         | 32         | 37         | 22          | 27          | 32          | 37          | 22          | 27          | 32          | 37          | 27          | 22          |
| Non-louvered region           | $S_1$       | 5.25       | 5.25       | 5.25       | 5.25       | 4.05        | 4.05        | 4.05        | 4.05        | 4.05        | 4.05        | 4.05        | 4.05        | 6.30        | 5.39        |
| Re-direction length           | $S_2$       | 2.33       | 2.33       | 2.33       | 2.33       | 3.00        | 3.00        | 3.00        | 3.00        | 3.00        | 3.00        | 3.00        | 3.00        | 3.60        | 6.15        |
| Depth of fin                  | $F_d$       | 54.0       | 54.0       | 54.0       | 54.0       | 54.0        | 54.0        | 54.0        | 54.0        | 54.0        | 54.0        | 54.0        | 54.0        | 54.0        | 55.5        |
| Fin pitch                     | $F_p$       | 3.64       | 3.64       | 3.64       | 3.64       | 3.64        | 3.64        | 3.64        | 3.64        | 3.64        | 3.64        | 3.64        | 3.64        | 3.64        | 3.64        |
| Fin thickness                 | $F_{th}$    | 0.27       | 0.27       | 0.27       | 0.27       | 0.27        | 0.27        | 0.27        | 0.27        | 0.27        | 0.27        | 0.27        | 0.27        | 0.27        | 0.27        |
| Fin height                    | $H$         | 23.6       | 23.6       | 23.6       | 23.6       | 23.6        | 23.6        | 23.6        | 23.6        | 23.6        | 23.6        | 23.6        | 23.6        | 23.6        | 27.2        |
| Louver length                 | $L_l$       | 18.6       | 18.6       | 18.6       | 18.6       | 18.6        | 18.6        | 18.6        | 18.6        | 18.6        | 18.6        | 18.6        | 18.6        | 18.6        | 22.2        |
| Tube depth                    | $T_d$       | 54.0       | 54.0       | 54.0       | 54.0       | 54.0        | 54.0        | 54.0        | 54.0        | 54.0        | 54.0        | 54.0        | 54.0        | 54.0        | 55.5        |
| Tube pitch                    | $T_p$       | 29.2       | 29.2       | 29.2       | 29.2       | 29.2        | 29.2        | 29.2        | 29.2        | 29.2        | 29.2        | 29.2        | 29.2        | 29.2        | 32.8        |
| Tube width                    | $T_w$       | 5.6        | 5.6        | 5.6        | 5.6        | 5.6         | 5.6         | 5.6         | 5.6         | 5.6         | 5.6         | 5.6         | 5.6         | 5.6         | 5.6         |
| Average $L_p^2$               | $\bar{L}_p$ | 3.00       | 3.00       | 3.00       | 3.00       | 3.52        | 3.52        | 3.52        | 3.52        | 4.08        | 4.08        | 4.08        | 4.08        | 4.73        | 3.38        |
| Number of louver <sup>3</sup> | -           | 17         | 17         | 17         | 17         | 15          | 15          | 15          | 15          | 13          | 13          | 13          | 13          | 11          | 15          |
| Number of fin <sup>4</sup>    | -           | 35         | 35         | 35         | 35         | 35          | 35          | 35          | 35          | 35          | 35          | 35          | 35          | 35          | 35          |
| HEX width <sup>5</sup>        | -           | 118.8      | 118.8      | 118.8      | 118.8      | 118.8       | 118.8       | 118.8       | 118.8       | 118.8       | 118.8       | 118.8       | 118.8       | 118.8       | 132.8       |
| Fin material                  | -           | Al         | Al         | Al         | Al         | Al          | Al          | Al          | Al          | Al          | Al          | Al          | Al          | Al          | Al          |



#### *Determination of intrinsic permeability and Ergun constant of louvered fin*

To solve the louvered fin model with porosity assumption through a 3D numerical analysis, the intrinsic permeability and Ergun constant of louvered fin must be determined. Hence, in this study, the intrinsic permeability and Ergun constant of louvered fin was determined through the regression analysis on the database of friction coefficients obtained in the previous step. The friction coefficient of louvered fin was assumed to be of below form:

$$f = \frac{C_1}{\text{Re}_{L_p}} + C_2$$

Since the assumed form of friction coefficient is nonlinear, first of all, a nonlinear regression analysis was performed on 14 different types of louvered fin model to determine the most suitable  $C_1$  and  $C_2$ . A multi-linear regression analysis was then performed to turn  $C_1$  and  $C_2$  into functions of louvered fin parameters, including louver pitch, louver angle, and fin pitch. Finally, the friction coefficient equation for louvered fin was obtained as below:

$$f = \frac{14.8 + 13.3 \ln(L_p / F_p) - 104 \ln(\cos \theta)}{\text{Re}_{L_p}} + 0.0455 + 0.0327 \ln(L_p / F_p) - 0.224 \ln(\cos \theta)$$

By substituting the above empirical equation into the equations for pressure drop and friction coefficient and simplifying, the intrinsic permeability and Ergun constant for louvered fin under porosity assumption were obtained.

$$K = \frac{2\varepsilon L_p^2}{C_1}$$

$$C_E = \frac{C_2}{2\varepsilon^2 L_p} \sqrt{K}$$

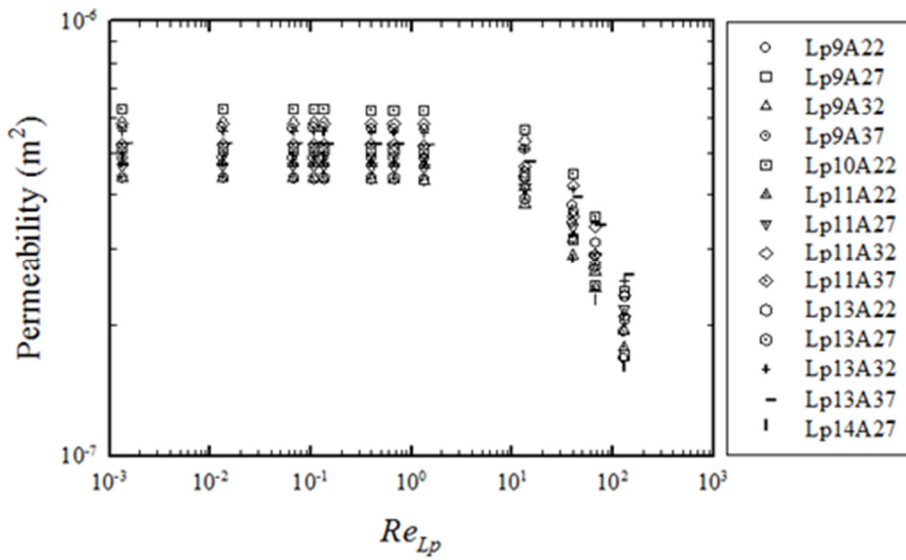
| Model   | $C_1$    | $C_2$   |
|---------|----------|---------|
| Lp9A22  | 17.87247 | 0.05430 |
| Lp9A27  | 22.58648 | 0.06200 |
| Lp9A32  | 29.88127 | 0.07140 |
| Lp9A37  | 34.30446 | 0.08270 |
| Lp11A22 | 20.51004 | 0.06040 |
| Lp11A27 | 24.70168 | 0.06650 |
| Lp11A32 | 32.48772 | 0.08200 |
| Lp11A37 | 36.02504 | 0.09240 |
| Lp13A22 | 24.26002 | 0.06340 |
| Lp13A27 | 27.11923 | 0.06830 |
| Lp13A32 | 33.23943 | 0.08170 |
| Lp13A37 | 38.23295 | 0.10430 |
| Lp14A27 | 29.95682 | 0.07750 |
| Lp10A22 | 20.39249 | 0.05930 |

#### *Ensuring reliable analysis accuracy*

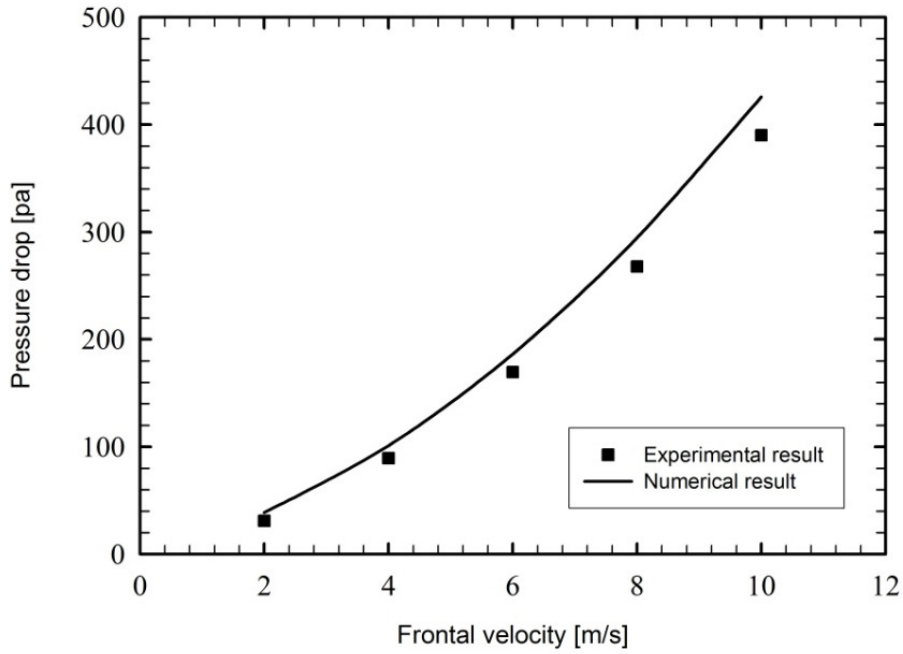
Permeability and Ergun constant of the louvered fin under the porosity assumption were obtained, and the following was deduced from applying the obtained permeability equation to 14 different types of louvered fin model with different Reynolds number. The pattern of change in the permeability of louvered fin accurately reflects the properties of porous media. In other words, for Reynolds number less than 1, pressure drop in the fluid passing through a porous medium is linearly proportional to velocity, and permeability is therefore constant. However, when Reynolds number is greater than 1, the pressure drop is no longer linearly proportional to velocity, and hence permeability is not constant as well. The permeability of louvered fin in this



study reflects this phenomenon. Therefore, it is highly appropriate to assume louvered fin to be a porous medium. By using the intrinsic permeability of louvered fin, Ergun constant, and  $j$  factor from Kang and Jun [1], a 3D performance analysis was performed for a compact heat exchanger containing louvered fin. It was observed that the pressure drop is predicted within 10% accuracy, and that the outlet temperatures of cooled air and coolant are predicted within 2° C accuracy.

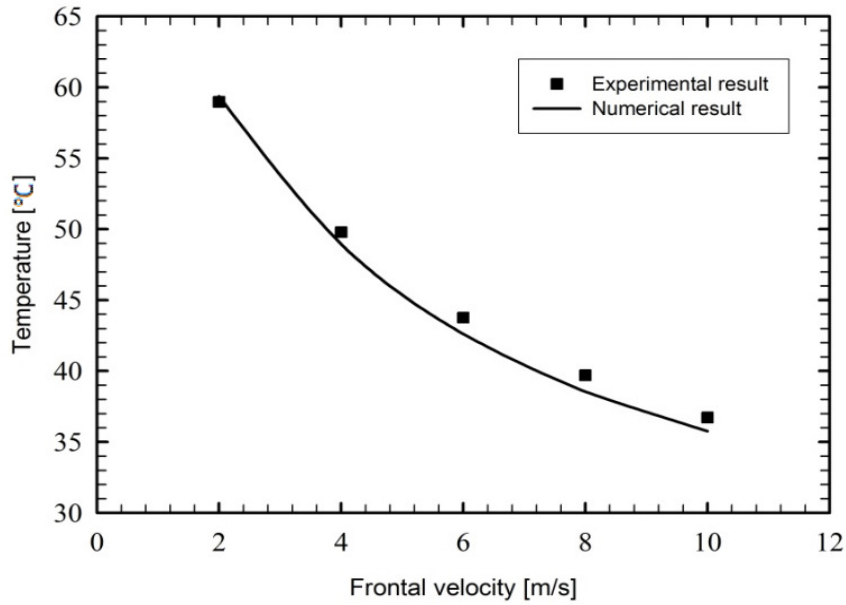


Comparison of experimental and numerical data for cooling air



(a) Comparison of Experimental and numerical data for pressure drop

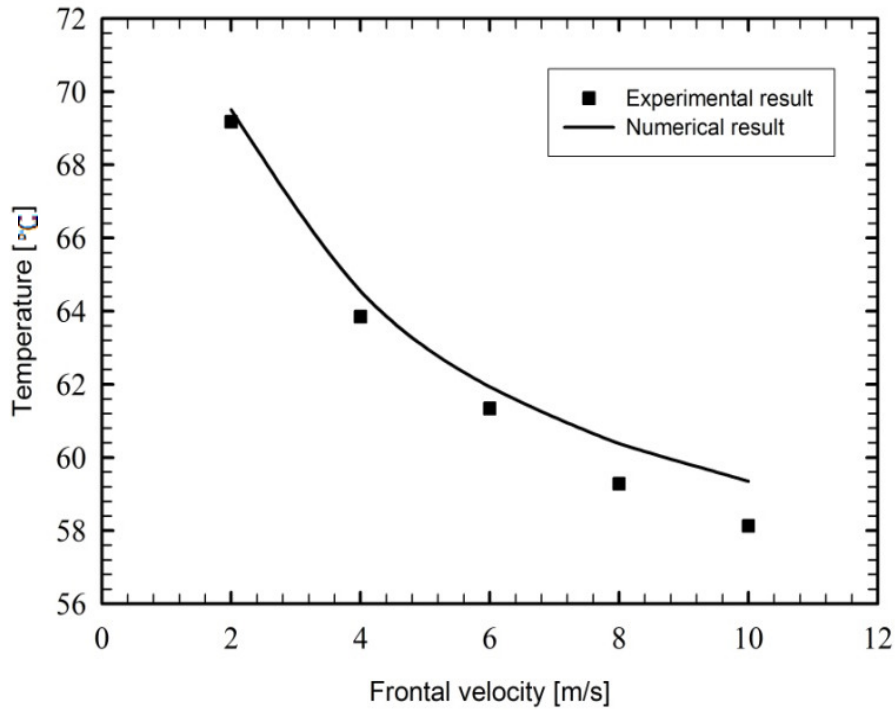
Comparison of experimental and numerical data for cooling air



(b) Comparison of Experimental and numerical data for cooling air outlet

temperature

Comparison of experimental and numerical data for coolant



(c) Comparison of Experimental and numerical data for coolant outlet temperature

*A tool that can replace the experiment for louvered fin compact heat exchanger performance measurement.*

It was observed that, using the intrinsic permeability and Ergun constant developed in this thesis and interfacial heat transfer coefficient of Kang and Jun [1], a 3D performance evaluation of compact heat exchanger containing a louvered fin is possible, and that the accuracy of this is reliable.

## 7.2 Future work

The application of compact heat exchanger is not limited to the use in cars, but can also be extended to all devices that require efficient heat exchange. There are 5 common types of heat exchanger fins.

*Louvered fin*

*Offset fin*

*Wavy fin*

*Pin fin*

*Straight fin*

Traditionally, the above five types of fins were used for a long time depending on the application, and numerous researchers have developed models for friction and heat transfer coefficients of each type as well. However, the demand for a 3D numerical analysis is continuously increasing, given the significant increase in numerical resources and the desire for improved competitiveness through reduction in development time. However, despite the increase in numerical resources, a 3D numerical analysis of louvered fin had been significantly limited due to the complex geometry and difficult flow and heat transfer dynamics. However, in this study, it was shown that the 3D numerical analysis of compact heat exchanger containing a louvered fin can be performed with reliable degree of accuracy. Therefore, future works will develop friction coefficient equations for the other four types of fins that are appropriate for porosity assumption unlike previous works. Once the friction coefficient equations are obtained for these 5 types of fins, it is expected that the engineers will be able to obtain and analyze results from numerical analysis for various geometries and conditions using the desired fin, and thus replacing experiments.

## References

1. H. C. Kang and G. W. Jun, Heat Transfer and Flow Resistance Characteristics of Louver Fin Geometry for Automobile Applications, Journal of Heat Transfer, Vol. 133(2011)
2. Chang, Yu. J. and Wang, C. C., A Generalized Heat Transfer Correlation for Louver Fin Geometry, Int. J. Heat and Mass Transfer, Vol.40. No.3, pp533-544 (1997)
3. Chang, Y. J., Hus, K. C., Lin, Y. T. and Wang, C. C., A Generalized Friction Correlation for Louver Fin Geometry, Int. J. Heat and Mass Transfer, Vol. 43, pp. 2237-2243 (1999)
4. Chang, Y. J. and Wang, C. C., Air side Performance of Brazed Aluminum Heat Exchangers, J. Enhanced Heat Transfer, Vol.3, pp.15-28 (1996)
5. Achaichia, A. and Cowell, T. A., Heat Transfer and Pressure Drop Characteristics of Flat Tube and Louvered Plate Fin Surfaces, Experimental Thermal and Fluid Science, Vol. 1, pp.147-157 (1988)
6. Webb, R. L., Principles of Enhanced Heat Transfer, John Wiley & Sons, New York., U.S.A, (1994).
7. Rugh, J. P., Pearson, J. T. and Ramadhyany, S. A Study of a Very Compact heat Exchanger Used for Passenger Compartment Heating in automobiles, in Compact Heat Exchangers for Power and Process Industries, ASME, Sym. Ser. HTD-Vol. 201, pp.15-24, ASME New York. (1992)
8. Davenport, C. J., Correlation for heat transfer and flow friction characteristics of louvered fin, AIChE Symp. Ser. 79, 19-27 (1983)
9. Sunden, B and Svantesson, J., Correlation of  $j$  and  $f$  Factors for Multilouvered Heat Exchanger Surfaces, in Proceedings of the 3<sup>rd</sup> UK National Heat Transfer Conf., pp.805-811 (1992)
10. Sahnoun, A. and Webb, R. L., Prediction of Heat Transfer and Friction for Louver Fin Geometry, J. of Heat Transfer, Vol. 114, pp.893-899. (1992)

11. Frank P. Incropera and David P. DeWitt, Fundamentals of Heat and Mass Transfer, John Wiley & Sons, U.S.A. (1998).
12. M. Kaviany, Principles of Heat Transfer in porous Media, Springer-Verlag, U.S.A. (1991)
13. A. Dybbs, R. V. Edwards, A new Look at Porous Media Fluid Mechanics - Darcy to Turbulent, Vol.82, pp. 199-256 (1984)
14. T. Masuoka, Y. Takatsu, Turbulence model for flow through porous media, Int. J. Heat and Mass Transfer, Vol. 39, pp. 2803-2809 (1996)
15. H. C. Brinkman, On the Permeability of Media Consisting of Closely Packed Porous Interface, Appl. Sci. Res., Vol. A1, 1997
16. H. C. Brinkman, Fluid flow in a Porous medium, Appl. Sci. Res. A, 1947
17. Donald A. Nield and Adrian Bejan, Convection in Porous Media, Springer, U.S.A. (2006)
18. J. C. Slattery, Momentum, Energy, and Mass Transfer in Continua, 2<sup>nd</sup> ed., R. F. Krieger (1981)
19. I. Nozad, R. G. Carbonell, S. Whitaker, Heat Conduction in Multi-Phase Systems I: Theory and Experiments for Two-Phase Systems", Chem. Enging. Sci., Vol. 40, pp.843-855 (1985).
20. J. C. Y. Koh and R. Colony, Heat Transfer of Microstructures for integrated circuits, Int. Comm. Heat Mass Transfer, Vol. 13, pp. 89-98 (1986)
21. S. J. Kim and D. Kim, Forced Convection in Microstructures for Electronic Equipment Cooling, Journal of Heat Transfer, Vol. 121, pp. 639-645 (1999)
22. H. -I. You, C. -H. Chang, Determination of Flow Properties in Non-Darcian Flow, Journal of Heat Transfer, Vol. 119, pp. 190-192 (1997)
23. H. -I You, C. -H. Chang, Numerical Prediction of Heat Transfer Coefficient for a Pin-Fin Channel Flow, Journal of Heat Transfer, Vol. 119, pp.840-843 (1997)
24. D. Kim, S. J. Kim and A. Ortega, Compact Modeling of Fluid Flow and Heat Transfer in Pin Fin Heat Sinks, Journal of Heat Transfer, Vol. 126, pp. 342-

350 (2004)

25. D. K. Kim, J. H. Jung and S. J. Kim, Thermal optimization of plate-fin heat sinks with variable fin thickness, *Int. J. of Heat and Mass Transfer*, Vol. 53, pp. 5988-5995 (2010)
26. J. Cui and D. K. Tafti, Computations of flow and heat transfer in a three-dimensional multilouvered fin geometry, *Int. J. Heat and Mass Transfer*, Vol. 45, pp. 5007-5023 (2002)
27. K. N. Atkinson, R. Drakulic, M. R. Heikal, T. A. Cowell, Two- and three-dimensional numerical models of flow and heat transfer over louvered fin arrays in compact heat exchangers, *Int. J. Heat and Mass Transfer*, Vol. 41, pp. 4063-4080 (1998)
28. Kang, H. C., and Kim, M. H., Effect of Strip Location on the Air-Side Pressure Drop and Heat Transfer in Strip Fin-and-Tube Heat Exchanger, *Int. J. Refrig.*, Vol. 22, pp.302-312 (1999)
29. Kang, H. C., and Webb, R. L., Evaluation of the Wavy Fin Geometry Used in Air-Cooled Finned-Tube Heat Exchangers, *Proceedings of the 11<sup>th</sup> International Heat Transfer Conference*, Vol. 6, pp.273-278 (1998)
30. Steven C. Chapra and Raymond P. Canale, *Numerical Methods for Engineers* Third Ed. McGraw-Hill, U.S.A. (1998)
31. Kline, S. J., F. A. McClintock, Describing Uncertaintites in Single-Sample Experiments, *Mechanical Engineering*, Vol.75, pp. 3-8 (1953)

## Abstract (in Korean)

# 루우버 흰을 가지는 컴팩트 열교환기에 대한 열다공성 모델 연구

서울대학교 대학원

기계항공공학부

김택근

루우버 흰 형상 및 루우버 흰 주위의 복잡한 열·유동 분포에 의해 루우버 흰이 포함된 컴팩트 열교환기의 삼차원 수치해석은 매우 어려운 해석 영역에 속해 왔다. 본 연구에서는 루우버 흰을 다공성 매질로 가정하여 루우버 흰을 포함한 컴팩트 열교환기 삼차원 수치해석이 가능하도록 다공성 매질 성질에 적합한 루우버 흰에 관한 마찰 계수 상관식을 제시하였다. 마찰 계수 상관식으로부터 루우버 흰 고유의 투과율과 Ergun 상수를 루우버 흰 파라미터의 함수로 만들었다. 루우버 흰의 고유 투과율과 Ergun 상수를 결정하기 위해, 3배 확대된 서로 다른 14종에 대한 루우버 흰 모델에 대하여 레이놀즈 수 0.001 부터 30,000에서 마찰 계수에 대한 데이터 베이스를 구축 하였다. 레이놀즈 수 100에서 1000사이에는 이전 연구자들의 마찰 계수 데이터를 취했으며, 레이놀즈 수 100이하와 1000이상에서는 2피치 루우버 흰에 관한 삼차원 수치 해석을 통해 마찰 계수 데이터를 얻었다. 레이놀즈 수 100이하와 1000이상에서 루우버 흰에 관한 마찰 계수 값을 얻은 것은 다공성 매질의 성질에 의해 매우 낮은 레이놀즈 수에서 점성력을 지배하는 다르시 항에서 투과율을 결정하고 높은 레이놀즈 수에서 관성력을 지배하는 비 다르시 항(또는 Forchheimer 항)에서 Ergun 상수를 결정하기 위함이다. 시험과 수치 해석을 통해 얻어진 데이터 베이스로부터 루우버 흰 고유의



투과율과 Ergun 상수를 결정하기 위해 비선형 회귀 분석과 선형 회귀 분석이 차례대로 실시 되었으며, 다공성 매질 성질에 적합한 루우버 환에 관한 새로운 마찰 계수가 제시되었다. 새롭게 제시된 마찰 계수를 다공성 매질 내 운동량 지배 방정식인 수정 다르시 방정식과 계수 비교를 통해 루우버 환 고유의 투과율과 Ergun 상수를 얻었다. 검증을 위해 14종 루우버 환 모델의 데이터 베이스와 상관 상관식부터 얻어진 마찰 계수를 비교하였으며, 평균적으로 10%이내의 오차를 가짐을 알 수 있다. 또한 루우버 환 고유의 투과율을 14종 모델과 레이놀즈 수에 따라 얻었을 때, 루우버 환의 투과율은 레이놀즈 수 1이하에서는 일정한 값을 가지나 레이놀즈 수가 1이상 일때는 투과율이 더 이상 일정하게 유지 하지 않는다. 이것은 정확하게 다공성 매질의 이론과 일치 한다. 다공성 매질 이론에서 레이놀즈 수 1이하 일 때 다공성 매질을 통과하는 유체에 의해 발생되는 압력 강하량은 다르시 속도에 선형 비례하고 이 때 비례 상수는 투과율이 되며 일정한 값을 가지게 된다. 그러나 레이놀즈 수가 1보다 크게 되면, 관성력의 증가로 인해 다공성 매질 내 압력 강하량과 다르시 속도는 비선형 비례하게 되며 이 때 투과율은 더 이상 일정하지 않게 된다. 따라서 루우버 환을 다공성 매질로 가정한 것은 매우 적절한 가정이라 할 수 있다. 루우버 환을 포함한 콤팩트 열교환기에 대한 삼차원 성능 예측을 위해 본 연구에서 제시한 루우버 환에 관한 투과율과 Ergun 상수 그리고 Kang and Jun (2011)의 Colburn j factor를 이용하였다. 첫 번째 시뮬레이션으로 2피치 루우버 환에 관한 삼차원 수치해석과 열다공성 모델이 적용된 수치 해석을 비교하였다. 비교 결과 예측 출구온도는 1도 이내의 오차를 가지지만 체적 격자는 열다공성 모델이 적용된 해석이 대략 1/200 수준으로 작아 짐을 알 수 있었다. 두번째 시뮬레이션으로 루우버 환이 포함된 콤팩트 열교환기에 대한 수치 해석을 실시하였다. 시험 결과와 비교할 때, 냉각 공기 및 냉각수측 출구 온도는 2도 이

내 그리고 냉각 공기측 압력 강하량은 10%이내 오차를 가짐을 알 수 있었다. 흥미로운 점은 본 연구의 검증을 위해 사용된 컴팩트 열교환기를 열다공성 모델을 적용하지 않고 기존 방식대로 해석 모델을 구성할 경우 루우버 흰 부분만 대략 244억 체적 격자가 필요한 반면, 열다공성 모델을 적용할 경우 루우버 흰은 대략 200만 체적 격자만 요구함을 알 수 있다. 뿐만 아니라 루우버 흰이 포함된 삼차원 수치 해석을 위해 요구되는 체적 격자수는 대략 1천만 체적 격자 이하이므로 루우버 흰이 포함된 컴팩트 열교환기 성능 예측을 삼차원 해석을 통해 가능해 졌다. 향후 연구로서 루우버 흰 뿐만 아니라 컴팩트 열교환기 흰으로 자주 사용되는 흰에 대해서 다공성 매질의 성질에 맞게 투과율과 Ergun상수를 결정하여 열교환기 및 차량 냉·난방을 설계하는 설계자는 자유롭게 흰을 선택할 수 있고 쉽게 시뮬레이션을 통해 성능을 예측할 수 있으므로 설계 비용 및 개발 기간을 단축할 수 있다

**Keywords** : 루우버 흰; 다공성 접근법; 투과율; 에르곤 상수; 컴팩트 열교환기; 3차원 수치 해석

**학 번** : 2010-31313